Title
Imaging membrane potential with semiconductor nanoparticle

Permalink
https://escholarship.org/uc/item/07g1b15q

Author
Park, KyoungWon

Publication Date
2014

University of California

Los Angeles

Imaging membrane potential with semiconductor nanoparticle

A dissertation submitted in partial satisfaction of the

requirements for the degree Doctor of Philosophy

in Electrical Engineering

by

Kyoungwon Park

2014

ABSTRACT OF THE DISSERTATION

Imaging membrane potential with semiconductor nanoparticle

by

Kyoungwon Park

Doctor of Philosophy in Electrical Engineering

University of California, Los Angeles, 2014

Professor Bahram Jalali, Chair

Understanding electrical activity of neural network is of great interest. Although electrodes and optical voltage sensors have been evolved over the past few decades, there is no such probe satisfying not only large enough sensitivity but also fast enough time response in large scale yet. Therefore, the reverse engineering on brain circuitry such that ‘every action potential in every neuron in large field of view’ is still far-off.

In this thesis, I introduce the inorganic voltage sensor for neural electricity imaging, based on semiconductor nanoparticles (NPs) *via* quantum-confined Stark effect (QCSE). Firstly, I validate NPs’ QCSE at room temperature (RT) at single molecule level. Based on the experimental results and theoretical investigation, I optimize the NP structure displaying the largest QCSE. Besides, undiscovered physical phenomena including wavelength blue-shift, linear energy-field dependency, and field dependent Auger recombination were revealed from the QCSE experiment for the first time. Secondly, I predict the performance of membrane inserted NPs by self-consistent Schrödinger-Poisson calculation, and propose voltage imaging strategies.

As a delivery method, peptide-based surface coating is developed which successfully guides NPs to the membrane. Lastly, delivered NPs are tested under voltage oscillating HEK cells and they generate voltage dependent emission fluorescence. This voltage information is finally captured and imaged by charge coupled device and analyzed. This result demonstrates the inorganic voltage sensor’s high throughput simultaneous multisite voltage imaging.

The dissertation of Kyoungwon Park is approved.

Robert Candler

Harold Fetterman

Shimon Weiss

Bahram Jalali, Committee Chair

University of California, Los Angeles

2014

TO MY PARENTS AND BROTHER FOR THEIR LOVE, SUPPORT AND SINCERE ENCOURAGEMENT,

TABLE OF CONTENTS

Chapter 1 Introduction

Chapter 2 Single molecule quantum-confined Stark effect

Chapter 3 Electric field dependent Auger recombination rate in semiconductor nanoparticles

Chapter 4 Self-consistent Schrödinger-Poisson calculation and performance prediction and design rules for membrane-embedded semiconducting voltage sensing nanoparticles

Chapter 5 Membrane potential imaging with semiconductor nanoparticle

LIST OF FIGURES

LIST OF TABLES

ACKNOWLEDGEMENTS

First of all, I could not write this page without expressing my deepest thanks to my advisor, Prof Shimon Weiss. I appreciate his encouragement and limitless support he provided me with. I have learnt a lot from his insight, experience and wisdom. I am also privileged to earn invaluable support and professions from Prof. Bahram Jalali. Without their acceptance and continual support, I could not succeed my study. I am grateful for all invaluable advices, and helpful insights of my committee members, Prof. Robert Chandler and Prof. Harrold Fetterman.

As a member of Weiss Group, I was supported by talented members. I am grateful to Jack Li, Sangyoon Chung, Jianmin Xu, Xavier Michalet, Younggyu Kim, Yazan Alhadid and Antonino Ingargiola for their invaluable collaboration and friendship. I specially thank to my colleague, Yung Kuo and my undergraduate students, Will Wookyeom Kim, Lawrence Hsiung and for their enthusiasm and contribution to my research.

I had a great time with my friend, Hyungsuk Yu, Sungmin Kim, Jinha Kang, Jonghyun Eun, Koji Sato, Elda Judica, Raquel Abreu, Yongha Hwang, Andrew Pan and Kyungsik Shin. I would like to thank them all for sharing joyful time and intellectual discussion. I also acknowledge professors in Korea University, Prof. Jaesung Rieh, Sukki Kim, Youngchae Ko, Inkyu Lee, Chulwoo Kim. I should also thank Kiha Hong, Jaykwang Shin for their advice from Samsung Advance Institute of Technology.

I should express my special appreciation to Juyeon Oh. Her deepest encouragement and love supported me at all times. I am indebted to her for patience and trust.

Finally, there is no word in the world to express my deepest gratitude to my parents and brother. Their continuous love, sacrifice, support, blessings and encouragement guided me during time in UCLA. I pray for their health and happiness. I also thank to my grandparents, uncles, aunts and cousins for having me wonderful memories. Especially, uncle Kwanghwa gave me advice for academic life.

VITA

2007-2009	Master of Science, Electrical Engineering
	University of California, Los Angeles, United States
2001- 2007	Bachelor of Science, Electrical Engineering
	Korea University, Seoul, Korea

PUBLICATIONS AND PRESENTATIONS

K. Park, J. Li, Z. Deutsch, D. Oron, V. Shvadchack, S. Weiss, “Voltage sensing inorganic nanoparticles”, ICP 2013, Leuven, Belgium, Jul., 2013

K. Park, Z. Deutsch, J. Li, D. Oron, V. Shvadchack, S. Weiss, “Voltage sensing inorganic nanoparticles”, Cold Spring Harbor Conferences, Suzhou, China, May, 2013

K. Park, “Delivery of nanorod into the cell membrane”, ACS meeting, New Orleans, Apr, 2013

K. Park, Z. Deutsch, J. Li, D. Oron, S. Weiss, “Single Molecule Quantum Confined Stark Effect Measurement of Semiconductor Nanoparticles at Room Temperature”, SPIE photonics west, San Francisco, Feb 2013

K. Park, Z. Deutsch, J. Li, D. Oron, S. Weiss, “Single Molecule Quantum Confined Stark Effect Measurement of Semiconductor Nanoparticles at Room Temperature”, ACS Nano, 2012

P. Narayanan, **K. Park**, C. O. Chui, C. A. Moritz, “Validating Cascading of Crossbar Circuits with an Integrated Device-Circuit Exploration”, IEEE/ACM Symposium on Nanoscale Architectures, San Francisco, 2009

P. Narayanan, **K. Park**, C. O. Chui, C. A. Moritz ”Manufacturing Pathway and Associated Challenges for Nanoscale Computational Systems”, IEEE NANO, Genoa, Italy, 2009

Chapter 1

Introduction

Understanding a brain is one of the greatest scientific challenges. A brain consists of approximately one billion neurons and each neuron connects to one thousand neighbor neurons, communicating each other with electricity. Since this network is hard to access, scientists utilize noninvasive tools such as Electroencephalography (EEG) and functional magnetic resonance imaging (fMRI) to study the neural activity and functionality. They provide structural and functional information, related with neural activity, but do not provide high spatio-temporal resolution information[1, 2]. Therefore, there is a fundamental underlying limitation to understand a brain's microcircuitry. Invasive recording methods, on the other hand, can provide high temporal resolution data, but lack the needed spatial resolution and throughput. For example, action potential (AP) from a single site (and ion currents generated even from a single ion channel) could be recorded with the help of a voltage-clamped glass micropipette electrode (having a tip diameter as fine as 10 nm)[3]. Such micropipette electrodes serve as the basis for traditional electrophysiology. However, such electrodes are invasive and are not suitable for multi-site investigation of- (or interfacing to-) neural network due to their bulkiness. Nanotechnology fabrication methods have been recently used to produce arrays of small electrodes that are less invasive and provide higher resolution and higher throughput measurements[4]. Such arrays could possibly find applications in brain research and in the construction of brain-machine interfaces (BMIs) that could possibly restore one day central nervous system (CNS) functions in patients with paralysis or other neurological disorders, or monitor and influence cognitive functions.

Optical recording of neuronal activity could in principle avoid problems associated with electrodes, i.e. it could afford non-invasive, multi-site recordings, with high spatial resolution. Fluorescence imaging of Ca^{2+} ions is indeed such a popular optical recording method, but it suffers from a low temporal resolution since membrane depolarization events are only indirectly reported by changes in Ca^{2+} concentration that follow a complex cascade of changes in states of ion pumps, channels, and buffers[5]. For this reason, Ca^{2+} imaging cannot fully temporally resolve hyperpolarizations and subthreshold events.

Direct imaging of action potentials with fluorescent voltage-sensitive dyes (VSDs) could provide a better solution for optical recording of neuronal activity with higher temporal and spatial resolutions. VSDs suffer, however, from several disadvantages: (i) they display relatively small (5-20%) fluorescence intensity ($\Delta F/F$) change; (ii) fast-responding VSDs have low $\Delta F/F$; (iii) slow-responding VSDs are too slow to capture action potentials due to capacitive loading; (iv) VSDs rapidly internalize into cells; (v) excitation/emission wavelengths of many VSDs are in the blue/green range, preventing work deep in tissues and organs (due to absorption and scattering); (vi) single-cell/monolayer imaging suffers from dye phototoxicity and low $\Delta F/F$.

Although several greatly improved VSDs have been recently introduced[6], including genetically encoded voltage sensors [7, 8, 9] development of even better performing VSDs is needed.

Therefore, I aimed to develop the semiconductor voltage sensitive nanoparticles (vsNPs) that self-insert into the cell membrane and optically record, non-invasively, action potential at the single-particle and nanoscale level, at multiple sites, in a large field-of-view. It detects voltage or AP *via* quantum-confined Stark effect (QCSE). This phenomenon describes the optical transition change including wavelength shift, lifetime change and intensity change, induced by external electric field. It could offer unique advantages for AP recording, since NPs (i) display much larger voltage sensitivity than conventional voltage-sensing dyes (VSDs); (ii) are very bright and afford single-molecule detection (due to a large one-photon excitation cross-section and high quantum yield); (iii) display a large spectral shift as function of voltage (affording a noise-immune ratiometric measurements); (iv) have a very fast (ns) response; (v) do not bleach; (vi) have very large Stokes shift; (vii) have a large two-photon cross sections; (viii) have excellent performance in the NIR spectral range; (ix) afford superresolution imaging *via* methods such as fluctuation imaging; (x) can be used at very low concentration. If materialized, it could revolutionize the fields of neurobiology, cardiology, and muscle physiology.

In this Chapter, basic backgrounds underlying in my research are overviewed. Chapter. 1.1 introduces semiconductor nanoparticle and history of development. Chapter 1.2 discusses QCSE in the context of perturbation theory. Chapter 1.3 introduce the **k·p** method and optical transition calculation in semiconductor. Chapter 1.4 introduces Auger recombination in semiconductor.

1.1 Semiconductor nanoparticle

As semiconductor materials shrink in nanometer scale, especially smaller than exciton Bohr's radius, unique electronic property emerges[10]. This semiconductor nanoparticle (NP) is often called as quantum dot (QD, spherical) or nanorod (NR, elongated shape) and its electronic properties are intermediate between a bulk semiconductor and an atom[11]. The quantum confined effect explains the atomic like energy separation although it is not atom. A QD is simply modeled as a particle in a box where energy levels are determined by the QD's size. Therefore optical bandgap, *i.e* transition energy between the electron in the ground state in conduction band to the hole's ground state in valence band, is changed by its size[12]. This size dependent energy gap enables tunable fluorescence emission wavelength (Fig. 1.1)

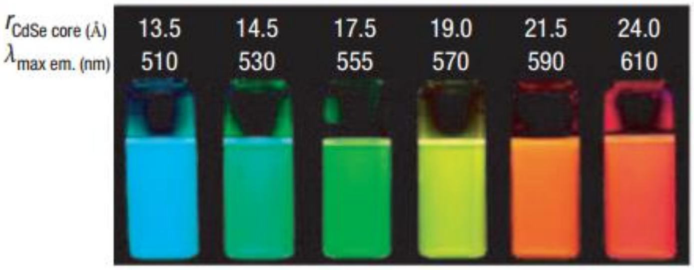

Fig. 1. 1 CdSe emission fluorescence[10]

In addition to this, density of states (DOS) changes in nanoscale material. Fig. 1.2 shows DOS in semiconductor material. As semiconductor is scaled down to the nanometer dimension, it accompanies increased DOS at the lowest energy state. For QD (0D material, confined all three direction), δ-function like density of states (DOS) appears as compared to parabolic DOS in three dimensional (3D) semiconductor ($DOS_{3D} \propto \sqrt{E}$) (Fig. 1.2).

Due to the largest DOS at the lowest energy, it possesses highly luminescent optical property. Therefore, it is highlighted for developing it as a light emitting diode (LED) or laser. QDs and NRs have other interesting optoelectronic, electrochemical and magnetic properties that are likely to be further exploited. Such NPs have found numerous applications, such as in biological tagging[13], quantum optics[14], photovoltaic light harvesting,[15] flat panel displays[16] and others.

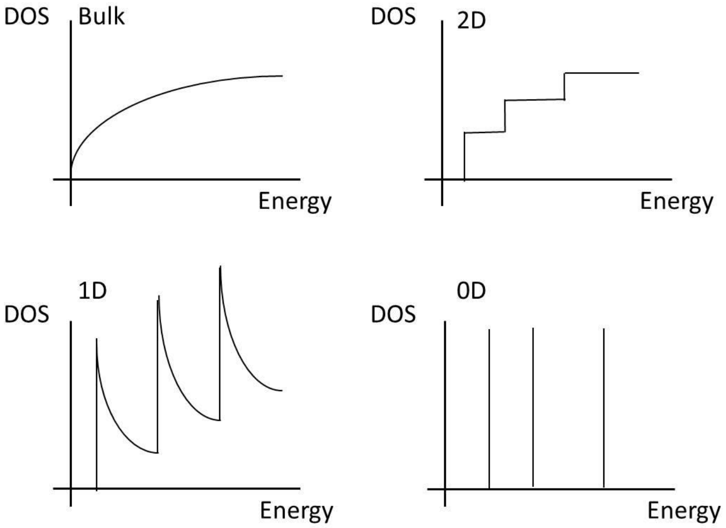

Fig. 1. 2 Density of states of semiconductor

Colloidal QDs or NRs are nucleated from a hot solution of precursor molecules. Their size and shape can be precisely controlled by the duration, temperature, and ligands used in the synthesis[17, 18, 19]. This method yields QDs or NRs that have composition and size-dependent absorption and emission wavelengths covering the entire spectral range from the visible to the NIR regions[20].

The growing number of novel applications stems from the ever-increasing control over QDs' and NRs' optical and electronic properties, afforded by dramatic improvements in synthetic protocols. Significant advancements include shape control *via* addition of co-adsorbents[21], allowing the fabrication of quantum rods and tetrapods, and synthesis of core/shell nanocrystals with type-I and type-II band alignments[22]. Combination of these synthetic techniques has afforded the fabrication of asymmetric heterostructures *via* seeded nanorod formation[23, 24] where a CdSe or a ZnSe core is embedded in one end of a CdS rod, exhibiting strongly asymmetric localization regimes for the electrons and the holes. Type-II QDs have been shown to have controllable exciton-exciton interaction energies[25], which is of particular interest for optical gain[26] and light harvesting[15] applications. Nucleation doping, a recent addition to the synthesis toolbox, enables formation of shallow traps for one charge carrier within the QD or NR, affording a controlled separation of charges inside the nanoparticle[27].

The intricate control over size, shape, shell thickness, doping, heterostructure and band alignment allows precise engineering of the carriers' wavefunctions, and in particular, their interactions with (and perturbation by) the immediate local environment. As a result, QDs and NRs have been increasingly used as local probes of their nanoscale environment. Examples include sensing of chemical properties such as pH[28], anion[29] and ion detection[30], and physical properties such as light intensity,[31] temperature[32], stress[33] and surface charge[34].

1.2 Quantum-confined Stark effect

Franz-Keldysh effect describes the electric field (*F*) dependent optical transition of semiconductor materials such as absorbance or emission spectrum change[35]. When *F* is applied to the semiconductor, triangular barriers are formed in the conduction band (CB) and valence band (VB). In this system, electron and hole's wavefunction leak through their triangular barriers *via* tunneling. Consequently, energy gap between leaked states is smaller than the actual bandgap, which results in wavelength red-shift ($\Delta\lambda > 0$) in absorption and emission spectra.

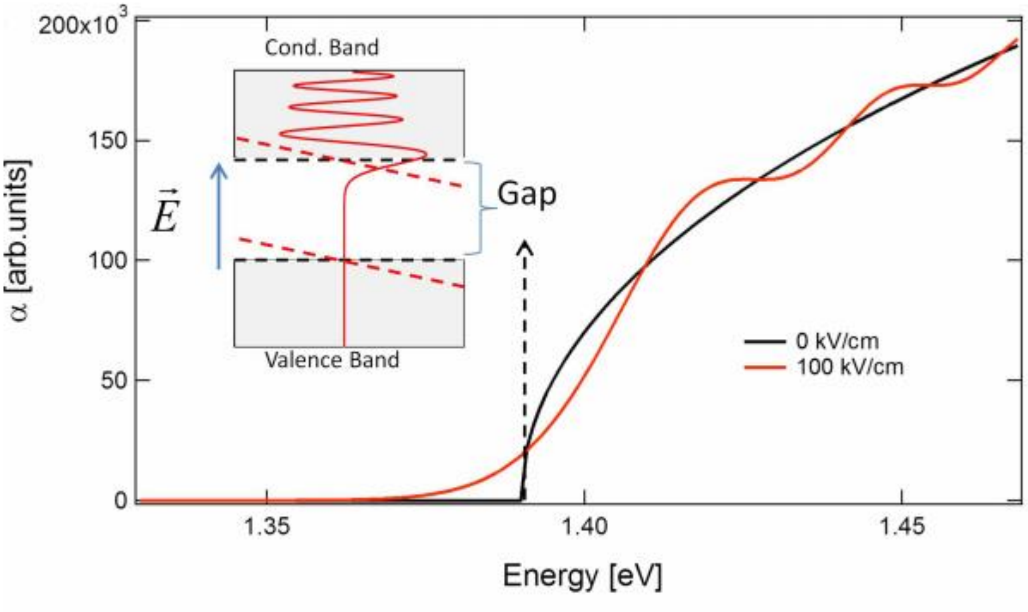

Fig. 1. 3 The Franz-Keldysh effect[33]

When an exciton is confined in nanoscale structure (smaller than a Bohr's radius), excitonic peak is more clearly visible compared to the bulk material, giving rise to the quantum confined Stark effect (QCSE)[36] (Fig. 1.4).

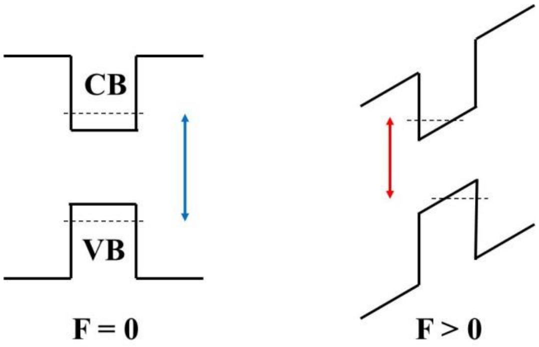

Fig. 1. 4 Quantum confined Stark effect

The Hamiltonian for this system is

$$
\begin{aligned}
H &= H_e + H_h + H_{e-h} \\
H_e &= \frac{-\hbar^2}{2m_e^*}\frac{d}{dz^2} + V_e(z) + eFz \\
H_e &= \frac{-\hbar^2}{2m_h^*}\frac{d}{dz^2} + V_h(z) - eFz \\
H_{e-h} &= \frac{-\hbar^2}{2\mu}\frac{d}{dr^2} - \frac{e^2}{4\pi|r|}
\end{aligned}
$$

where m_e^*, m_h^* are effective masses of an electron and a hole, μ is the reduced effective mass in the plane of the layer, V_e and V_h are potential energies for an electron and a hole. This is the complete Hamiltonian for the envelop function under effective mass approximation. This problem is often treated by the perturbation theory.

$$\{H_o + H'\}\psi_n = E_n\psi_n$$

$$H_o = \frac{\boldsymbol{p}^2}{2m^*_{e\ or\ h}} + V(z)$$

$$H' = eFz$$

H_o is unperturbed Hamiltonian of quantum well (QW), H' is perturbation from externally applied *F*. The first order correction is zero if QW is symmetric.

$$E_n^{(1)} = \left\langle \psi_n^{*(0)} \left| eFz \right| \psi_n^{(0)} \right\rangle = 0$$

The second order correction of the ground state becomes

$$E_1^{(2)} = \sum_{n\neq 1} \frac{\left\langle \psi_n^{*(0)} \left| eFz \right| \psi_1^{(0)} \right\rangle}{E_1^0 - E_n^0} \approx \frac{\left\langle \psi_2^{*(0)} \left| eFz \right| \psi_1^{(0)} \right\rangle}{E_1^0 - E_2^0} \approx \alpha F^2$$

By solving this, one can calculate ΔE_e, ΔE_h and total optical transition energy change ($\Delta E = \Delta E_e + \Delta E_h$). The strength of QCSE is characterized by electric polarizability (α [m^3], $\Delta E = \alpha F^2$). For example, α of QD having 5.8nm in diameter shows 2.38×10^5 $Å^3$ [37]and this value increases with the quantum well (or dot) size increase.

First QCSE was demonstrated in epitaxially grown two-dimensional quantum wells. 10 nm GaAs layer is sandwitched by AlGaAs layers and it shows 35 meV reduction in optical bandgap at 200 kV/cm[36]. This physical phenomena is exploited to construct the self-electrooptic-effect-device (SEED).[38] QCSE based SEED has advantages including low power consumption, high speed, easily integrated onto Si-based device or waveguide and room temperature (RT) operation[39].

1.3 The k·p method and Optical transition calculation

The **k·p** method is one such widely used method to calculate energy gaps and optical transition rate. By using this, energy structure near the high symmetric **k** points is conveniently calculated. Extrapolating from these points, one can obtain the energy structure in the entire Brillouin zone with band dispersion and effective mass. The **k·p** method is also used to calculate the optical transition induced by electromagnetic field. Both absorption and emission rate in semiconductor is calculated with this method.

The simplest picture of the **k·p** model is nondegenerate one band. Single particle Schrödinger equation is

$$\left\{\frac{\boldsymbol{p}^2}{2m}+V(r)\right\}\psi_{nk}=E_{nk}\psi_{nk}$$

$$\psi_{nk}=u_{nk}(r)\exp(ik\cdot r) \qquad \cdots \textit{Bloch function}$$

where V(r) is atomic periodic potential, u_{nk} is the periodic part of the Bloch function, n is the band index, k is wave vector within the first Brillouin zone. Above equation can be expressed with only atomic part of the Bloch function,

$$\left\{\frac{\left(\boldsymbol{p}+\hbar\boldsymbol{k}\right)^2}{2m}+V(r)\right\}u_{nk}=E_{nk}u_{nk}$$

This can be simplified as

$$\left(H_0 + H_1 + H_2\right)u_{nk} = E_{nk}u_{nk}$$

$$H_1 = \frac{\hbar}{m}\boldsymbol{k}\cdot\boldsymbol{p}, \qquad H_2 = \frac{\hbar^2\boldsymbol{k}^2}{2m}$$

The simplest solution of this equation is obtained by non-degenerate perturbation theory. The first and second order correction of the eigenvalues become

$$E_{nk} = E_{n0} + \frac{\hbar}{m}\boldsymbol{k}\cdot\left\langle n_0\left|\boldsymbol{p}\right|n_0\right\rangle + \frac{\hbar^2\boldsymbol{k}^2}{2m} + \frac{\hbar^2}{m^2}\sum_{m\neq n}\frac{\left|\boldsymbol{k}\cdot\left\langle m_0\left|\boldsymbol{p}\right|n_0\right\rangle\right|^2}{E_{n0} - E_{m0}}$$

For most semiconductors, energy bands are symmetric at k = 0 points. Thus, linear dependence in **k** term becomes zero. The effective mass expression gives

$$E_{nk} = E_{n0} + \sum_{i,j}\frac{\hbar^2}{2m_{i,j}^{\ *}}k_i k_j$$

$$\frac{m}{m_{i,j}^{\ *}} = \delta_{ij} + \frac{2}{m}\sum_{m\neq n}\frac{\left\langle n_0\left|\boldsymbol{p}_i\right|m_0\right\rangle\left\langle m_0\left|\boldsymbol{p}_j\right|n_0\right\rangle}{E_{n0} - E_{m0}}$$

where m^* is a second-order tensor, i, j are Cartesian indices.

Electronic states of conduction and valence band, and optical transition between these two states are one frequently calculated with this method. The two band model considers the nondegenerate $\left|s\right\rangle$ like conduction band at Γ, and three degenerate bands $\left|p_x\right\rangle, \left|p_y\right\rangle, \left|p_z\right\rangle$ at valence bands. For $\left|s\right\rangle$ band, most matrix elements become zero except $\left\langle s\left|\boldsymbol{p}_x\right|p_x\right\rangle, \left\langle s\left|\boldsymbol{p}_y\right|p_y\right\rangle, \left\langle s\left|\boldsymbol{p}_z\right|p_z\right\rangle$ due to the symmetry, so it becomes

$$\frac{m}{m_{CB}{}^{*}} = 1 + \frac{2}{m}\frac{|P|^2}{E_g}$$

and for light hole,

$$\frac{m}{m_{VB}{}^{*}} = 1 - \frac{2}{m}\frac{|P|^2}{E_g}$$

This tells us that narrow gap semiconductor has small effective mass at both bands. As the electronic state deviates from the **k** = 0 value, it couples with different bands *via* the **k·p** term in matrix, resulting in band dispersion (effective mass).

Interestingly, the momentum matrix element also appears in calculating interaction with electromagnetic field. The electron interacts with the electric and magnetic field of the electromagnetic radiation. The Hamiltonian describes this

$$\begin{aligned} H &= \frac{1}{2m}(\boldsymbol{p} - q\boldsymbol{A})^2 + e\phi + V(r) \\ &= \frac{\boldsymbol{p}^2}{2m} - \frac{q}{2m}(\boldsymbol{p}\cdot\boldsymbol{A} + \boldsymbol{A}\cdot\boldsymbol{p}) + \frac{e^2\boldsymbol{A}^2}{2m} + e\phi + V(r) \end{aligned}$$

It is further simplified as

$$\begin{aligned} H &= \frac{\boldsymbol{p}^2}{2m} + V(r) - \frac{q}{m}(\boldsymbol{A}\cdot\boldsymbol{p}) \\ H' &= -\frac{q}{m}(\boldsymbol{A}\cdot\boldsymbol{p}) \end{aligned}$$

and vector potential is written as

$$\boldsymbol{A} = \sqrt{\frac{\hbar}{2\omega\varepsilon V}}\left(b^{\dagger} + b\right)$$

where $b^{\dagger}$, and b are the photon creation and destruction operators. The Fermi golden rule describes the transition rate from the initial state $\left|i\right\rangle$ to the final state $\left|\, f\,\right\rangle$.

$$W = \int_{f} \frac{2\pi}{\hbar}\left|\left\langle f\left|H'\right|i\right\rangle\right|^{2}\delta(E_f - E_i)dS_f$$

Since we are interested in transition between conduction and valence band, Fermi golden rule becomes

$$W_{abs} = \frac{2\pi}{\hbar}\frac{q^2}{m^2}\left(\frac{\hbar n_{ph}}{2\omega\varepsilon}\right)\left|\int \psi_f^*(a\cdot\boldsymbol{p})e^{ik_{ph}\cdot r}\psi_i\,dV\right|\delta(E_i - E_f + \hbar\omega)$$
$$W_{ems} = \frac{2\pi}{\hbar}\frac{q^2}{m^2}\left(\frac{\hbar(n_{ph}+1)}{2\omega\varepsilon}\right)\left|\int \psi_f^*(a\cdot\boldsymbol{p})e^{ik_{ph}\cdot r}\psi_i\,dV\right|\delta(E_i - E_f - \hbar\omega)$$

where a is unit vector of **A**. The transition due to the photon are 'vertical', so we can neglect the k_{ph} contribution (dipole approximation). Thus, the matrix element becomes

$$P_{if} = -i\hbar\int \psi_{k_f,n}^{*}\nabla\,\psi_{k_i,m}dV$$

and this is called optical matrix element, having the same form as momentum matrix element. The oscillator strength measures the strength of transition, defined by

$$f_{if} = \frac{2}{m}\frac{\left|P_{if}\right|^2}{E_g}$$

$$\sum_{i\neq f} f_{if} = 1 - m / m_f^*$$

P_{if} value for IV, and III-V and II-VI semiconductor are quite similar $2P^2/m \approx 20$ eV.

Although NP is 0D structure, we can get enough intuition of optical transition by projecting it to quantum well (QW) structure (2D). In 2D QW, wavefunction is described as

$$\psi = \frac{1}{\sqrt{AW}} e^{ik\cdot\rho} g_{c,v}^{n}(z) u_{c,v}^{n}(\rho)$$

where A is area and W is width and c is conduction band and v is valence band and n is subband and g(z) is envelope function perpendicular to the QW and *u(ρ)* is parallel to the QW. Then, it becomes

$$P_{if} = \frac{-i\hbar}{AW} \left\langle g_v^m \mid g_c^n \right\rangle \int e^{i(k_c - k_h)\cdot\rho} \left\langle u_v^m \left|\nabla\right| u_c^n \right\rangle d\rho^2$$

where m and n represent subband indices, $\left\langle g_v^m \mid g_c^n \right\rangle$ is called the overlap integral. The overlap integral is the direct measure of the transition strength of QW and also frequently used to compare the radiative transition rate in QD.

1.4 Auger recombination

Auger recombination is three particle scattering process. It describes two electrons (or two holes) collision in the vicinity of a spectator hole (or electron) and energy relaxation to the spectator particle (Fig. 1.5). Therefore, no energy is relaxed as a form of photon. Compared to the bulk semiconductor, Auger recombination in NPs is not negligible, instead it is one dominant transition in NPs. Since Auger rate (k_A) is orders of magnitude larger than the radiative process (k_r) for most NPs, NPs at trion state (X^+, Fig. 1.5b) become completely 'dark', emitting suppressed number of photons before they are neutralized to single exciton state (X). The random occurrence of charging and uncharging brings NPs' emission intermittency, called blinking (Fig. 1.5c)[40, 41].

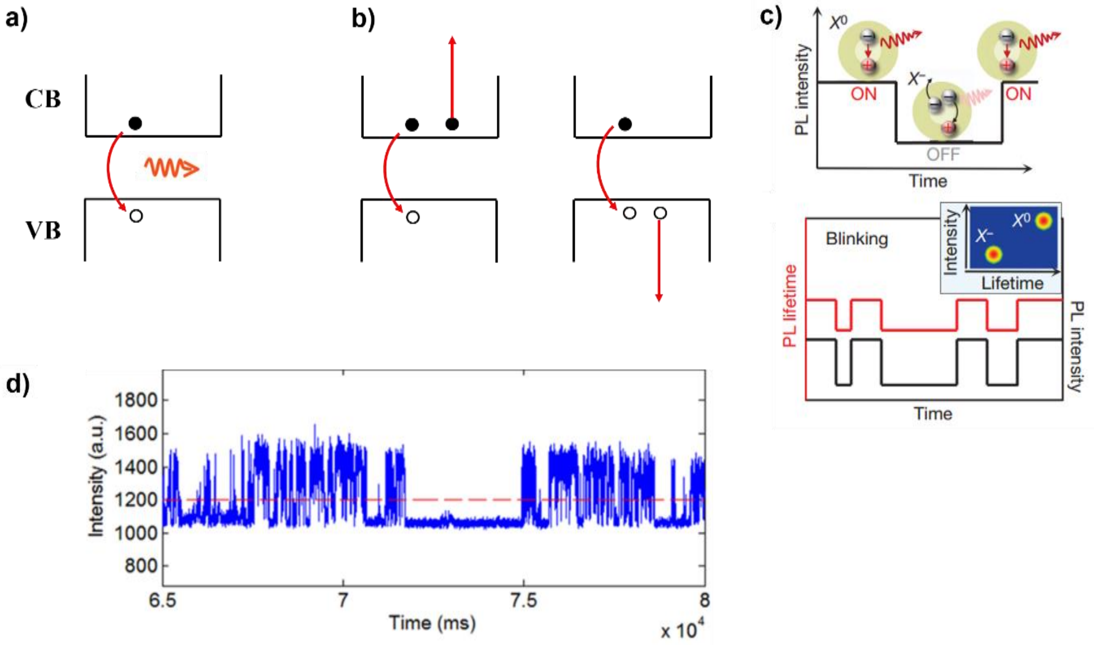

Fig. 1. 5 Optical transition (a) radiative recombination (b) Auger recombination (c) Emission intermittency due to charging and uncharging of NPs.[38] (d) Quantum dot blinking[39]

The Auger rate is calculated by Fermi golden rule:

$$k_A = \frac{1}{\tau_A} = \int_f \frac{2\pi}{\hbar} \left| \langle f | H' | i \rangle \right|^2 \delta(E_f - E_i) dS_f$$

$$H' = -\frac{q|r|}{4\pi\varepsilon_r\varepsilon_o}$$

In this study, we are interested in Auger recombination rate change by external electric field. Thus, it is discussed in the context in QCSE in Chapter 3. In addition, it helps to estimate the trion state's quantum yield (QY) in Chapter 4. Calculation detail of Auger recombination rate is discussed in Chapter 3.

Chapter 2

Single molecule quantum-confined Stark effect (QCSE)

2.1 Introduction

To validate semiconductor nanoparticle's (NP) voltage sensing ability, quantum-confined Stark effect (QCSE) measurement was performed for eight different NPs. Unlike the previously performed experiments, I aimed to resolve QCSE at single molecule level (instead of ensemble measurement) at room temperature (RT) since actual action potential (AP) detecting will occur at live cell at RT. However, resolving QCSE of colloidal NPs at room temperature (RT) is challenging for several reasons. At RT, an exciton is readily ionized, and emission spectrum is thermally broadened which prevent from resolving the spectrum shift. Trapping of random thermally excited charges at surface-and interface-states can cause local potential fluctuations that interfere with and modulate charge separation, thus adding spectral noise. In addition, externally applied electric field (*F*) is not fully transferred to the internal *F* under NPs at glass-air environment due to the large dielectric mismatch. Normally colloidal NPs are located onto the cover glass, exposed to air (ε_r = 1) or buried in the polymer matrix (ε_r of PMMA is 2.6) when measured. Due to the large dielectric mismatch between NPs (ε_r is usually close to 10) and their environment, electric field is dropped near the NPs surface. In this dielectric configuration, internal *F* is only 10~30 % of the external *F*. In addition, image charges forms such that they oppose the exciton separation, which is called dielectric confinement [42].

QCSE in epitaxially grown 2D quantum wells is more readily observable, compared to the colloidal NPs. This is because the induced *F* is larger when the dielectric mismatch is small between confined layer and surround layers. For example, a wavelength shift of 15 nm was measured (shift from 610 nm at 5 V to 625 nm at 10 V) at 197 ^{o}k ($\Delta\lambda/\lambda$ = 2.40 % for ΔF = 119 kV/cm).[43] For type-II band alignment, even larger changes were measured ($\Delta\lambda$ = 85 nm, $\Delta\lambda/\lambda$ = 7.14 % for ΔF = 80 kV/cm).[44] Nonetheless, the advent of colloidal QD synthesis led to extensive examination, mostly at low temperature (LT), of their QCSE[37]. Wavelength shifts of type-I NPs are usually small ($\Delta\lambda$ = 6.0 nm, $\Delta\lambda/\lambda$ = 1.0 % for ΔF = 350 kV/cm)[45]. Larger shifts were measured for type-II NRs ($\Delta\lambda$ = 4.2 nm, $\Delta\lambda/\lambda$ = 0.65 % for ΔF = 30 kV/cm)[46] but in ensemble measurement. To the best of our knowledge, there is no study reported, resolving QCSE of a single NP at RT.

In order to resolve single molecule QCSE of colloidal NPs at RT, I built custom *F*-modulation microscopy setup where *F* is alternatively modulated by the automated control program. It is more robust to the spectral noise, and provide the statistical analysis. Secondly, I narrowed the electrode gap as much as UCLA Nanoelectronics Research Facility allows (2 μm). Lastly, I synthesized new type-II NRs, which is designed to enhance QCSE by separating exciton.

2.2 Overview of NPs

	Sample	Energy band		E_g [eV]	λ_{ems} [nm]	TEM picture, scale bar is 20nm
		V=0	V>0			
Type-I	#1	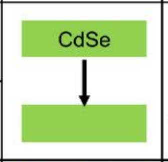	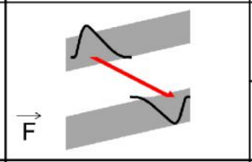	2.00	621	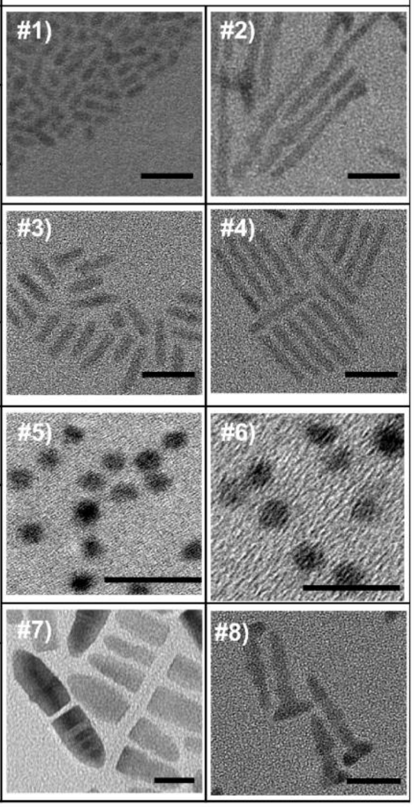
	#2			1.95	637	
Quasi Type-II	#3	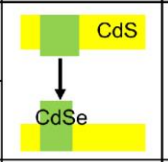	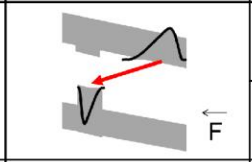	2.26	550	
	#4			2.18	570	
Type-II	#5	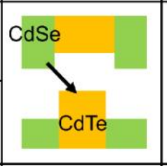	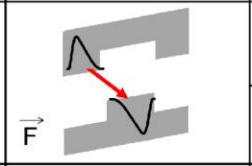	1.84	675	
	#6			1.74	712	
	#7	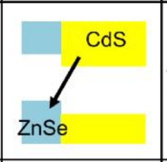	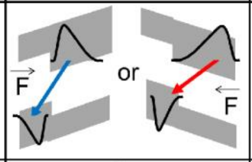	2.07	600	
	#8	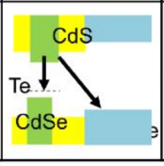	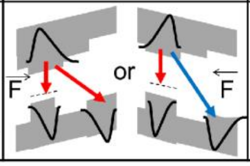	T-I :1.7 T-II:1.97	730 630	

Table 2.1 List of studied samples and their relevant attributes. E_g and λ_{ems} are the respective NP's optical bandgap and peak emission wavelength. Black arrow represents a radiative recombination pathway without F. When F is applied, λ_{ems} is either increased (red arrow) or decreased (blue arrow) depending on the NPs' composition and its relative orientation with respect to the direction of F. Transmission electron microscopy (TEM) micrographs of all samples are shown on the right panel.

Eight NPs of different geometries, band alignment structures and compositions were surveyed for their QCSE (Table 2.1). Colloidal synthesis is introduced in Ch. 2.8. Samples were of either type-I or type-II band alignment, homostructures or heterostructures, and of either sphere or rod shapes. Table 2.1 describes the attributes of these samples and includes their transmission electron microscopy (TEM) micrographs. Average sizes of the various samples were evaluated from TEM images (from 30 NPs or more each) and are summarized in Table 2.2 Sample #1 and #2 are homogeneous CdSe NRs with different lengths (7.7 nm and 43.4 nm on average, respectively). Sample #3 and #4 are quasi type-II CdS NR heterostructures with CdSe QDs as seed with different rods' lengths (12.8 nm and 29.0 nm respectively), where electrons are delocalized across the entire NR while the holes are localized on CdSe seed. Sample #5 and #6 are CdTe/CdSe core/shell type-II QDs having different core sizes and shell thicknesses. Samples #5 has a 4.2 nm CdTe core and a 2-layer CdSe shell and sample #6 has a 3.9 nm CdTe core and a 5-layer CdSe shell. Sample #7 is an asymmetric type-II heterostructure composed of ZnSe sphere embedded in a thick bullet-shaped CdS NR (seeded NR). Its length is 33.7nm and width at the thicker waist is 12.1nm. We note that sample #8 is a novel formulation with a barrier inserted inside a type-II gap and was only recently described in the context of quantum optics application[47]. Particles are hammer-shaped, 28.0nm long and 5.0nm wide at the 'handle'. Excitons in this sample have two recombination pathways, one from the conduction band of CdSe to the Te dopant level (spatially direct gap, 730 nm transition) and the other from the conduction band of CdSe to the valence band of CdZnSe (spatially indirect gap, 630 nm transition). The 730 nm emission is due to a type-I transition, while the 630 nm emission is the manifestation of an enhanced type-II transition since the electron and the hole reside in two wells that are separated by a CdS barrier. Interestingly, the spectral bandwidth of the type-II transition is much narrower than the spectral bandwidth of the type-I transition. Unlike previously observed linewidth differences in two color emitting CdSe/ZnS/CdSe core/barrier/shell systems,[48] this is probably due to stronger phonon coupling of the type-I transition due to the strong hole localization in the doped core[47]. Both samples #7 and #8 are asymmetric type-II NPs. As discussed below, and elsewhere,[49],[50] the spectral shift dependences on the applied field are expected to be different for these samples as compared to type-I, quasi type-II and symmetric type-II QDs and NRs (samples #1 - #6).

Table 2.2 | Statistical size characterization of sample #1 - #8 (Unit is nm).

Sample	#1	#2	#3	#4	#5	#6	#7	#8
Length	7.7±0.9	43.4±7.9	12.8±1.5	29.0±2.1	5.0±0.8	6.0±0.9	33.7±4.2	28.0±4.9
Width	2.9±0.3	4.2±0.4	3.7±-0.4	4.0±0.4			12.1±2.3	5.0±0.4

2.3 QCSE results

QCSE results for Type-I and quasi type-II NPs (samples #1 - #4)

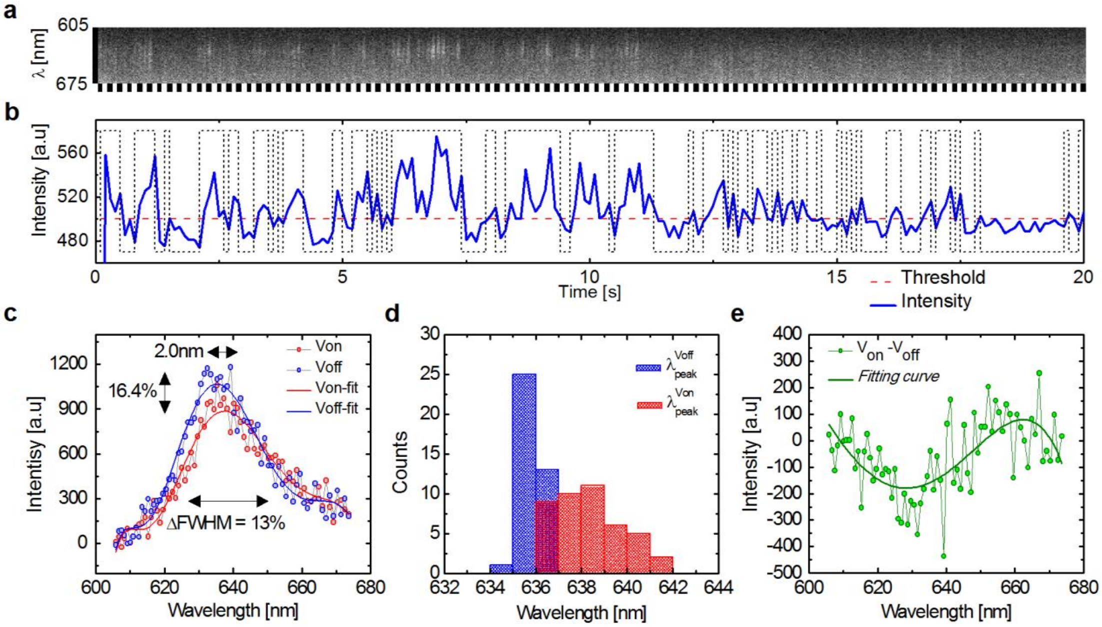

Fig. 2.1 Single NP QCSE analysis of sample #2. **(a)** A series of 200 successive spectra obtained from sample #2 at RT (excitation intensity 2 mW/cm^2, electric field modulation frequency 10 Hz, single frame integration of 0.1 s). The dashed white/black line at the bottom of the Fig. indicates the periods at which the applied electric field was on (V_{on}= 400 kV/cm, white) or off (V_{off} = 0 kV/cm, black); **(b)** Integrated intensity trajectory (integration over λ for each frame) of the data shown in **(a)** (solid blue). The dashed red line is a guide to the eye emphasizing the blinking-on and blinking-off intensity states; **(c)** Averaged V_{on} frames (red) and averaged V_{off} frames (blue) (after filtering for frames in the blinking-on state) with corresponding 7th order polynomial fits (solid red and blue respectively); **(d)** A histogram of spectral peak positions (V_{on} red, V_{off} blue) from all blinking-on frames (derived from the polynomial fits); **(e)** Differential emission spectra derived from **(c)**

RT QCSE results for CdSe NRs (sample #2) are shown in Fig. 2.1. The Fig. shows 200 successive spectra of a single NR. As clearly shown in Fig. 2.1a and 2.1b, the seeded NR exhibited fluorescent intermittency (blinking)[51,52,53,54] with a typical blinking-on / blinking-off telegraph noise-like intensity values. Only frames during blinking-on periods were retained for further analysis using a threshold filter (Fig. 2.1b).

Fig. 2.1c shows sample #2's average spectra (over the whole movie) for V_{off} and V_{on}, where the latter is red-shifted with respect to the former by 2.0 nm, corresponding to $\Delta\lambda/\lambda = 0.32\%$. Concomitant with the spectral shift, a 16.4% decrease in the peak emission intensity and a 13% increase in the FWHM of the emission peak were observed (Fig. 2.1c) based on the fitted curves. Beyond averaging these properties over the whole movie (20s, Fig. 2.1c), we also analyzed the spectral shifts for individual frames (0.1s each, Fig. 2.1d), by extracting emission peak wavelength (λ_{peak}) for each frame (in the blinking-on state) and separately histogramming the V_{off} and V_{on} frames (Fig. 2.1d). This analysis yields λ=635.9±0.5 nm and λ=638.4±1.4 nm for V_{off} and V_{on} respectively, with a red shift $\Delta\lambda$=2.5 nm (as compared to $\Delta\lambda$= 2.0 nm in Fig. 2.1c). The difference between Fig. 2.1c and 2.1d is originated from the fitting errors and their accumulation. Fig. 2.1e shows the difference between the two spectra in Fig. 2.1c.

The averaged V_{off} and V_{on} spectra (Fig. 2.1c), the histograms of V_{off} and V_{on} peak wavelength (Fig. 2.1d), the shape of the differential spectra (Fig. 2.1e), clearly demonstrate spectral red-shift and spectral broadening due to the applied external field, which are hallmarks of the QCSE and a manifestation of the exciton's charge separation, reflecting the build-up of an internal electric field (dipole) that opposes the external applied field.

A more pronounced QCSE was measured for sample #4 (Fig. 2.2), with noticeable spectral and integrated intensity changes (Figs. 2.2a and 2.2b; notice the saw tooth signal in Fig. 2.2b). The average spectral shift $\Delta\lambda$ was measured to be 4.4 nm ($\Delta\lambda/\lambda = 0.77\%$). A 30.2% decrease in peak intensity and 28.1% increase in FWHM were observed (Fig. 2.2c). These numbers represent a QCSE which is about twice as big for sample #4 as compared to sample #2. The peak spectra (λ_{peaks}) histograms for V_{off} and V_{on} are λ=568.7±0.3 nm and λ=573.9±1.2 nm, and are clearly separated (Fig. 2.2d), displaying a red shift of Δλ=5.23 nm (as compared to Δλ= 4.4 nm in Fig. 2.2c). However, majority of sample #4 NPs displayed smaller shifts.

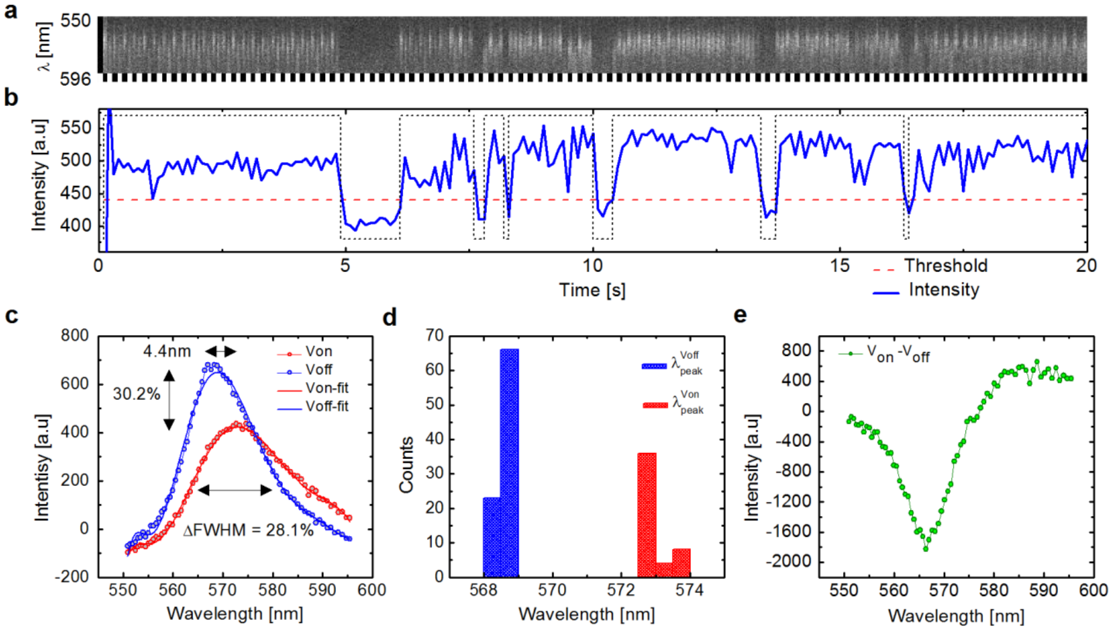

Fig. 2.2 Single NP's QCSE analysis of sample #4, presented in the same format as in **Fig. 2.1**

It is apparent from the spread (and the overlap) of the V_{off} and V_{on} histograms that the magnitude of the Stark effect varies from NR to NR, likely due to several reasons: (i) the orientation of NRs with respect to the applied field (due to only partial alignment); (ii) inhomogeneities in NRs' structure and size; (iii) presence of defects and/or traps on NRs surfaces and interfaces; (iv) presence of random surface charges on the supporting slide in close proximity to the NRs, and others. Charge trapping due to (iii) or (iv) could stochastically (and temporally) modulate the QCSE and result in static or dynamic broadening (spectral diffusion). The fast ionization of the exciton at RT, the observed inhomogeneities and the activation of trap states reduce the observed effect at RT as compared to low temperature (LT). Nonetheless, Fig. 2.1 and 2.2 show that although the effect is very small for these samples, it still can be measured at RT, on the single particle level, and therefore it should be possible to screen a library of different NPs for the optimal structure, shape, size, composition and band-alignment in order to yield a larger QCSE at RT.

The experiments described in Figs. 2.1 and 2.2 were repeated tens of times for each of the samples in Table 2.1 such that statistically meaningful QCSE data could be histogrammed from many individual NPs. Fig. 2.3 shows histograms for samples #1 - #4. Samples were subjected to the alignment procedure during deposition on the coverslip (Chapter 2.8) except for the data described in Fig. 2.3e (serving as a control for alignment).

Samples #1 and #2 are homogeneous NR with different diameter × length dimensions: 2.9×7.7 nm and 4.2×43.4 nm respectively. If electron and hole separation is extended throughout the length of the NR, sample #2 should yield a larger shift than sample #1. We observe, however, similar average shifts ($\Delta\lambda=0.6\pm1.2$ nm, $\Delta\lambda=0.6\pm1.4$ nm) for both samples, suggesting incomplete charge separation along the long axis of the NRs.

NPs with the structure, shape, and materials' compositions of samples #3 and #4 (CdSe/CdS seeded rods) were previously reported to have: (i) a high photoluminescent quantum yield (QY) (75% at RT[55]); (ii) a high degree of emission polarization;[55] (iii) an aspect-ratio (or length) dependent QCSE[56] at LT; and (iv) an efficient charge separation at RT.[57] These attributes make these NPs ideal for studying length and orientation dependent QCSE. However, in contrast to the reported LT results, we could not detect statistically significant differences in Stark effects for aligned ($\Delta\lambda$=0.7±1.4 nm) and non-aligned ($\Delta\lambda$=0.6±1.2 nm) samples (Figs. 2.3d and 2.3e), although polarization measurements suggested otherwise (Fig. S2.5). We could not detect statistically significant differences in wavelength shifts for the two different lengths and aspect ratios either (average shifts were around ~0.7 nm with 4.0 nm outliers, Figs. 2.3c, d). A possible explanation for this observation is miss-classification of the CdSe/CdS interface as a quasi type-II. The conduction band offset (Δe) of CdSe/CdS could vary in the range 0.00 eV to 0.30 eV[58] (depending on geometry and strain) while the valence band offset (Δh) is estimated to be 0.78eV. If core diameters are larger than 2.8nm, it could possibly still be confined to the CdSe seed, therefore reducing the extent of charge separation.

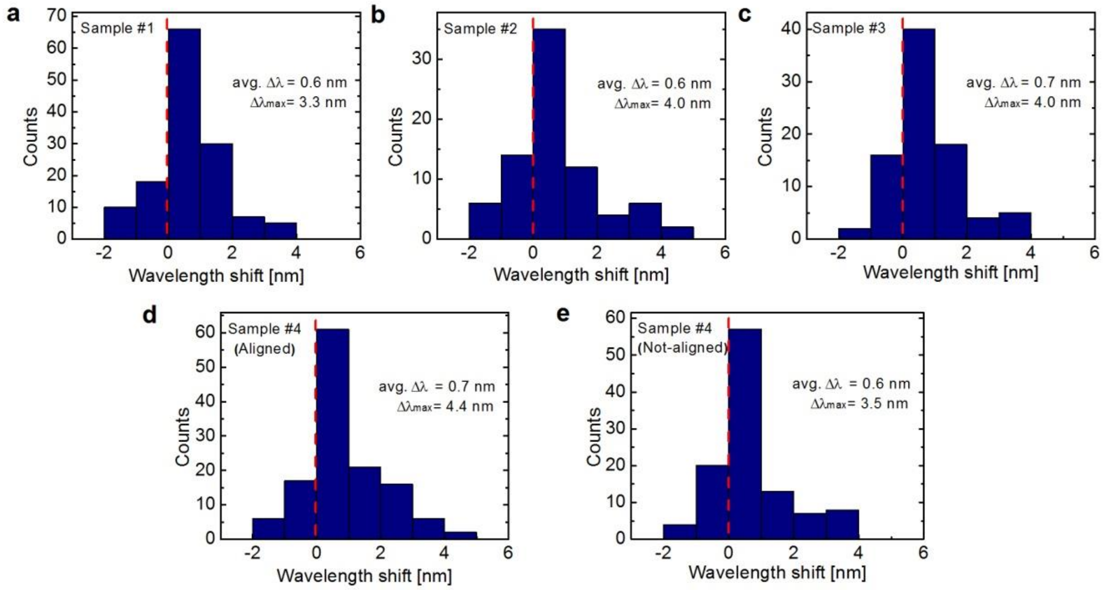

Fig. 2.3 Wavelength shift (Δλ) histograms for: **(a),** Sample #1; **(b),** Sample #2; **(c),** Sample #3; **(d),** Sample #4; **(e),** Sample #4; Measurements (**a**~**d**) are for aligned samples. **(e),** non-aligned Sample #4 (serving as a control).

It is noted that all histograms in Fig. 2.3 have tails with negative values (representing QCSE blue shifts), consisting of approximately 15% of all measured NPs. These are likely due to built-in dipole moments induced by random surface charge configurations that cancel-out the external field and generate a residual field in the opposite direction[37]. Shifts from such random charges are estimated to contribute ‘noise’ of about ±2 nm to the QCSE measurements. We conclude that the extent of charge separation at RT in samples #1 - #4 (homogenous and quasi type-II structures) is small and does not (or very weakly) depend on NRs length or orientation.

QCSE results for Type-II NPs (samples #5 - #8)

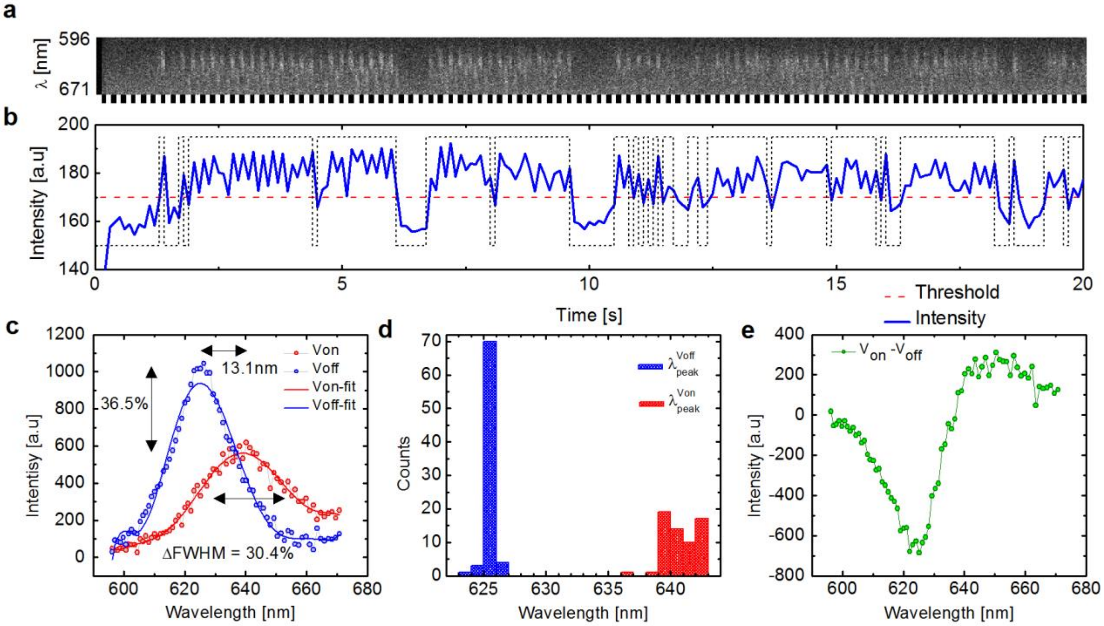

Fig. 2.4 Single NP's QCSE analysis of sample #8, presented in the same format as in Fig. 2.1

Similar QCSE measurements were performed for samples #5 - #8, all having type-II band alignment (Table 2.1). Fig. 2.4 shows representative results for a single NP from sample #8. A clear zigzag pattern of alternating V_{off} and V_{on} spectra is observed in the raw data of Fig. 2.4a (most notably around 6s and 9s). This zigzag pattern is also manifested in the integrated intensity trajectory during the blinking-on periods (Fig. 2.4b), a manifestation of the decreased intensity in the V_{on} state (Fig. 2.4c). Fig. 2.4c shows the averaged V_{on} frames (red) and averaged V_{off} frames (blue) for the whole trajectory, exhibiting an average $\Delta\lambda$=13.1 nm ($\Delta\lambda/\lambda$ = 2.1%) wavelength shift, 36.5% peak intensity (ΔI) reduction and 30.4% FWHM ($\Delta FWHM$) increase, which are respectively ×6.6, ×2.2 and ×2.3 larger than the corresponding changes presented in Fig. 2.1c for sample #2.

In contrast to Fig. 2.1d, the V_{off} and V_{on} spectral peak positions histograms (Fig. 2.4d) are well separated, suggesting the QCSE could be detected with high confidence in a single frame (0.1s) for a single NP, while 20s averaging was needed to extract the shift in Fig. 2.1. The large shift is also evident from the differential spectrum (Fig. 2.4e, as compared to the noisy differential spectrum of Fig. 2.4e).

Statistically meaningful data was also acquired for samples #5 - #8. While similar wavelength shifts were observed for samples #1 - #4 (Fig. 2.3), large variations were observed among type-II NPs (samples #5 - #8, Fig. 2.5). Sample #5 and #6 are spherical CdTe/CdSe (Core/Shell) type-II QDs with core diameters at around 4nm and shell thicknesses of around 1~2nm. They have smaller QCSE (average $\Delta\lambda$=0.5±1.2 nm and $\Delta\lambda$=0.4±1.3 nm for sample #5 and #6, respectively, and $\Delta\lambda$=3.1 nm maximum shifts for both, Fig. 2.5a and b) than type-I NRs. Sample #7 is a bullet-shape type-II ZnSe (sphere) seeded CdS NR, and it displays both red and blue spectral shifts due to its asymmetry. Wavelength blue shift in QCSE is a unique feature of asymmetric type-II quantum structures, and was previously measured only for 2D quantum well devices[49,50, 59]. Type-II band alignment assists in charge separation; the symmetry breaking of a single heterostructure implies that the electric field either pushes both the electron and the hole wavefunctions towards the interface, leading to a blue shift, or away from the interface (further enhancing charge separation) leading to a red shift. However, blue shifts do not occur in symmetric core-shell structures such as samples #5 and #6. Sample #7, in contrast, has an asymmetric type-II interface, allowing for charges to be pushed towards the interface or away from it, depending on the direction of the applied electric field.

The measured blue shifts as well as red shifts for sample #7 are favorably compared with red shifts reported for samples #1 - #6, with a Δλ=1.6±1.7 nm average shift and up to Δλ=8.2 nm for outliers (Fig. 2.5c). Even larger shifts (as large as Δλ=13.1 nm, Fig. 2.4) were observed for the type-II transition of sample #8 (this sample has ~730 nm type-I transition and ~630 nm type-II transition due to an asymmetric type-II interface), with an average shift of Δλ=3.5±3.1 nm (Fig. 2.5e). The type-I transition of sample #8 displayed an average shift of Δλ=1.2±2.0 nm and up to Δλ=6.5 nm for outliers (Fig. 2.5d).

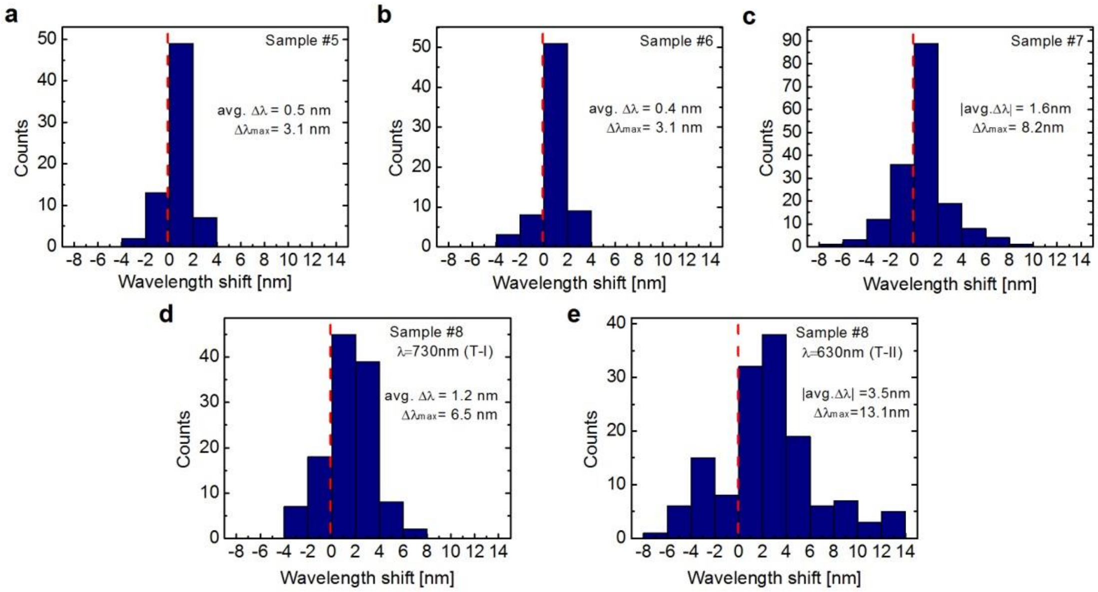

Fig. 2.5 Wavelength shift (Δλ) histograms for **(a),** Sample #5 **(b),** Sample #6 **(c),** Sample #7 **(d),** Sample #8, type-I transition **(e),** Sample #8, type-II transition.

2.4 Field dependent QCSE

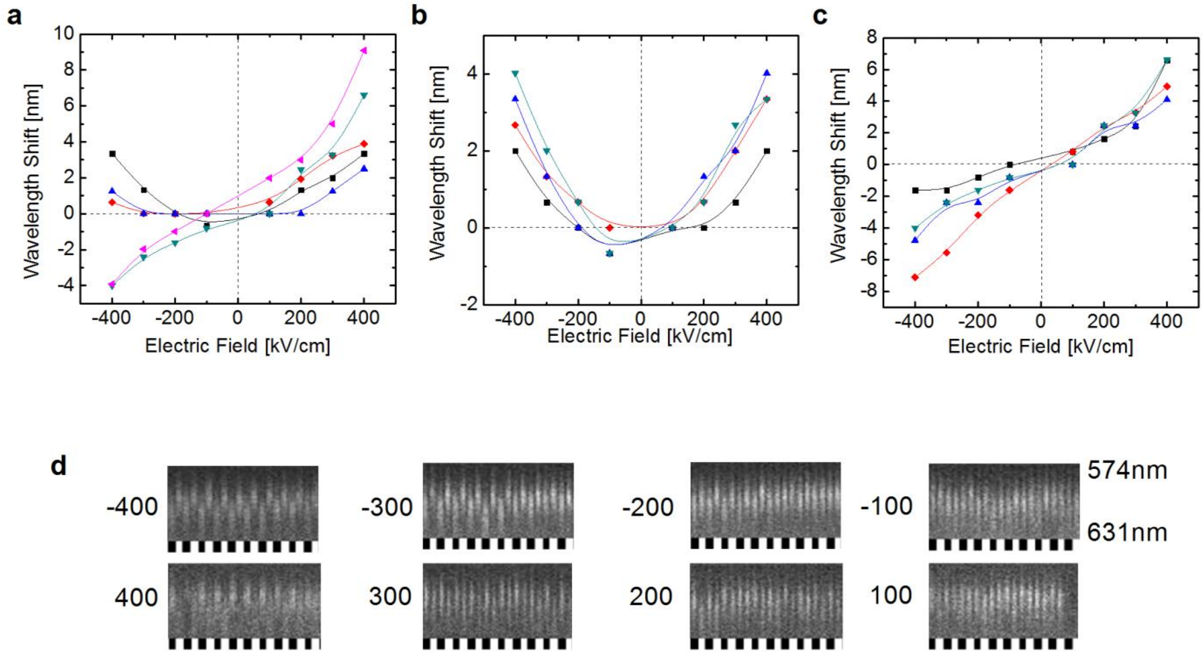

Fig. 2.6 Field dependent QCSE of single NP. **(a)**, Sample #2(black squares), #4(red diamonds), #6(blue triangles), #7(dark cyan down triangles), #8(pink left triangles); **(b)**, **(c)**, 4 individual NP of sample #2 **(b)** and sample #7 **(c)**; **(d)**, Spectral images for 20 frames of sample #7 (present in red diamonds in **c**). Applied electric field (kV/cm) is shown at the left of each images and λ is shown at the right side of the image of -100kV/cm field.

All QCSE data presented so far (Figs. 2.1-2.5) were measured at a fixed (maximal) V_{on} electric field (400 kV/cm). I also measured the field dependence of the QCSE (Δλ-F) for samples #2, #4, #6, #7 and #8 (samples #1, #3 and #5 displayed too small QCSE). The electric field was varied from -400 kV/cm to +400 kV/cm in 100 kV/cm increments. Fig. 2.6a displays Δλ-F plots for the different samples. For example, sample #2 showed a quadratic Δλ−F relationship as previously reported elsewhere[37, 45] while sample #4 showed an asymmetric Δλ-F as reported by Müller *et al.*[56] Due to its symmetrical core-shell type-II structure, sample #6 also displayed a quadratic relation (similar to the type-I sample #2). However, sample #7 and the type-II transition of sample #8 displayed roughly linear Δλ-F due to symmetry breaking (*i.e* the relative orientation of the applied field with respect to the type-II asymmetry of the structure). We note that the linear Δλ-F was observed for multiple quantum wells (MQWs) or superlattices,[59] but both red and blue shifts were simultaneously present in the spectrum (and therefore required spectral de-mixing for the analysis). Linear Δλ-F relation is well resolved here, manifesting the presence of a single asymmetric type-II interface (at very high fields this relation could be altered[50]). Fig. 2.6b, c displays Δλ-F curves for 4 different sample #2 NPs (middle) and 4 different sample #7 NPs (right). These curves represent the reproducibility of the QCSE among individual NPs from the same sample, and the robust and clear distinction in QCSE between type-I and asymmetric type-II structures. Fig. 2.6d shows 2s stretches (20 frames) of field-dependent spectral shifts raw data of a single NR from sample #7 (corresponding to red diamonds in Fig. 2.6c).

2.5 Simulations results

Geometries used for simulation are shown in Fig. S2.9. Parameters used in this study were obtained from the literature[60, 61, 62, 63] and are summarized in Table S2.1 and S2.2. For simplicity, the same dielectric constant ($\varepsilon_r = 9$) was applied for the all samples, and the dielectric constant of air ($\varepsilon_r = 1$) was assumed for the immediate surroundings of the NP. Conduction band (Δe) offset between CdS-CdZnSe is assumed to have 0.3eV which is a medium value of CdSe-

CdS and ZnSe-CdS. Valence band offsets (*Δ*h) of sample #8 are assumed to be zero except CdS-CdZnSe interface in order to ignore type-I transition and only take account type-II transition.

Experimental and calculated maximum Δλ, and E_b. Δλ blue shift are shown in parentheses.

	Exp. Δλ (nm)	Cal. Δλ (nm)	E_b (meV)
#2	4.0	3.1	40.0
#4	4.4	4.8	50.2
#6	3.1	1.5	21.9
#7	8.2 (-7.1)	12.4 (-7.6)	3.3
#8	13.1 (-7.3)	15.5 (-10.2)	0.035

Table 2.3 Experimental and calculated maximum Δλ (at 400 kV/cm) and E_b. Δλ blue shifts at (-400 kV/cm) are shown in parentheses.

The experimental results suggest a smaller extent of charge separation in type-I and quasi type-II NRs as compared to asymmetric type-II structures. In order to gain deeper insight and understanding for why this is so, I performed QCSE simulations for all samples shown in Fig. 2.6a. I solved the self-consistent Schrödinger-Poisson equations numerically (see Chapter 2.8). The simulations are in good agreement with previously published calculations[37, 56, 64, 65] and the experiments presented here. Dimensions and parameters used for these simulations are presented in Fig. S2.9. Table 2.3 compares the experimentally obtained maximum red (or blue) shifts with the corresponding simulated shifts and excitons' binding energies (E_b). Except for sample #6, simulations agree well with experiments. It is possible that our geometrical definition and parameters for sample #6, are not as good as for other samples. For example, CdTe/CdSe core/shell structures are easily branched into shapes such as tetrapod. It is possible that our samples exhibit initial small branching not detected by TEM (due to sample's aging or residual tetradecylphosphonic acid ligands that are not easily removed during TEM sample preparation). The overlap integral $\left\langle \psi_e^* | \psi_h \right\rangle^2$ is also extracted which is a measure of charge separation (Fig. 2.7a).

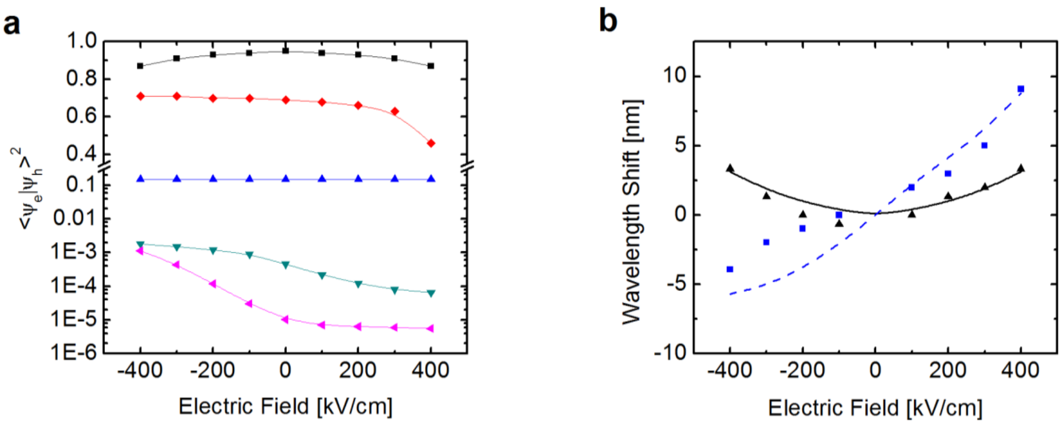

Fig. 2.7 Calculation results. **(a)**, Overlap integral of sample #2 (black squares), #4 (red diamonds), #6 (blue triangles), #7 (dark cyan down triangles), and #8 (pink left triangles). The y-axis has a log scale for $1\text{x}10^{-6}$ - 0.3 and a linear scale for 0.35 - 1.0; **(b)**, Field dependence ($\Delta\lambda$–F) of experiment (black triangles and blue squares) and simulation (solid and dashed line) of sample #2 (black) and #8 (blue), respectively.

The overlap integral has a maximal value at zero field for the type-I NP (sample #2) and for the symmetric core-shell type-II QD (sample #6). This is also reflected in the quadratic $\Delta\lambda$-F relation for these samples. However, the overlap reaches its maximal value at the negative maximal field (-400 kV/cm) for asymmetric heterostructures (type-II samples #7 and #8 and quasi type-II sample #4) in which both the electron and the hole are pushed towards each other and against the heterostructure interface (see corresponding band diagrams in Table 2.1). This is also reflected in the nearly linear Δλ-F relation for these samples. Similarly to the experimental results, simulations show that the charge separation in sample #2 turns out to be small (8% reduction in overlap integral) due to the strong exciton's binding energy (E_b=40.04 meV). Simulations for sample #4 show a sudden drop (17%) in the overlap integral at around 300 to 400 kV/cm, likely due to exciton ionization. The overlap integral for sample #6 does not exhibit a change as function of applied field due to the small size of the particle (charge separation is limited by the physical dimensions). Samples #7 and #8 exhibit minimal overlap since the exciton's binding energy is negligible (E_b=3.34 and 0.03 meV, respectively), and so is the Coulomb interaction for these samples. Fig. 2.7b compares field dependent Δλ values of calculation and experimental data of sample #2 and #8 (same data, as in Fig. 2.12a). Calculated Δλ of sample #2 regenerate the experiment data. For sample #8, it is assumed that there is partial alignment with an angle θ between the NR's long axis and the field direction, and a maximal possible shift of 13.1nm at θ=0. The data could then be reasonably fitted with a $\cos^2\theta$ ($\theta \approx 37^o$) correction factor (Fig. 2.7b).

2.6 Discussion

Most of previous single NP Stark effect measurements were performed at cryogenic temperatures[37, 56, 45]. The few RT[46,57] studies were done on the ensemble level with NPs embedded in polymer matrixes or in solvents with large dielectric constants ($\varepsilon_r > 1$). To the best of our knowledge, the work reported here is the first RT single NPs QCSE measurement on the air-glass interface. The difficulties that have hindered such measurements in the past include: (i) relatively small wavelength shifts; (ii) short exciton lifetime (rapid ionization) at RT; (iii) spectral broadening due to surface charge fluctuations; (iv) requirement for large applied fields (> 100 kV/cm, close to material breakdown); (v) dielectric mismatch between the semiconductor NP (large ε_r) and air (ε_r=1). Due to this mismatch, most of the applied field is dropped near the electrodes and not across the particle. Nonetheless, I was able to measure QCSE of single NPs at RT for eight different samples of different compositions and geometries. Using modulation spectroscopy and averaging, I could measure the effect even for NPs with relatively small polarizability (such as sample #1 through #6). Moreover, taking geometry and material composition into account, I could qualitatively and quantitatively reproduce experimental results in simulations, including the NPs field dependence ($\Delta\lambda$-F).

I find (both experimentally and in simulations) that the strong Coulomb interaction in type-I NPs (samples #1 and #2) results in a small QCSE ($\Delta\lambda < 4$ nm). This is the manifestation of a minute field-induced band bending that does alter much the electron’s and hole’s potential energy minima (and therefore only slightly reduces the Coulomb attraction energy). The insensitivity of the effect to length (Fig. 2.3) is also an indication for small perturbation to the Coulomb interaction in these particles. Since NPs from samples #1 and #2 display a quadratic $\Delta\lambda$-F relation, it is possible to use the well-known energy (E)- field (F) expression $\Delta E=\alpha F^2$ to evaluate α, the polarizability of these NPs. Sample #1 has $\alpha=1.82\times10^5$ Å^3 and sample #2 has $\alpha=2.20\times10^5$ Å^3. It is noted that a similar polarizability value (2.38×10^5 Å^3) was found for a 5.8 nm diameter QD in ref. [37] (even though that QD sample had a different geometry).

Asymmetric quasi type-II NRs (samples #3 and #4) display only very slightly larger QCSE (average $\Delta\lambda \approx 0.7$ nm) as compared to type-I NPs (average $\Delta\lambda \approx 0.6$ nm). Since the position (and symmetry) of the QD seed in the seeded rod structure is not well controlled or defined, their $\Delta\lambda$-F relation is somewhere in between linear and quadratic[56]. They also exhibit only a weak length and orientation dependence (Fig. 2.3). Nonetheless, a few individual NRs from these samples, most likely well aligned with the direction of the applied field, exhibited clear zigzag pattern in the integrated intensity and peak wavelength signals (Fig. 2.2). Simulations show that these samples have a reduced overlap integral overall (as compared to samples #1 and #2), and an additional sudden drop around 300 to 400 kV/cm, suggesting a weaker Coulomb interaction and exciton ionization at these large fields ($\Delta\lambda$, however, is smaller as compared to the value measured for similar particles at cryogenic temperatures[56]).

Symmetric type-II QDs (samples #5 and #6) exhibit the smallest averaged QCSE ($\Delta\lambda$=0.5, 0.4 nm respectively). Simulations predict even a smaller shift (Table 2.3). Due to their small size and symmetric shape, charge separation is very limited for these particles, as evidenced by Fig. 2.7a: they have a larger overlap integral with respect to the larger rod-shaped samples #7 and #8 (due to their smaller size), but smaller overlap integral with respect to samples #1 and #2 since they are type-II. As expected, these spherically-symmetric samples have a quadratic $\Delta\lambda$-F relation, exhibiting only red shifts.

Asymmetric type-II NRs (samples #7 and #8) exhibit the largest spectral shifts. Charge separation is enhanced in these structures since the minimum energy for the electron is on one side of the interface, while the minimum energy for the hole is on the other side of the interface, leading to a reduced Coulomb attraction between the separated charge carriers. This, in turn, leads to a larger response to an external field. The breaking of symmetry at the interface leads to a blue shift when the field is aligned in a direction that 'pushes' the electron's and hole's wavefunctions towards the interface (and towards each other), and a red shift when the field is in the opposite direction, *i.e.* 'pulls apart' the electron's and hole's wavefunctions away from the interface (Fig. 2.6). The largest observed red shifts are $\Delta\lambda$=8.2 nm and $\Delta\lambda$=13.1 nm for samples #7 and #8 respectively, values which are almost ×2 and ×3 larger than the values for samples #1 through #6. The largest observed blue shifts were also sizeable ($\Delta\lambda$=7.1 nm and $\Delta\lambda$=7.3 nm for samples #7 and #8 respectively). As expected, these samples exhibit nearly linear $\Delta\lambda$-F dependence. Interestingly, simulations confirm the experimental observation that the slope in the first quadrant (red shift) is different from the slope in the third quadrant (blue shift). The difference in slopes is attributed to the two field configurations described below.

In the case where the field 'pulls apart' the electron and the hole away from each other, longer rods will afford a larger charge separation, a larger dipole ($\mu=q\times d$, μ : dipole moment, q : electron charge, d : distance between e and h), a reduced Coulomb attraction, and therefore a larger $\Delta\lambda$ red shift. The red shifts obtained for samples #7 and #8 are much larger than the shifts measured for samples #1 and #2, signifying the importance of the type-II interface. However, symmetric core/shell type-II structures (sample #5 and #6) lack the geometry that affords the generation of a large dipole. In short, the largest red shifts are achieved for elongated, asymmetric, type-II heterostructures.

In the case where the field 'pushes' the electron and the hole towards the interface (and towards each other), the geometry of the rod plays a less important role. Instead, the band tilting due to the external applied field and the redistribution of charges, form triangle potential wells for both the electron and the hole. The blue shift is a measure for the degree of tilting due to the established internal electric field (which is proportional to the external field). In the above discussion rods is treated as 1D wires; geometry could have a secondary effect on the blue shift when the true 3D structure of the NR is taken into account. It is noted that the blue shift configuration is advantageous for cases where the size of the sensor matters, but that the red shift configuration affords the highest voltage sensitivity.

Three distinct classes of Δλ-F relations were observed: (1) Symmetric NPs with strong Coulomb attraction (type-I) display a red shift with a quadratic Δλ-F (and ΔE-F) dependence: $\Delta E=\alpha F^2$ [37] which is characterized by the polarizability α; (2) Asymmetric NRs with reduced Coulomb attraction (type-II) display a red shift with a linear at zero electric field towards positive fields Δλ-F (and ΔE-F) dependence: $\Delta E=F\times d$ (d: distance);[46] (3) Asymmetric NRs with reduced Coulomb attraction (type-II) display a blue shift with nearly linear for negative fields Δλ-F (and ΔE-F) dependence: $\Delta E=\left(\frac{9hq}{16\sqrt{2m^*}}\right)^{2/3}\times F^{2/3}$, $\frac{1}{m^*}=\frac{1}{m_e^*}+\frac{1}{m_h^*}$ [66] where h is Plank's constant, q is electron charge and m_e* and m_h* are effective masses of the electron and hole respectively.

A sudden transition from a quadratic to a linear Δλ-F dependence could occur at large enough fields, manifesting the ionization of the exciton that leads to a decrease in the overlap integral and an increase in the red shift. Such critical behavior was observed for sample #4 at around ~300-400 kV/cm. Samples #7 and #8, however, display such ionization already at a zero filed due to their type-II nature. Exciton ionization could not be observed for type-I NRs (samples #1 and #2).

When these NPs are used for field-sensing application, spectral diffusion should be taken into account. Charge trapping at the NP surface directly affects the magnitude of QCSE by changing the electric field inside the NP. If charge trapping is dynamic, it induces spectral diffusion.[67] The resulting spread of wavelengths due to such diffusion is not larger than 10nm.[48,68] In our observation, emission peaks diffuse no more than 4nm (Fig. 2.7d, 2.8d, 2.10d), consistent with the earlier works. Interestingly, our results suggest that trapped charges have a strong influence on V_{on} states (Fig. 2.1d, 2.2d, 2.4d, red) as compared to V_{off} states. This is likely because the wavefunction is more susceptible to the trapped charges when it is close to the surface of the NP. Obviously, spectral diffusion due to trapped charges reduces the signal to noise ratio (S/N) in voltage sensing, especially for short integration times. Generally, it is observed that if the average shift is larger than 4 nm, reliable voltage sensing could be achieved despite spectral diffusion.

In summary, the observations indicate that the QCSE magnitude, and applied field dependence are sensitive to the shape and the material composition of the nanoparticles: (i) Type-I NRs (homostructures with cylindrical symmetry) only weakly respond to the applied field (Fig. 2.1). The magnitude of their QCSE shift is small and the signal is usually masked by spectral diffusion at RT (likely due to local charge fluctuations/redistributions). With signal averaging some weak signals could be measured above the noise. As reported earlier[45], these NRs display a quadratic field dependence (Fig. 2.6a, black squares). Although one might expect charge separation to be dependent on the NR length, no length-dependency for Type-I NRs was observed; (ii) Quasi type-II NRs (heterostructures with cylindrical symmetry) display slightly larger QCSE than Type-I NRs (Fig. 2.2). Also, its asymmetric composition alters its field dependence, to be no longer quadratic (Fig. 2.6a, red diamonds). Calculations indeed confirm reduced Coulomb interaction for Quasi type-II NRs as compared to Type-I NRs (Fig. 2.7a, red diamonds *vs*. black squares), allowing for larger polarizability; (iii) Type-II core/shell QDs (heterostructures with spherical symmetry) display the weakest QCSE, often totally masked by spectral diffusion (Fig. 2.5a, b). This observation implies that symmetry breaking is important for sizeable QCSE. The field dependence of these particles is quadratic (Fig. 2.6a, blue triangles); (iv) Type-II NRs (heterostructures with cylindrical symmetry) display the largest QCSE (Fig. 2.4) and close to linear field dependence (Fig. 2.6a, dark cyan down and pink left triangles). Calculations suggest that Coulomb interaction is reduced the most in these structures (Fig. 2.7a, dark cyan down and pink left triangles), affording large polarizability. The symmetry breaking by the type-II heterostructure is manifested through the close to linear field dependence. The large shifts in these samples are hardly affected by spectral diffusion.

2.7 Summary

I measured and simulated wavelength shifts for eight different NPs formulations on the single molecule level at room temperature. It is found that type-II asymmetric NRs ZnSe-CdS and CdSe(Te)-CdS-CdZnSe yielded the largest shifts, demonstrating single particle sensitivity of

$\Delta\lambda/\lambda \sim 2.1\%$ at a field of 400 kV/cm. The shifts for these samples (#7 and #8) were roughly linear with the applied external field and displayed both red and blue shifts within a broad range of applied voltages, depending on the field's polarity with respect to the particle's orientation. The demonstrated sensitivity could be translated into a noise-immune, ratiometric voltage measurement of two spectral bands (by splitting the fluorescence with an appropriate dichroic mirror followed up by band-pass filtering the two spectral bands using two detectors).

The temporal response of the Stark effect is in the nanoseconds range. If voltage measurements are to be performed with NPs on the ensemble level, very fast signals could indeed be detected. The voltage nanosensors presented here however, are capable of reporting voltage signals on the single particle level. For this, though, enough photons need to be detected from a single nanosensor to yield a reasonable signal-to-noise-ratio. I demonstrated here discernible shifts measured on single nanosensors with 30~100ms time resolution. With further optimization, stronger laser excitation, faster cameras, brighter QDs, and better QDs' coating, significant improvements in single nanosensor time resolution will be expected.

I believe that the results reported here could be further enhanced by: (i) improving synthesis to yield even more uniform particles; (ii) engineering electron and hole wavefunctions that display weaker exciton binding energy while maintaining high radiative recombination rate (by improving on bandgap structure, composition, and geometry); (iii) reducing electrode spacing such that most of the field drops on the NPs; (iv) matching the environment's dielectric constant to that of the particles or identification of asymmetric type-II structure with lower dielectric constant. With such improvements, these voltage nanosensors could possibly find interesting applications.

2.8 Material and Methods

SI-2.1 Colloidal syntheses

Samples #1 and #2 are homogeneous CdSe NRs that were prepared according to a published protocol[69] with some modifications. With the same precursors ratio, sample #1 (short NR) and sample #2 (long NR) were differently shaped by adjusting growth temperature. Sample #1 was grown at 300°C for 10 mins; Sample #2 (long and thin NR) was grown at 270°C for 10 min. Samples #3 (short NR) and #4 (long NR) are quasi type-II seeded NRs. CdSe cores and seeded CdS NRs were prepared according to published protocols ref. [23]and [70] respectively with some modifications. Their lengths were predominantly controlled by the amount of CdSe dots used for seeded growth. Samples #5 and #6 are CdTe/CdSe core/shell structured type-II QDs that were prepared by successive ion layer adsorption and reaction (SILAR) according to a published protocol[71] with some modifications. Samples #7 and #8 are type-II seeded NRs. Sample 7 has bullet-shape morphology with one ZnSe QD seed buried in CdS matrix. It was prepared according to a published protocol[46]. Sample #8 is an elongated NR having core-shell-shell structure, Te-doped CdSe core seeded in CdS (inner shell) - CdZnSe alloy (outmost shell). The detailed morphology, band structure and synthesis of sample #8 is described in ref. [47].

Chemicals and materials: Cadmium oxide (CdO, 99.99%), Zinc Oxide (ZnO, 99.99%) oleic acid (90%), tri-n-octylphosphine (TOP, 90%), trioctylphosphine oxide (TOPO, 99% and technical grade 90%) hexadecylamine (HDA), octadecylamine (ODA, 97%), octylamine (97%), octadecene (ODE, 90%), tetra-butylphosphene (TBP, 97%), selenium (Se, 99.999%), telluride (Te, 99%), Sulfur (S, 99.5%) and oleylamine (OA, 70%) along with all organic solvents were purchased from Sigma-Aldrich and used without any further purification. Tetradecylphosphonic acid (TDPA), hexylphosphonic acid (HPA) and octadecylphosphonic (ODPA) were purchased from PCI Synthesis.

CdSe NRs: A three-neck flask was loaded with a mixture of 1 mmol CdO, 0.6 mmol HPA, 1.4 mmol TDPA and 2.0 g TOPO (99%). Temperature was raised slowly to 250°C under nitrogen flow to obtain clear (or slightly opaque) colorless solution. The cooled mixture was left overnight in ambient. In continuation, the mixture was reheated to 320°C under nitrogen flow. A colorless Se solution was quickly injected into this colorless solution containing 0.5 mmol Se, 0.6 mmol TBP, 2.7 mmol TOP and 0.3 g toluene. Sample #1: The growth temperature was set at 300°C. Due to the injection, the temperature decreased to 270°C but climbed back to 300°C within 10 mins. Growth was terminated after 10mins by rapid cooling to RT. The resulted NRs had a small aspect ratio. Sample #2: The same protocol as for sample #1 was followed, with two exceptions: instead of TOPO (99%), a technical grade TOPO (90%) was used, and the growth step was proceeded for 10mins at 270°C.

Quasi-Type-II NRs (CdSe seeded in CdS): CdSe core nanocrystals were prepared using a procedure modified from a previous report[23]. A 50 ml round bottom flask was loaded with 60 mg (0.5 mmol) CdO, 280 mg ODPA and 3 g TOPO. After degassing under vacuum for 1 hour at 120°C the temperature was raised to 340°C under argon until dissolution of CdO at which point 1.8 ml TOP was injected and temperature was raised to 370°C. A solution containing 58 mg Se in 0.5 ml TOP was swiftly injected and heating mantle was removed until. Final core size had a diameter of about 2.7 nm. A slight modification of previously reported methods[55] was used for seeded growth of CdS. A 50 ml round bottom flask was charged with 211 mg (1.6 mmol) CdO, 1 g ODPA, 50 mg HPA and 3.46 g TOPO. The reaction flask was degassed for 3 hours at 130° and then temperature was raised to 340°C under argon until dissolution of CdO at which point 1.8 ml TOP was injected. CdSe seed solution was separated and purified for reaction by mixing with toluene and precipitating with excess methanol 3 times. Seeds were then re-dissolving in 0.6 ml TOP. The S:TOP precursor solution was prepared by mixing 51mg S (1.6mmol) in 0.6 ml TOP. Temperature was raised to 350°C for injection. The amount of dots used for preparation of sample #3 was 8 x10-7 and for sample #4 was 1 x10-7moles.

Type-II QDs: CdTe/CdSe: CdTe core QDs were synthesized in high temperature organic solution. The mixture of 0.5 mmol CdO, 1.25 mmol TDPA and 20 g ODE was sonicated for 5 min before heated on the mantle to 290°C under nitrogen purging. A clear and colorless solution was obtained. Meanwhile a mixture of 0.5 mmol Te powder, 0.31 g TBP and 6 g ODE in septum-topped vial was sonicated for 5 min and then heated on a mantle to 214°C in order to dissolve the Te. This Te precursor solution, upon cooling to room temperature, was loaded into a 10 ml syringe mounted with a 12 gauge needle. Cd precursor solution was heated to 310°C under nitrogen; the Te precursor was injected into it under stirring. The temperature dropped to 270°C. At this temperature the reaction was proceeding for about 30 min (or whenever the target absorption peak position was reached). CdTe QDs were purified and characterized by UV-Vis (to estimate the concentration using known extinction coefficients) and TEM (to measure particle size and calculate surface area) for the following steps. Sample #5: CdTe core 4.2 nm, CdSe shell 2-monolayer, emission 670 nm. 1.2 g CdTe hexane solution (concentration was calculated in units of mmol/gram) was mixed with 0.5 g oleic acid and 3.5 g ODE in a flask. After the removal of hexane and degassing under vacuum, the flask was heated to 210°C under nitrogen. 0.04 M Cd precursor was prepared by heating to 250°C and dissolving 76.8 mg CdO in 1.35 g oleic acid and 10.65 g ODE. The colorless solution was pumped while being cooled to room temperature. Similarly 0.04 M Se precursor was made with 38 mg Se, 1.624 g TBP and 7.89 g ODE. The Cd and Se precursors were loaded into separate syringes for manual dripping or syringe pump infusion. At 210°C the first 0.104 ml Se solution was slowly dripped into the CdTe containing flask. 10 min later the same amount of Cd solution was added to complete the first monolayer of CdSe shell. For the growth of the second layer CdSe, 0.139 ml Se and Cd solutions were introduced sequentially and respectively. Successively with 0.177 ml for the third layer, 0.221 ml for the fourth and 0.270 ml for the fifth layer, the 3.9 nm CdTe QD was overcoated with 5 monolayers of CdSe, showing a single emission at 710 nm. Sample #6: CdTe core 3.9 nm, CdSe shell 5-monolayer, emission 710; nm. The epitaxial growth of CdSe shell onto the CdTe core was executed via the SILAR method[71]. Cd and Se precursor solutions were introduced into the reaction flask containing CdTe core, fresh ligands (e.g., oleic acid) and solvent (ODE or TOPO) alternatively, with increasing amounts for each additional layer. The amounts were calculated to cover all QDs in solution to exact one monolayer.

Type-II NRs: ZnSe/CdS (Sample #7): 3.7 nm ZnSe QD was prepared via multiple injections. The particles were purified by precipitations and quantified for concentration with UV-Vis[24]. 40 nmol ZnSe were redispersed in 0.7 g TOP immediately following the removal hexane by vacuum. 120 mg S were dissolved in 0.8 g hot TOP before being combined at room temperature with ZnSe/TOP for injection. Cd precursor solution was prepared by degassing the mixture of 60 mg CdO, 290 mg ODPA, 80 mg HPA and 3.0 g TOPO (Tech.) at 150°C under vacuum before the reaction with sulfur precursor in the presence of the seed (template) at 365°C. Upon the quick injection, the temperature dipped to 320°C. Without change of the setting, the temperature went back up to 365°C. The growth was stopped at 10 min after injection.

Te doped CdSe core in CdS-CdZnS-CdZnSe shell (Sample #8): Te doped CdSe core nanocrystals were prepared using a procedure modified from a previous report[72]. A 50 ml round bottom flask was loaded with 26 mg (0.2 mmol) CdO, 127 mg TDPA and 3.6 g TOPO. After degassing under vacuum for 2 hours at 130°C the temperature was raised to 340°C under argon until CdO dissolved and solution became clear. A Se/Te precursor solution in TOP was prepared by dissolving 40 mg (0.5 mmol) Se in 0.6 ml TOP and mixing in 100 µl of a 0.1 M Te:TOP solution (Te constitutes 4% of the Cd). Reaction solution was heated to 360°C for injection of the Se/Te precursor. The heating mantle was removed immediately after injection. The solution color changed within 10 seconds to a deep dark red shade.

Seeded growth of CdS: A slight modification of previously reported methods[70] was used. A 50 ml round bottom flask was loaded with 100 mg (0.75 mmol) CdO, 600 mg ODPA, 80 mg HPA and 3.6 g TOPO. The reaction flask was degassed for 3 hours at 130°C and then temperature was raised to 330-350°C to dissolve CdO at which point 1.8 ml TOP was added. The CdSe(Te) quantum dots (QDs) were separated and purified for reaction by mixing 1 ml of the QD solution with toluene until completely clear and precipitating with excess acetone. Further purification entailed re-dissolving in 1 ml chloroform/octylamine (6:1) and precipitating with acetone, then re-dissolving in 0.5 ml chloroform/oleic acid/TOP (1:1:8). The QD solution containing ~9 x10-8moles of core QDs, was then mixed with an S:TOP solution containing 115 mg S in 1.5 ml TOP. The QD/S solution was quickly injected into the flask at 350°C. A portion of the reaction solution was extracted within 20 seconds for quenching in room temperature ODE.

Continued shell growth of CdZnS: A 50 ml round bottom flask was charged with 1.78 g ODA, 1 ml HDA and 4ml ODE and degassed under vacuum for 4 hours. The CdSe(Te)/CdS NCs QDs were separated for reaction by mixing 2 ml mother solution with chloroform until completely clear and precipitating with excess acetone/ methanol (1:1) after which they were re-dissolved in 1 ml toluene/TOP (1:1). Preparation of S, Cd and Zn precursor solutions is described below (stock solutions section). Cd and Zn oleate solutions were mixed in a 1:2.5 ratio in order to get partial incorporation of Zn in the CdS lattice. Total volumes of 2.6 ml Cd/Zn precursor and 2.6 ml S precursor were added drop-wise to reaction solution over the course of 11 hours. The additions were carried out in a staggered fashion at temperatures ranging from 190° to 220° C.

Continued growth of CdZnSe: Growth of CdZnSe was carried out at 200-220°C by the drop wise addition of Se:TOP stock solution over the course of about 1 hour. Within 10 min, a new narrow peak in the emission spectrum appeared at 580 nm, indicating that the solution contained large amounts of unreacted Cd and Zn precursors. As growth of ZnSe continued, the two peaks remained completely distinguishable as both peaks red-shifted in tandem. It was also apparent that the VIS emission was getting stronger on the expense of the NIR emission.

Stock solutions for sample #8: Stock solutions of Cd, S, Se, Te and Zn with a concentration of 0.1M for shell growth were prepared in advance; for preparation of Cd (or Zn) oleate 0.1 M - CdO (or ZnO) and oleic acid (ratio of 1:8) were placed in 35 ml ODE in a 100 ml round bottom flask. The solution was degassed for 20 min at 120°C then heated to 300°C on a Schlenck line until full dissolution of the CdO, evident by the solution turning colorless. For S:ODE 0.1 M, 160mg elemental sulfur (5 mmol) and 50ml ODE were placed in a 100 ml round bottom flask. The solution was degassed for 20 min at 120°C and then heated to 200°C for 1 hour, by which time all the sulfur dissolved and the solution attained a yellowish tint. Te:TOP and Se:TOP solutions were prepared by sonicating under heat the desired amount of the elemental material in TOP until it dissolved. For shell growth I applied the technique of successive ion layer deposition and adsorption (SILAR) as described previously[73].

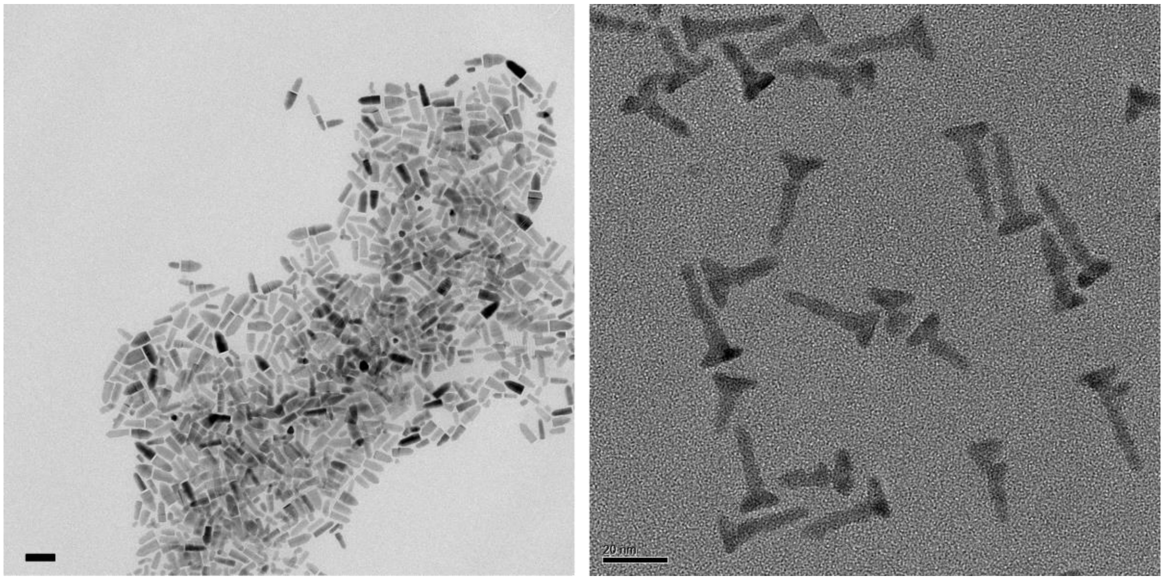

Fig. S2.1 TEM micrographs **(a)** Sample #7 (Scale bar is 50nm.) (**b)** Sample #8 (Scale bar is 20nm.)

SI-2.2 Optical Setup

Fig. S2.2 describes the set-up used to acquire QCSE spectroscopic data on single QDs and NRs. The set-up is based on an Olympus IX71 inverted microscope equipped with a Xenon lamp (Olympus, U-LH75XEAPO, 75W) and excitation filter (BP 470/40, Chorma Technology Corp, Bellows Falls, VT). The emission of the NPs is collected by ×60 objective lens (Olympus, PlanApo 60×, n=1.45, oil immersion), passed through a dichroic mirror (DM, 505DCXRU, Chorma Technology Corp, Bellows Falls, VT) and then directed to the high resolution spectral detection arm. Spectral features (Figure S2.6a) are selected by a variable slit (in order to remove overlapping spectra of neighboring NPs; Figure S2.6).

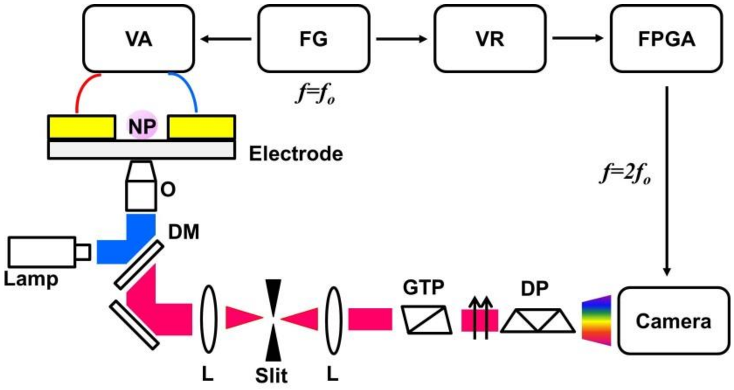

Fig. S2.2 Schematics of the set up used to perform single nanoparticle QCSE spectroscopy. (L=lens, GTP=Glan-Thompson prism, DP=dove prism, DM=dicroic mirror, FG=function generator, NP=nanoparticle, O=objective lens, FPGA=field-programmable gate array, VR=voltage regulator, VA=voltage amplifier)

A Glan-Thompson prism (GTP, Thorlabs, Newton, NJ, acting as a linear polarizer downstream from the slit) selects NRs that are aligned along the direction of the applied electric field. Larger QCSE wavelength shifts are expected for charge separation along the long axis of the NR, which is also the direction of its polarized emission[74]. The emission is then dispersed by a dove prism (DP, Thorlabs, Newton, NJ) and detected by an Andor iXon electron multiply (EM) charge coupled device (CCD) camera (EMCCD, Andor iXon, South Windsor, CT) (see also Figure S6c). The horizontal axis of the resulted spectral images was calibrated with 532 nm (DPGL-20P, World Star Tech, Toronto, Canada), 594 nm (25 LYP 173, Melles Griot, Albuquerque, NM) lasers and 810 nm LED (NT59-432, Edmund optics, Barrington, NJ) lines using a quadratic fit.

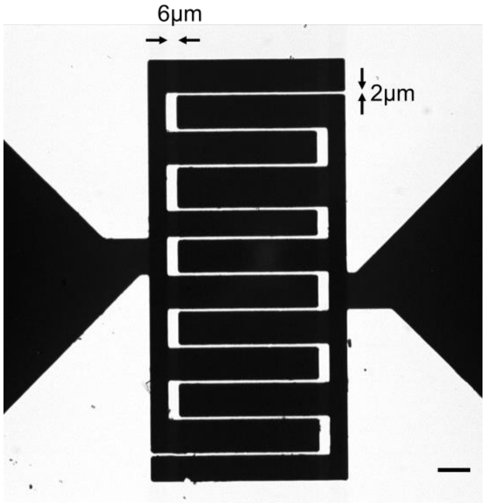

Fig. S2.3 Interdigitated electrode. (bright field image). Electrode spacing is 2μm. Scale bar is 10μm.

Photolithographically patterned interdigitated electrodes (Figure S2.3) were fabricated at the UCLA Nanoelectronics Research Facility using a home-made designed mask and conventional lithographic and acetone-based lift-off procedures. 100 nm/5 nm Au/Cr layers were deposited onto 25 mm diameter cover glass slides (Circle #1, 0.13 to 0.17mm thickness) using a CHA Mark 40 e-beam evaporator. The gap between finger electrodes is 2um.

SI-2.3 AC dielectrophoresis NR alignment

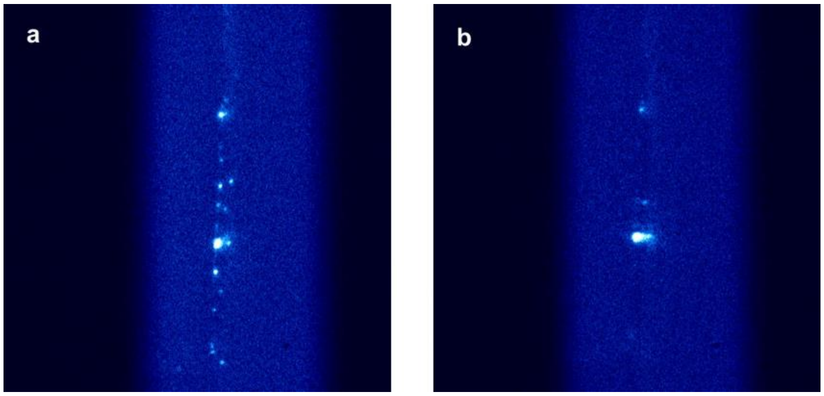

Fig. S2.4 Emission of aligned sample #4 after AC dielectrophoresis. Emission is passed through Glan-Thompson prism (GTP). **(a)**, GTP is installed so that NRs' emission polarization is analyzed parallel to the electric field. **(b)** GTP is installed so that NR's emission polarization is analyzed perpendicular to the electric field.

NPs samples were dissolved in toluene solution (1mg/ml), diluted ×10, ×100, ×1000 and ×10000 times and casted onto an interdigitated electrode-patterned cover glass (Figure S2.4). Sample casting started with the lowest concentration and step-wise increased with higher concentrations to reach optimal surface density for subsequent single molecule spectroscopy (in order to avoid signal overlap on the camera). A dielectrophoresis method was used for each casted layer in an attempt to align NRs long-axis along the field direction[75] (except for control experiments) in order to maximize the QCSE signal. It was achieved by applying an AC electric field (10 kHz, 100 kV/cm) during the casting process (before toluene evaporation[75]).

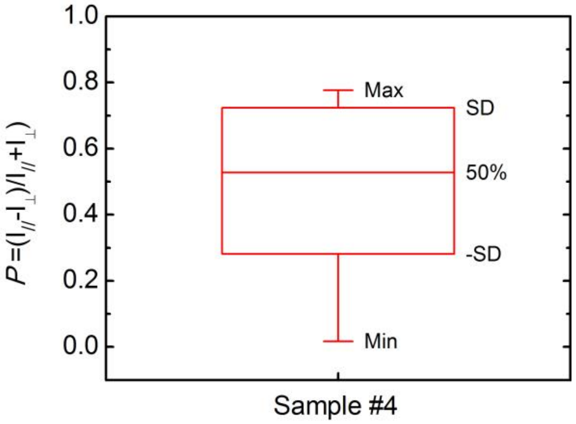

Fig. S2.5 Box chart of 15 NRs' (sample #4) fluorescence polarization. SD is one standard deviation**.**

Figure S2.4 shows the effect of AC dielectrophoresis on NRs alignment. Since NRs exhibit linear polarization along their long axis[74], their degree of alignment could be assessed by analyzing their polarized emission parallel and perpendicular to the direction of the aligning AC field. The figure shows a field of view containing several NPs of sample #4 after the alignment protocol has been implemented. More bright spots can be seen when the GTP polarization analyzer is aligned parallel to the field (a). Fewer (and weaker) spots are seen when the GTP polarization analyzer is aligned perpendicular to the field (b). By measuring the parallel $I_{\parallel}$ and perpendicular $I_{\perp}$ polarization components of individual NRs' emission, one can calculate the polarization *P* according to: $P=(I_{\parallel}-I_{\perp})/(I_{\parallel}+I_{\perp})$ for each NR. Figure S2.5 shows a box chart of P values for 15 individual NRs. The mean *P* is 0.50, suggesting a reasonable alignment yield (random orientation would have resulted in an average $\bar{P}=0$), a slightly lower value than the one reported for CdSe NR in ref. [74].

SI-2.4 Data Analysis

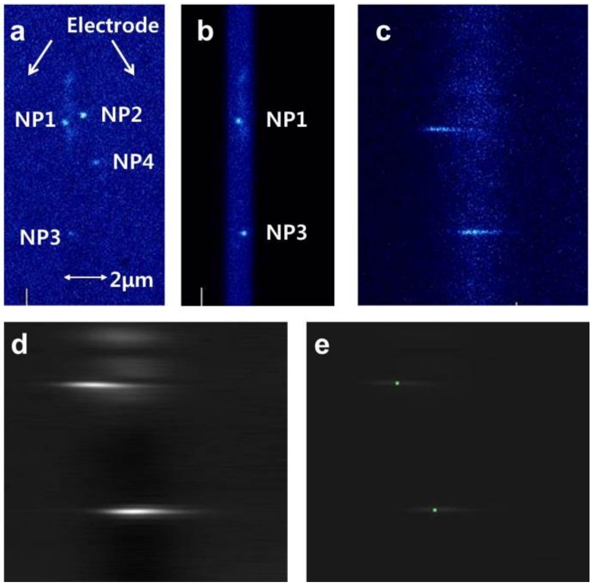

Fig. S2.6 The procedure used to acquire spectral images. **(a)**, NPs image (single frame) taken without the slit and the prism; **(b)**, the same image taken with the slit; **(c)**, same image as in **(b)** after dispersion by the prism; **(d)**, Average of 200 frames of the image in **(c)** after background correction; €, automated spectral peak detection (overlaid with **(d)**). Green dots represent spectral peak positions of NP1 and NP3.

Figure S2.6 illustrates the procedure that was utilized to find NPs, select isolated NPs, and acquire their spectra. For example, four NPs located in the gap between two electrodes' fingers were observed in the data set shown in Figure S2.6a (NP1-NP4). Since the dispersed emission of NP2 overlapped with that of NP1, the variable slit was adjusted to filter-out signals from NP2 and NP4, i.e. only the signals from NP1 and NP3 were selected for further analysis (Figure S2.6b). After passing through the dispersive prism, the two spectra of NP1 and NP3 were recorded on the EMCCD (Figure S2.6c). The camera acquisition clock (frame-rate) was synchronized to the alternation frequency of the (quasi) DC electric field (square wave, typically f_o=5 Hz) that was applied to the interdigitated electrodes using a function generator (FG2A, Beckman industrial, Fullerton, CA) followed by a voltage regulator and a high voltage amplifier (STM 100 controller, RHK technology, Troy, MI). The amplitude of the applied field to the electrodes could reach up to ±500 kV/cm (f=5 Hz). The function generator synchronization signal was frequency doubled by a Labview-controlled FPGA board ($f= 2f_o= 10$ Hz) (Spartan 3E, Xilink, San Jose, CA) resulting in successive synchronized acquisitions of camera frames in the Von and Voff periods of the square wave (the delays between the generated waveform by the function generator, the high-voltage amplifier, and the actual applied voltage on the electrodes, were confirmed to be negligible; the RC time constant of the electrode was measured to be 0.2 ps). Typical data set was acquired for 20~30 seconds in a format of a movie of ~200-300 alternating frames, i.e. 100~150 frames for each Von and Voff.

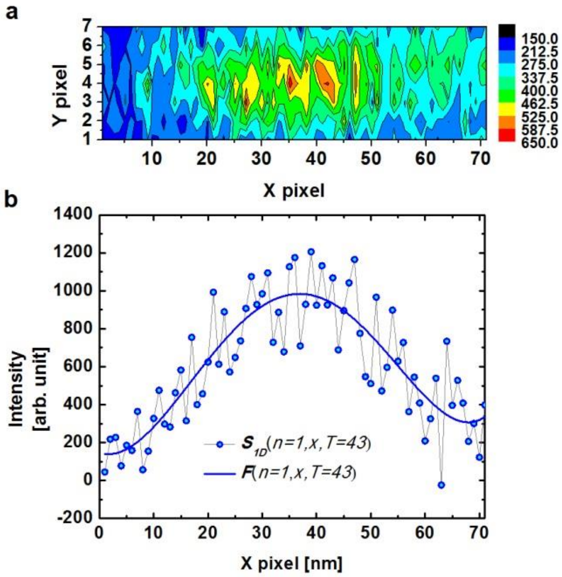

Fig. S2.7 Intensity profile of the 43th frame in a movie of NP1 in Fig. S2.6. **(a)**, 2 dimensional intensity profile S_{2D}(n=1,x, y, t=43). Color map illustrates photon number acquired at each pixel. **(b)**, 1D intensity profile S_{1D}(n=1,x,t=43) and its fitting curve (F)

All data sets were automatically analyzed using a home-written Matlab program. The program detects NPs location in the field-of-view (on the sum of all movie frames, Figure S2.6e) and extracts, for each frame in a movie, all relevant parameters from individual spectrum including the peak emission wavelength (λ_{peak}), the integrated intensity, and the full width half maximum (FWHM). It then calculates the histograms of these properties for all Von and Voff frames in a movie. To achieve this, the following steps were performed:

(i) Background correction: Owing to the nonlinear prism's dispersion (especially at $\lambda >$ 700nm) and random background noise, background was corrected across the whole field (Figure S6d). The X-axis (column) of the raw spectral image represents wavelength. The Y-axis (row) of the raw spectral image represents real space. All pixels in the field-of-view were integrated over all frames (along t) to average out temporal intensity fluctuations, and over all rows (Y-axis) to achieve an averaged, ‘single row’ background. This vector is then subtracted from each frame and each row to achieve background correction.

(ii) Peak detection: The spectrum of a single NP spreads over several rows and columns. To detect each spectrum’s peak position, a Matlab built-in one-dimensional peak detection function, ‘findpeaks’, was implemented twice, both for X and for Y directions. It returns the peak coordinates (x_n, y_n , where n indexes individual NPs). When the areal concentration of NPs was adjusted properly (~1 NP per 10 μm^2), the yield of spectra extraction from individual NPs approached 95%.

(iii) Spectrum’s profile and thresholding: The program returned a list of NPs coordinates (x_n, y_n), (Figure S2.6e) and subsequently extracted parameters for all NPS in the list, one NP at a time. For each individual NP’s spectrum of each frame, a profile is defined: S_{2D}(n, x, y, t), with index n, frame t and peak position (x_n, y_n) in the region of interest (ROI). Figure S2.7a is a representative 2D spectrum profile of the 43th frame of NP1 in Figure S2.6: S_{2D}(1,x,y,43). Only frames with NPs in the blinking-on state are retained (from the full set of 200~300 frames) by applying a threshold filter. The threshold (*Th*) is defined as the mean value of the total integrated intensity of individual NP, $Th(n)=\frac{1}{T}\sum_{t,x,y} S_{2D}(n,x,y,t)$ where T is the total length of the movie. Signals of frames with total integrated intensity $\left(=\sum_{x,y} S_{2D}(n,x,y,t)\right)$ larger than *Th* are retained and their spectrum is reduced to a 1D spectrum profile by integrating over the Y-axis: $S_{1D}(n,x,t)=\sum_{y} S_{2D}(n,x,y,t)$. $S_{1D}(n,x,t)$ is then fitted by a 7th order polynomial F(n,x,t) (since spectra were not fitted well by Gaussians or Lorentzians). Figure S2.7b shows S_{1D} for the data shown in Figure S2.7a.

(iv) Final data reduction and presentation: S_{1D} and F data (excluding blinking-off frames) are further divided into Von and Voff frames which are used for the construction of average spectra (as in Figures. 2.1c, 2.2c, 2.4c) by averaging S_{1D}(n, x, t) and the construction of spectral peak position histograms (Figures. 2.1d, 2.2d, 2.4d) by tabulating peak positions (x_{peak}) of F(n, x, t) for Von and Voff frames respectively. Finally, the X-axis is converted to wavelength by quadratic fitting to the calibration data (taken with 2 lasers and 1 LED spectral lines,). The differential spectrum (Figure 2.1e, 2.2e, 2.4e) is acquired by subtracting Voff averaged spectrum from Von averaged spectrum.

SI-2.5 Simulation method

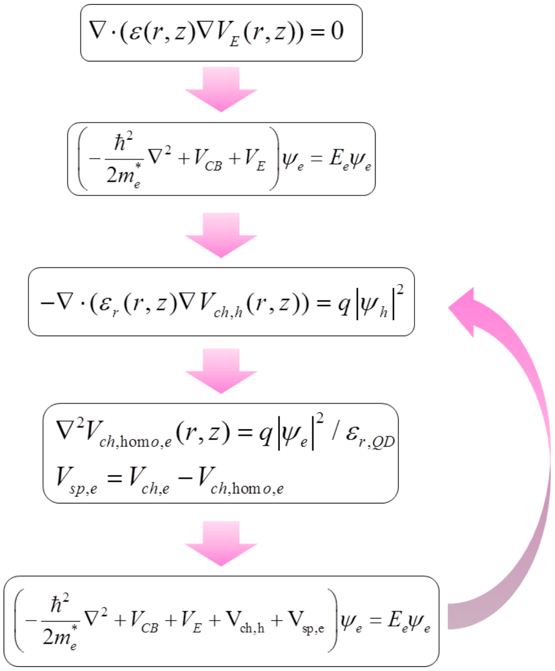

$$\nabla\cdot(\varepsilon(r,z)\nabla V_E(r,z))=0$$

$$\left(-\frac{\hbar^2}{2m_e^*}\nabla^2+V_{CB}+V_E\right)\psi_e=E_e\psi_e$$

$$-\nabla\cdot(\varepsilon_r(r,z)\nabla V_{ch,h}(r,z))=q\left|\psi_h\right|^2$$

$$\nabla^2V_{ch,\mathrm{homo},e}(r,z)=q\left|\psi_e\right|^2/\varepsilon_{r,QD}$$
$$V_{sp,e}=V_{ch,e}-V_{ch,\mathrm{homo},e}$$

$$\left(-\frac{\hbar^2}{2m_e^*}\nabla^2+V_{CB}+V_E+\mathrm{V}_{\mathrm{ch,h}}+\mathrm{V}_{\mathrm{sp,e}}\right)\psi_e=E_e\psi_e$$

Fig. S2.8 Quantum calculation flow chart

QCSE is calculated by solving the self-consistent Schrödinger-Poisson equations using a home-written Matlab program. Cylindrical symmetry was employed using a finite difference mesh. On every discretized mesh point, Schrödinger and Poisson equations were solved by assuming effective masses and self-consistent field approximation. The code generates electron's and hole's energy levels, overlap integral, and exciton binding energy by solving the coupled Schrödinger-Poisson equations iteratively using the finite difference method. To achieve three dimensional calculation with manageable computational effort, I apply axial (cylindrical) symmetry to the geometry and Laplacian operators for homogeneous space (or gradient and divergence operators for inhomogeneous space) in the coupled equations. The entire computational space extends 3~5nm further from the NP boundary (allowing for e and h wavefunctions to extend outside of the NPs' boundaries and decay into free space). Figure S8 presents the flow diagram for these calculations. First I define geometry and geometry-dependent parameters such as effective masses (m*(r,z)), dielectric constants (ε_r(r,z)), and conduction and valence band profiles (V_{CB} and V_{VB}). Parameters and their references used in this calculation are summarized at Tables S2.1 and S2.2. At the NP boundary, ε_r is assigned the average value of the NP and air dielectric constants. The potential generated by the external electric field (V_E) is calculated by solving the Laplacian equation $\nabla\cdot(\varepsilon_r(r,z)\nabla V_E(r,z))=0$ with the boundary condition: ($V_E(z=0)=0$, $V_E(z=d)=qF\times d$), where F is the electric field, and d is the total length of the computational space. With these potentials at hand, the Schrödinger equations for the electron:

$$\left(-\frac{\hbar^2}{2m_e^*}\nabla^2+V_{CB}+V_E\right)\psi_e=E_e\psi_e$$

and for the hole:

$$\left(-\frac{\hbar^2}{2m_h^*}\nabla^2+V_{VB}-V_E\right)\psi_h=E_h\psi_h$$

are solved next (using the Dirichlet boundary conditions). After normalization of the wavefunctions, the Poisson equation $-\nabla\cdot(\varepsilon_r(r,z)\nabla V_{ch,h}(r,z))=q\left|\psi_h\right|^2$ is solved (with a Dirichlet boundary condition) to derive the hole coulomic potential $V_{ch,h}$. The electron coulomic potential $V_{ch,e}$ is obtained in a similar way. In addition to the potential generated from the other particle, each particle is influenced by its own self-polarization potential ($V_{sp,e}$, $V_{sp,h}$) [76],[77] arising from the dielectric mismatch with its surrounding. $V_{sp,e}$ is calculated using: $V_{sp,e}=V_{ch,e}-V_{ch,homo,e}$ and

$V_{ch,homo,e}$ is calculated using: $\nabla^2 V_{ch,homo,e}(r,z) = q\left|\psi_e\right|^2 / \varepsilon_{r,QD}$. $\varepsilon_{r,QD}$ is the dielectric constant of the NP (which has a constant value). $V_{sp,h}$ is obtained similarly. With these potentials, Schrödinger equations are solved again for e and h with all of the contributions to the potentials:

$$\left(-\frac{\hbar^2}{2m_e^*}\nabla^2 + V_{CB} + V_E + V_{ch,h} + V_{sp,e}\right)\psi_e = E_e\psi_e$$

$$\left(-\frac{\hbar^2}{2m_h^*}\nabla^2 + V_{VB} - V_E + V_{ch,e} + V_{sp,h}\right)\psi_h = E_h\psi_h$$

This process is repeated iteratively until the electron (or/ and hole) energies converge. In most cases, four iterations are sufficient to obtain a convergence error of $\Delta E_e/E_e \leq 0.1\%$.

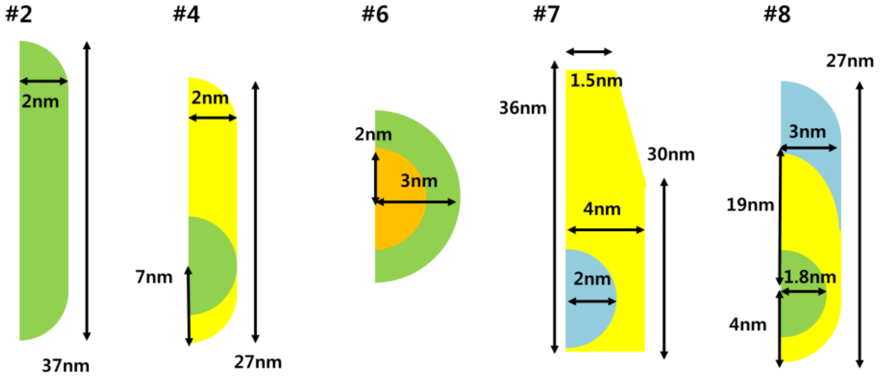

Fig S2.9 Simulated geometries for samples #2, #4, #6, #7, #8. CdSe (green), CdS (yellow), CdTe (orange), ZnSe (#7, cyan), CdZnSe (#8, cyan)

Geometries used for simulation are shown in Figure S2.9. Parameters used in this study were obtained from the literature [60],[61],[62],[63] and are summarized in Table S2.1 and S2.2 For simplicity, the same dielectric constant ($\varepsilon_r = 9$) was applied for the all samples, and the dielectric constant of air ($\varepsilon_r = 1$) was assumed for the immediate surroundings of the NP. Conduction band (Δe) offset between CdS-CdZnSe is assumed to have 0.3eV which is a medium value of CdSe-

CdS and ZnSe-CdS. Valence band offsets (Δh) of sample #8 are assumed to be zero except CdS-CdZnSe interface in order to ignore type-I transition and only take account type-II transition.

	CdSe	CdTe	CdS	ZnSe
m^*_e	0.13	0.11	0.2	0.14
m^*_h	0.45	0.35	0.7	0.53

Table S2.1 Electron and hole effective masses

	CdSe-CdTe	CdSe-CdS	CdS-ZnSe
Δ_e	0.42	0.2	0.8
Δ_h	-0.57	0.78	-0.52

Table S2.2 Conduction and valence band offsets. For example, Conduction band edge of CdTe is 0.42eV higher than CdSe. Unit is eV.

Chapter 3

Electric field dependent Auger recombination rate in semiconductor nanoparticle

3.1 Introduction

As semiconductor material is miniaturized in nanoscale, unique optical properties emerge due to the quantum confined effect. This brings quantized energy level in semiconductor compared to the continuous energy levels in bulk semiconductor. Among them, zero dimensional (0D) semiconductor possesses δ-function like density of state (DOS), exhibiting narrow full-width half maximum (FWHM, ~30nm) compared to the organic fluorophore (FWHM ~ 100nm). This 0D semiconductor is called as QD, or dubbed as 'artificial atom' due to its discrete energy levels. In addition, its emission wavelength is controlled by QD size, so that it covers wide range of spectrum. For example, CdSe and CdS heterostrucutred QD's emission spectrum covers entire visible range. Moreover, increased DOS at lowest energy brings enhanced light emitting property, so it is investigated as a light emitting diode (LED)[78], or laser. Especially QD laser is known for possessing the lowest lasing threshold for semiconductors[26].

The major drawback for using QD as light emitting purpose is its increased Auger recombination rate (Chapter 1.4). Auger rate (k_A) is nonradiative transition and it is inversely proportional to semiconductor's volume ($k_A \propto Vol^{-1}$). Thus, it is one dominant transition in QDs or nanorods (NRs), while k_A is negligible in bulk semiconductors. Auger recombination process deteriorates the nanoparticles (NPs)'s emitting property. It reduces overall fluorescence quantum yield (QY). More importantly, it induces emission photon's intermittency[79] (called as blinking) (Fig. 1.5d). If nanoparticles (NPs) have multiple excitons $\langle N \rangle > 1$, Auger channel is activated since k_A is much faster than radiative transition rate (k_r). After Auger recombination, either an electron or a hole is remained in NPs. They become negative or positive trion if they are excited again, and an electron and a hole recombine with Auger process. Therefore, NPs cannot emit photons until it becomes neutralized. This totally dark state and light emitting state are repeated random manner (blinking)[79].

Therefore, suppression of blinking is one major goal for utilizing NPs as stable fluorophore. Considerable efforts have been invested in designing NPs with reduced Auger recombination and blinking, such as via graded shells[80, 81], increased shell thickness[82], type-II shells[83] and alloying[84]. These approaches relax the momentum conservation requirement between the ground and excited states by 'smoothing' the otherwise abrupt changes in the conduction and valence band energies at the interfaces[80].

This Chapter reveals that the momentum conservation for satisfying Auger transition can be altered by applied electric field (F). First, theoretical analysis estimates the F-dependent k_A by solving Fermi's Golden Rule (FGR) at different F. Second, experimentally obtained quantum-confined Stark effect (QCSE) data exhibits reduced intensity for blue-shifted ZnSe-CdS NR which indicates increased k_A. These findings demonstrate voltage dependent nature of Auger process. Since, Auger recombination influence on emission intensity in multiple exciton or trion state (X^+), k_A change should be taken into account for intensity monitoring under F or measuring membrane potential with intensity (Chapter 4).

3.2 Calculation detail

Home-built python code is used to calculated F dependent k_A. It is constructed in one dimension (1D) finite difference method. Material parameters are shown in Fig. 3.1 and Table 3.1. Here, two model systems are under investigated which are homogeneous CdSe and asymmetric ZnSe-CdS NRs. CdSe is type-I energy structured and ZnSe-CdS is asymmetric type-II energy structured which has built-in dipole moment of excited electron and hole.

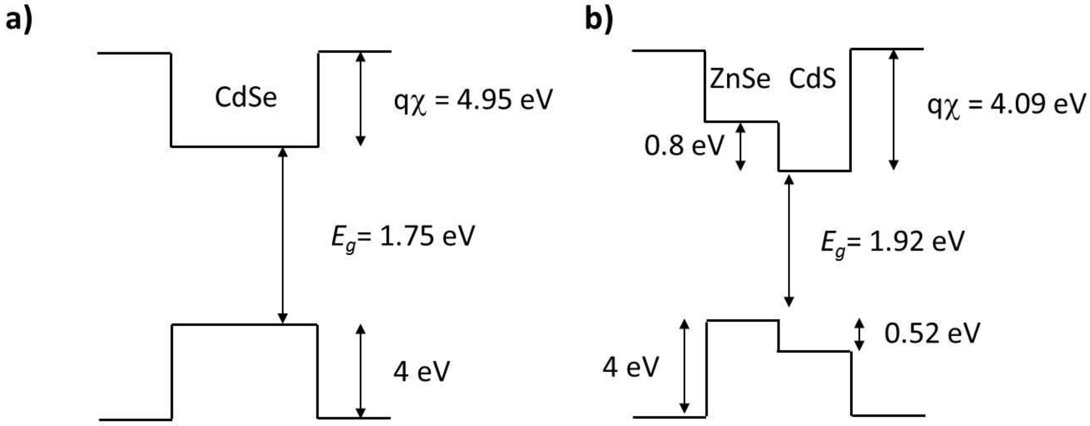

Fig. 3.1 Energy band structure of (**a**) CdSe and (**b**) ZnSe-CdS

	CdSe	ZnSe-CdS
m_e^*	0.13	0.21
m_h^*	0.45	0.7
ε_r	9.5	8.9
K	20	23

Table 3.1. Parameters used for calculation. m_e^*, and $m_h^*$are electron and hole effective masses. ε_r is dielectric constant. K is Kane matrix element. For ZnSe-CdS, averaged parameters of ZnSe and CdS are used.

Self-consistent Schrödinger and Poisson equation are solved until electron energy converges with *ΔE* < 1 meV (see self-consistency method in Chapter 2.8) to obtain wavefunctions. For a specific, two band Kane model are used in K·P formalism.

$$H = \begin{pmatrix} H_e & K\cdot\hat{p} \\ K\cdot\hat{p} & H_h \end{pmatrix} \quad \text{with:} \quad H_{e,h} = \pm\,\hat{p}^2\big/2m^*_{e,h} \ \pm E_g\big/2 \pm V_{e,h} \ \pm V_F \pm V^{e,h}_{coul}$$

K is the Kane matrix element, $\hat{p}$ is the momentum operator ($\hat{p} = -i\hbar\nabla$), E_g is the energy bandgap, $m^*_{e,h}$ are the electron and hole effective masses respectively, $V_{e,h}$ are the electron and hole confinement energies respectively, V_F is the potential generated by the applied electric field *F* ($V_F = x\cdot F$ where x is the spatial coordinate along the NR's long axis), and $V^{e,h}_{coul}$ is coulomb potential, describing attraction from the other charge.. $V^{e,h}_{coul}$ is calculated by inhomogeneous Poisson equation $-\nabla\cdot\left(\varepsilon_r(x)\nabla V(x)\right) = \rho(x)\big/\varepsilon_0$. Calculated wavefunctions are used for solving FGR at different *F*.

Auger recombination is a three particles process that results in a nonradiative transition due to the absorption of the exciton's energy by the spectator particle (Fig. 3.2b, c).

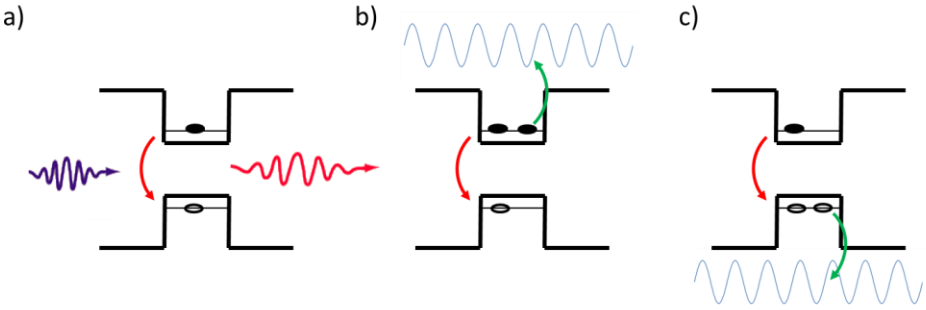

Fig. 3.2 Energy transition in QD **(a)** Radiative transition (blue) Absorbed photon (red) Emitted photon. **(b, c)** Auger recombination (e-e-h for **b**) (e-h-h for **c**)

The FGR expects the Auger recombination rate (k_A)

$$k_A = \frac{1}{\tau_A} = \frac{2\pi}{\hbar}\left|M_{if}\right|^2 \rho(E_f)$$

$$M_{if} = \left\langle \Psi_i \middle| V(x_1 - x_2) \middle| \Psi_f \right\rangle$$

where M_{if} is the matrix element describing coulomb potential between particles, τ_A is Auger recombination lifetime, $\rho(E_f)$ is density of states at E_f and E_f is the energy level of spectator particle's final state. The two particle initial and final wavefunctions are

$$\Psi_i(x_1, x_2) = \frac{1}{\sqrt{2}} \psi_h^0(x_1)\psi_h^0(x_2)[\lambda(1)\beta(2) - \lambda(2)\beta(1)]$$

$$\Psi_f(x_1, x_2) = \frac{1}{2}[\psi_e^0(x_1)^* \phi_f(x_2) + \psi_e^0(x_2)^* \phi_f(x_1)][\lambda(1)\beta(2) - \lambda(2)\beta(1)]$$

ψ_e^0, ψ_h^0 are electron's and hole's ground state. λ and β are spinors of the state. In final state, the spectator hole is excited in the continuum space, so it is expressed as a plane wave $\phi_f(x) = \frac{1}{\sqrt{L}}\exp(ik_f x)$ where L is a normalization factor. The other hole is in conduction band, expressed as complex conjugate of the electron's ground state ψ_e^{0*}. Having the initial and final states, matrix element is calculated.

$$\begin{aligned} M_{if} &= \left\langle \Psi_i \left| V(x_1 - x_2) \right| \Psi_f \right\rangle \\ &= \sqrt{2} \int dx_1 dx_2 \psi_h^0(x_1)^* \psi_h^0(x_2)^* V(x_1 - x_2) \psi_e^0(x_1)^* \phi_f^0(x_2)^* \end{aligned}$$

Coulomb potential is defined as $V(x_1 - x_2) = \dfrac{e^2}{4\pi\varepsilon_r\varepsilon_0 \left| x_1 - x_2 + \delta \right|}$ where δ is chosen 10^{-2} nm to prevent divergence. This value is numerically calculated on the one dimension (1D) finite difference method. I obtain k_A values at different electric field, and NRs' length. k_A was calculated only for the electron-hole-hole ($e-h-h$) scattering configuration (Fig. 3.2c). This configuration is more likely to occur than the electron-electron-hole ($e-e-h$) scattering configuration (Fig. 3.2b). This is because that in general hole confined volume is much smaller than electron covering area in ZnSe-CdS or CdSe-CdS NR. Therefore, we expect stronger hole confinement than electron, which results in higher scattering rate between holes than between electrons. The calculation method used here is referred from ref. [80].

3.3 Calculation results

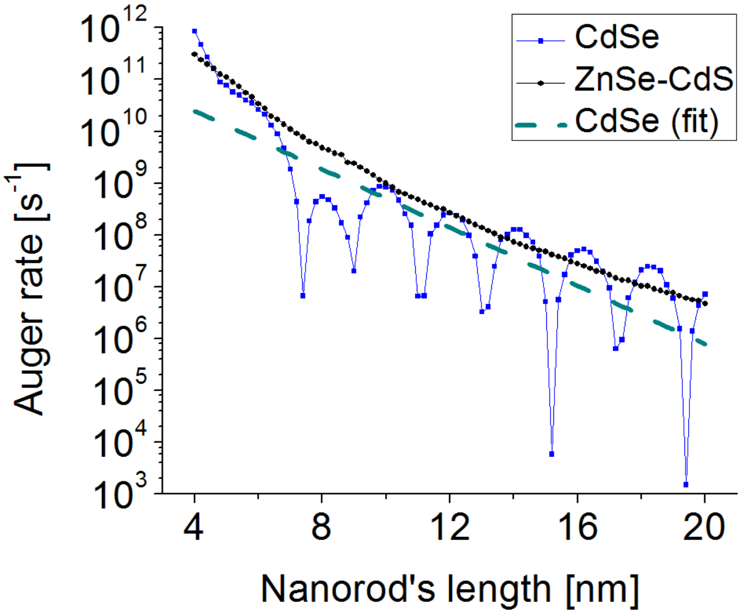

Fig. 3.3 Length-dependent Auger rate of CdSe (blue) and its fitting curve (green dash line) and ZnSe-CdS (black).

Fig. 3.3 shows the length dependent k_A of CdSe and ZnSe-CdS. Interestingly, there is repeating drops in k_A for CdSe as its length increases. Since $\phi_f(x) = \frac{1}{\sqrt{L}} \exp(ik_f x)$ has strong oscillatory behavior, low frequency component of $\psi_h^0(x_2)^*$ is canceled out for calculating M_{if} due to the symmetry requirement. Thus high frequency component (close to k_f) becomes significant. At certain lengths, high frequency component vanishes which results in orders of magnitude suppressed k_A. For an actual measurement, this oscillation is averaged out for numerous reasons including environmental effect, imperfection of NP's size and shape [80]. On the other hand, this oscillatory behavior is not shown in ZnSe-CdS due to the collapse of symmetry in this material. k_A is generally reduced as length increases ($k_A \propto Vol^{-1}$ for 3D).

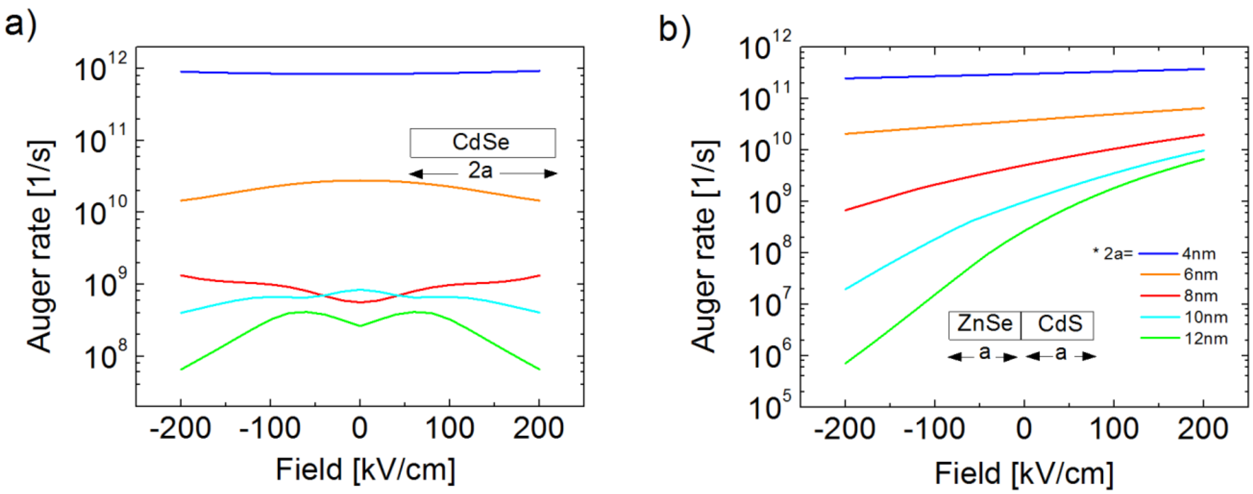

Fig. 3.4 F-dependent k_A (**a**) CdSe (**b**) ZnSe-CdS (black) total length is 4nm (blue), 6nm (orange), 8nm (red), 10nm (cyan), 12nm (green)

Figs. 3.4a and b show calculated Auger recombination rates (k_A) for the two NPs as a function of F. Our calculations show that k_A is rather invariant for 4nm CdSe. This is due to the strong Coulomb interaction between an electron and a hole. Therefore, their wavefucntions do not change under F (Fig. 4. 2). Except 8 nm CdSe, k_A shows reduced its value under both positive and negative F. Under F, electron's and hole's wavefunctions are separated each other (for type-I energy band), so their Coulomb interaction $V(x_1 - x_2) = \dfrac{e^2}{4\pi\varepsilon_r\varepsilon_0 |x_1 - x_2 + \delta|}$ is diminished, which affects reduced k_A. For 8nm CdSe, it is the verge of the magic size where k_A is suppressed (Fig. 3.3). So it is even smaller in F=0 than $F > 0$.

For ZnSe-CdS, k_A is enhanced under positive F where an electron and a hole is pushed towards type-II interface, and is reduced under negative F where an electron and a hole is separated towards the other direction. Here, it is found that k_A suffers 4 orders of magnitude change in its value while F change from -200 to +200 kV/cm, demonstrating its high F sensitivity. k_A is not direct observable, so it will be extracted from lifetime or inferred from intensity information.

3.4 Experimental results

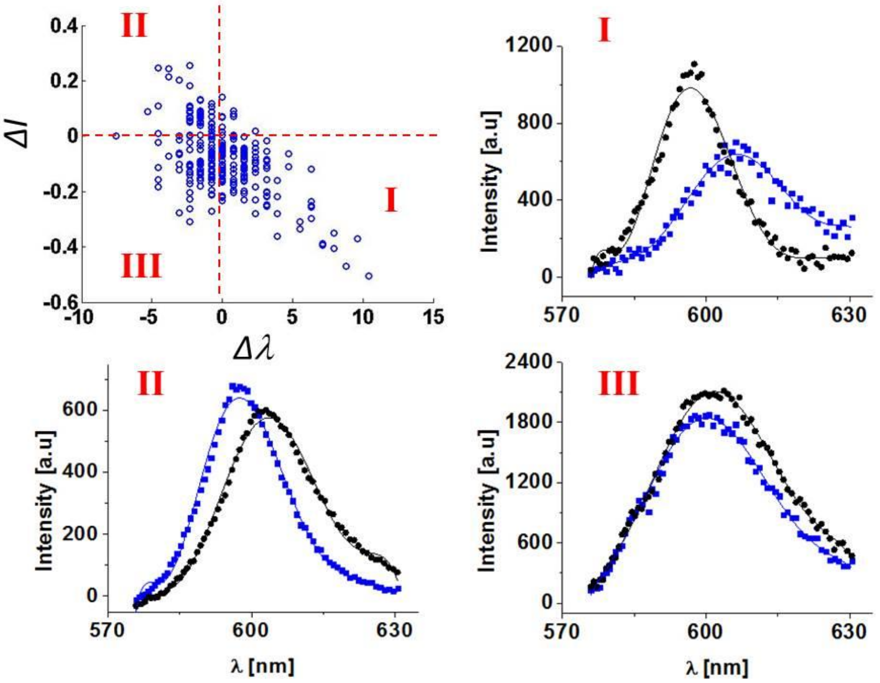

Fig. 3.5 Intensity variation along with Stark shift (**I**) intensity increase (**II**) intensity reduction (**III**) histogram of intensity when blue-shifted spectrum. (Black) spectrum without F. (Blue) Spectrum at $\boldsymbol{F}$=400 kV/cm

Increase Auger recombination at certain *F* is confirmed by QCSE experiment. In previous study, our ZnSe-CdS NRs are reported to have asymmetric energy band, and approximately linear ΔE-ΔF relation in Fig. 2.6c. Thus, they show both blue- and red-shift under *F* at different orientation with respect to *F*. According to the theoretical results in Fig. 3.4, ZnSe-CdS shows increase k_A at positive *F* where blue-shift occurs. Consequently, we expect reduced intensity under blue-shifted spectrum. ZnSe-CdS NRs (sample #7 in Chapter 2) are located under QCSE *F*-modulation microscopy (Chapter 2), and 400kV/cm *F* is applied to the interdigitated electrode (Fig. S2.3). Actual *F* applied to the NRs, or Field inside NRs (F_{int}) is expected to be 40 kV/cm from the calculation in Chapter 2.

275 samples are tested, and formatted in scatter plot $\Delta I = (I_{400kV/cm} - I_{0kV/cm}) / I_{0kV/cm}$ over Δλ in Fig. (3.5). There are three distinct regions; (I) red-shifted and intensity reduced, (II) blue-shifted and intensity increased, (III) blue-shifted and intensity reduced. Representative spectra of each region are shown in the subplot of Fig. 3.5 (I, II, III). 36.3%, 15.6%, and 32.3% of them are assigned in region I, II and III, respectively. Intensity reduction with emission spectrum red-shift is well-known QCSE (region I). Compared to the red-shifted region I, blue-shifted region has wide range of *ΔI* distribution. If electron and hole wavefunctions are close each other (blue-shifted), their overlap integral (*f*) is increased, resulting in increased k_r and emission intensity. However, 32.3% of total NPs show reduced intensity (region III) rather than showing increased *ΔI* in region II*,* confirming increased nonradiative recombination. k_A is the dominant nonradiative transition in NPs. For those samples that does not satisfy momentum conservation in Auger transition, it shows increased intensity (region II).

3.5 Summary

In this chapter, I first introduce the *F*-dependent Auger rate. Until now, energy (or wavelength) shift or intensity variation have been discussed in the context of QCSE. However, theoretical investigation finds that Auger recombination rate is even more sensitive to the *F* than other observables. Intensity reduction in wavelength blue-shifted QCSE confirms the increased Auger process in type-II ZnSe-CdS. Consequently, these findings suggest that k_A should be taken into account for recording membrane potential by intensity (Chapter 4) or for nanoscale field (or voltage) sensor. These findings should be taken into account for designing other optical devices including LED, laser, photovoltaics since NPs in those devices are under biased.

Chapter 4

Self-consistent Schrödinger-Poisson calculation and performance prediction and design rules for membrane-embedded semiconducting voltage sensing nanoparticles

4.1 Introduction

In order to understand the brain, tools need to be developed to allow the investigation of interactions between individual neurons[85, 86]. Multi-electrode recordings have provided important insights but have limited performance when dense local circuits need to be analyzed or when signals from specific types of near-by neurons need to be distinguished. For this reason, considerable efforts have been invested in developing optical detection methods[87], including the utilization of voltage-sensitive dyes (VSDs)[88]. VSDs could potentially allow simultaneous visualization of neuronal activity over a large number of neurons in a large field-of-view and with superresolution. Moreover, targetable VSDs could report signals from specific types of neurons.

As examples, synthetic and genetically encoded fluorescent Ca^{2+} indicators have gained great prominence and are routinely used to study Ca^{2+} signals in cultured neurons, brain slices, and live brains. Such indicators allow the recording of the dynamics of Ca^{2+} signals over large sets of individual neurons of known types. Although Ca^{2+} dynamics is correlated to neuronal spiking, Ca^{2+} signals do not report neuronal spiking signals faithfully due to their slow kinetics and signal saturation. In contrast, VSDs afford direct imaging of cellular membrane action potentials (AP). Indeed, organic VSDs have allowed the functional mapping of brain activities in individual cells, in invertebrates, in mammalian brain slices, and even in whole brains of awake mammals[88]. Most VSDs report on voltage changes via changes in their fluorescence intensity, but ratiometric VSDs have also been demonstrated[89]. VSDs, however, suffer from some shortcomings. They could alter membrane capacitance, be phototoxic, suffer from photobleaching, have a short retention time in the membrane, and miss-target the membrane, resulting in nonspecific background labeling. More recently, several genetically-encoded fluorescent voltage-sensor proteins (VSPs) have been developed and used to detect aggregate neural activity *in vivo* and single spikes *in vitro*[8]. Hybrid approaches (combining membrane-targeted fluorescent proteins with VSDs) have also been recently reported, but they suffer from slow kinetics, limited dynamic range, low quantum yields, and perturbation to membrane capacitance[90]. Unfortunately, despite these advances, VSDs and VSPs are not yet preforming at the level of detection where every single action potential, in every neuron, in a large field-of-view, in the brain of a live animal, could be recorded. Promising results, however, have been recently demonstrated with ArcLight VSP[9].

In Chapter 2, I examined bandgap-engineered colloidal semiconductor nanoparticles, dubbed voltage-sensing nanoparticles (vsNPs) that display large quantum-confined Stark effect (QCSE) at room temperature on the single particle level. In particular, I have shown that charge separation across one (or more) heterostructure interface(s) with type-II band alignment (and the associated induced dipole) is crucial for an enhanced QCSE[68]. The feasibility of utilizing such vsNPs for membrane voltage sensing was soon after theoretically investigated and favorably compared to organic VSDs[91]. Here I utilize self-consistent Schrödinger-Poisson calculations for vsNPs embedded in the membrane to further explore the feasibility and performance of vsNPs as voltage sensors, and to provide guiding principles for their design.

4.2 Calculation detail

All calculations were performed using a home-written code (using Python). Two types of vsNPs were examined as model systems: a simple cylindrical homostructure CdSe nanorod (NR) (Fig. 3.1a) and a heterostructure ZnSe-CdS NR with asymmetric type-II energy band alignment (Fig. 3.1b). First, inhomogeneous Poisson equation is calculated to obtain the electrostatic potential profile of the NR embedded in the lipid membrane:

$$-\nabla \cdot \left(\varepsilon_r(x,y)\nabla V(x,y)\right) = \rho(x,y)/\varepsilon_0$$

The NR, lipid membrane, and the surrounding physiological buffer are modeled in two dimensions (2D) with cylindrical symmetry and a finite difference grid (FDM) with a grid mesh size of 2 Å. The entire simulation space spans 8 nm × 20 nm (width × length). The lipid membrane (of 4 nm thickness) is located at the center of the simulated space. The NR (of 2 nm radius) is symmetrically embedded in the membrane and its length is varied from 4 nm to 12 nm (Fig. 4.1b). Each region is parameterized with its corresponding dielectric constant (Fig. 4.1b and Table 3.1). Neumann boundary conditions are applied to the simulation boundaries to maintain potential continuity ($\Delta V = 0$ at the boundaries). Membrane potential is established by applying a thin sheet of charges $[C/m^2]$ justified by the very short Debye screening length (≈ 0.7 nm) of a physiological buffer. Having the sheet of charges and the map of dielectric constants as inputs (Fig. 4.1b), the Poisson equation returns the electrostatic potential across the entire simulation space, providing the relation between membrane potential (V_m) and electric field (F_{int}) inside the NR (Fig. 4.1c).

With the internal electric field F_{int} at hand, I solved the Schrödinger equation using the two band $K \times \hat{p}$ (Kane) model to obtain the electron's (*e*) and the hole's (*h*) wavefunctions (ϕ_e, ϕ_h) and their ground state energies (E_e^1, E_h^1) at different electric fields. This simulation was implemented in 1D FDM to further reduce the mesh size to 0.2 Å (2D FDM with a larger mesh failed to model the high spatial frequency plane wave that describes the excited state's hole in calculating Auger recombination rate (k_A). The Kane Hamiltonian is given by:

$$H = \begin{pmatrix} H_e & K \cdot \hat{p} \\ K \cdot \hat{p} & H_h \end{pmatrix} \quad \text{with:} \quad H_{e,h} = \pm \hat{p}^2 / 2m_{e,h}^* \ \pm E_g/2 \pm V_{e,h} \ \pm V_F$$

where K is the Kane matrix element, $\hat{p}$ is the momentum operator ($\hat{p} = -i\hbar\nabla$), E_g is the energy bandgap, $m^*_{e,h}$ are the electron and hole effective masses respectively, $V_{e,h}$ are the electron and hole confinement energies respectively, V_F is the potential generated by the F_{int} ($V_F = x \times F_{\text{int}}$ where x is the spatial coordinate along the NR's long axis), and $V^{e,h}_{coul}$ is coulomb potential, describing attraction from the other charge. This Poisson and Schrödinger equations are self-consistently solved until electron's energy converges with $\Delta E < 1$ meV. As a validation step, I successfully reproduced previously published calculations for $V_F = 0$ [80, 83]. With the calculated electron's and the hole's wavefunctions and corresponding energies at hand, I could calculate in a third step the Stark-shift (ΔI), the Auger recombination rate (k_A), and the overlap integral between the *e* and *h* wavefunctions (f). By combining the derived V_m - F_{int} relation from the Poisson equation in cylinder and the derived F_{int} - ΔI relation and k_A and f from the self-consistent Schrödinger-Poisson equation, ΔI, k_A, and f are extracted at each V_m. Previously reported methodology to calculate k_A is used here[80]. The relative radiative recombination lifetime $\Delta\tau_r$ and the NRs' emission intensity ΔI were then calculated from f and k_A. τ_r is given by $\tau_r = \frac{2\pi\varepsilon_0 m_0 c^3 \hbar^2}{\sqrt{\eta} e^2 E_{ex} K f}$ where m_0 is the free electron mass, c is the speed of light, $\hbar$ is the reduced plank constant, ε_o is the vacuum permittivity, η is the refractive index for the NRs (2.5 for both CdSe and ZnSe-CdS), K is the Kane matrix element, and E_{ex} is the energy of emitted photon[92]. The total emission intensity ΔI was calculated as a weighted sum of the exciton's (X) (dominant at low light excitation) and the positive trion's state $\left(X^{+}\right)$ (dominant at high light excitation) emission intensities for varying relative weights. This was done in order to evaluate the contribution of Auger recombination to voltage sensing performance by voltage sensing NRs (vsNRs). This sequence of calculations was repeated for resting- and action-potential- like membrane voltages.

4.3 Electrostatic profile of membrane inserted nanorod

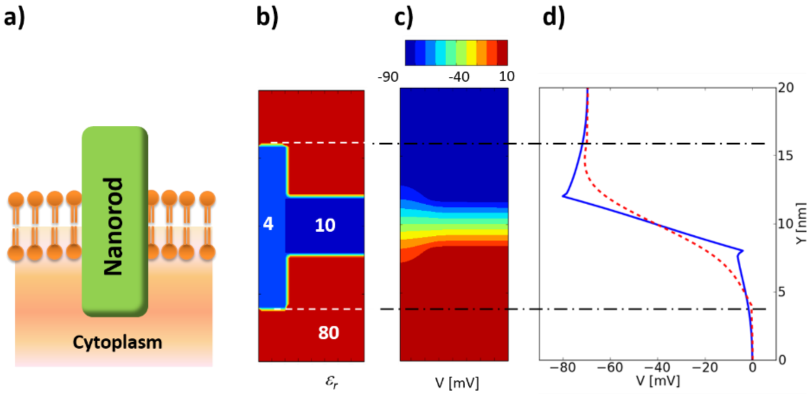

Fig. 4.1 Calculated potential of the inserted NR in membrane. (**a**) Schematic of NR embedded in membrane. (**b**) Dielectric constants ε_r: intra- and extra-cellular (red): 80, lipid (dark blue): 4, NR (light blue) 10. ε_r's at the boundaries and interfaces are averaged. (**c**) Color map of the calculated potential profile of geometry (**b**) when V_m = 70 mV. (**d**) 1D potential profile across the NR (dashed red line) and outside of the NR (solid blue line). Dashed-doted black lines mark the top and bottom of the NR.

The magnitude of the internal electric field inside the NR, in response to the external membrane potential (V_m - F_{int} relation) was calculated by solving the Poisson equation for the dielectric distribution depicted in Fig. 4.1b. As an example, Fig. 4.1c shows the 2D potential profile of a 12 nm long NR at V_m = 70 mV. For this calculation, 0.8 mC/m^2 and 11.4 mC/m^2

of sheet charges were applied to the extracellular and the intracellular sides of the membrane respectively, corresponding to 7.9 mM and 117.9 mM charge density and 1 nm Debye screening length (on each side). Fig. 4.1d shows the potential profile across the long axis of the NR (dashed red line) and across the membrane away from the NR (solid blue line). In the absence of the NR, the potential drops entirely across the lipid membrane, due to the large difference in dielectric constants between water and lipids ($\varepsilon_r = 80$ vs $\varepsilon_r = 4$). Within the NR, the potential still drops across its entire length (confirmed for lengths from 4nm to 12nm) despite the fact that it protrudes the membrane on both sides. The average F_{int} inside the NR could therefore be simply approximated to be: $F_{\text{int}} = \Delta V / l = V_m / l$ (where l is the length of the NR). The internal electric field in the water-protruding ends does diminish, however, for longer l's. I therefore expect a trade-off between QCSE enhancement and reduction in F_{int} as function of l.

4.4 Self-consistent calculation on QCSE

The QCSE observables D/ and f, and k_A were calculated for type-I CdSe NRs (Fig. 3.1a) and 1 nm buffer layered ZnSe-CdS type-II heterostructure NRs (Fig. 3.1b) of varying lengths, from 4 nm to 12 nm (Fig. 4.2). Voltage-dependent spectral shifts and intensity (emission rate) changes in QDs and NRs were experimentally observed and theoretically treated [37, 45, 93, 56, 68]. Such changes depend on the geometry, composition, and heterostructure configuration of these nanoparticles (NPs)[68]. The effect of an applied voltage on the Auger recombination rate are represented here from Chapter. 3.

Figs. 4.2a, b and c show the calculated values for $\Delta\lambda$, k_A and f for the CdSe NR. Figs. 4.2d, e and f show the same for the Type-II ZnSe-CdS heterostructure NRs. As previously demonstrated[37, 45], a quadratic $\Delta\lambda-\Delta F$ relation and a red shift ($\Delta\lambda>0$) are calculated for the type-I CdSe NR. The quadratic relation is a manifestation of the particle's (and its bandgap's) symmetry. It indicates that there is no built-in dipole moment, and that the exciton's energy is always reduced under an applied field (i.e. red-shift in emission spectrum). In contrast, a roughly linear $\Delta\lambda-\Delta F$ relation and both a red shift ($\Delta\lambda>0$) and a blue shift ($\Delta\lambda<0$) that are dependent on the applied field direction are calculated for the Type-II ZnSe-CdS heterostructure NRs. This behavior is a manifestation of the particle's (and its bandgap's) asymmetry and the presence of a built-in dipole[68].

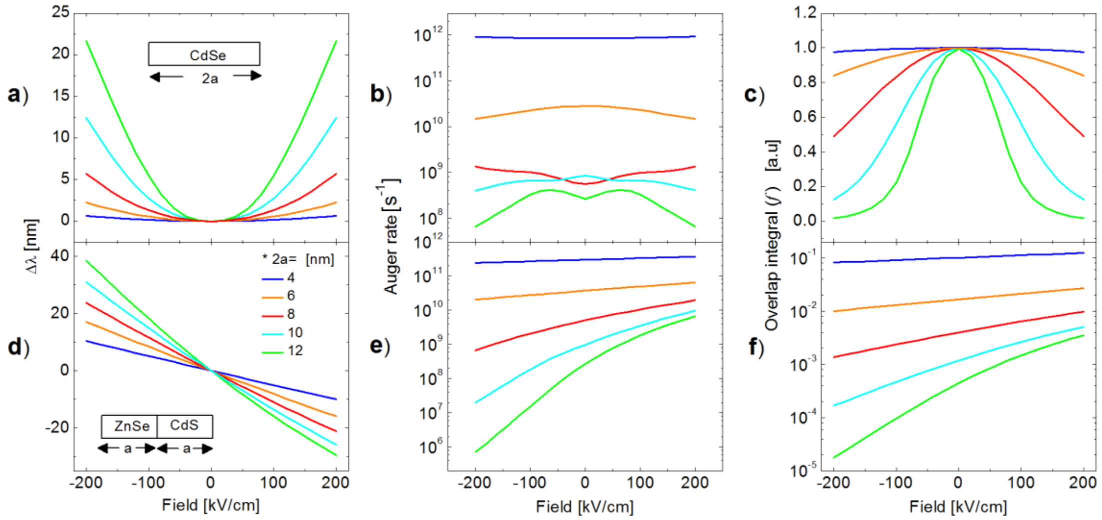

Fig. 4.2: Calculated values for $\Delta\lambda$ ((**a**) and (**d**)), k_A ((**b**) and (**e**)), and f ((**c**) and (**f**)) as function of applied field for CdSe NRs ((**a**), (**b**), and (**c**)) and Type-II ZnSe-CdS heterostructure NRs ((**d**), (**e**), and (**f**)). 4nm (blue), 6nm (orange), 8nm (red), 10nm (cyan), 12nm (green)

As can be seen from Figs. 4.2a and 4.2d, the sensitivity of the QCSE to the applied field (i.e. $\Delta\lambda/\Delta F$, the slope of the calculated curves) scales with the length of both types of particles. The Type-II ZnSe-CdS heterostructure NRs, however, exhibit a larger sensitivity and a larger QCSE shift per given applied field as compared to type-I CdSe NR.

Calculated Auger recombination rates (k_A) for the two nanoparticles as function of applied field are shown here again for comparing other observables. F-dependent k_A is discussed in Ch. 3. k_A is reduced as length increases for both CdSe and ZnSe-CdS NR. In addition, it is noteworthy that Coulomb interaction between e and h largely affects k_A. If e and h close approach (blue-shift in type-II ZnSe-CdS, positive F), k_A increases. On the other hand, k_A decreases and e and h separate each other in both positive and negative F for CdSe, and negative F for ZnSe-CdS (red-shift). The Auger rate influence directly on intensity (an experimental observable), which will be discussed in Fig. 4.4.

4.5 Performance prediction of membrane inserted nanorod

The overlap integral f is symmetric with respect to F_{int} for the type-I CdSe NR (Fig. 4.2c) and non-symmetric for the Type-II ZnSe-CdS heterostructure NRs (Fig. 4.2f). It is inversely proportional to the radiative lifetime τ_r (another experimental observable).

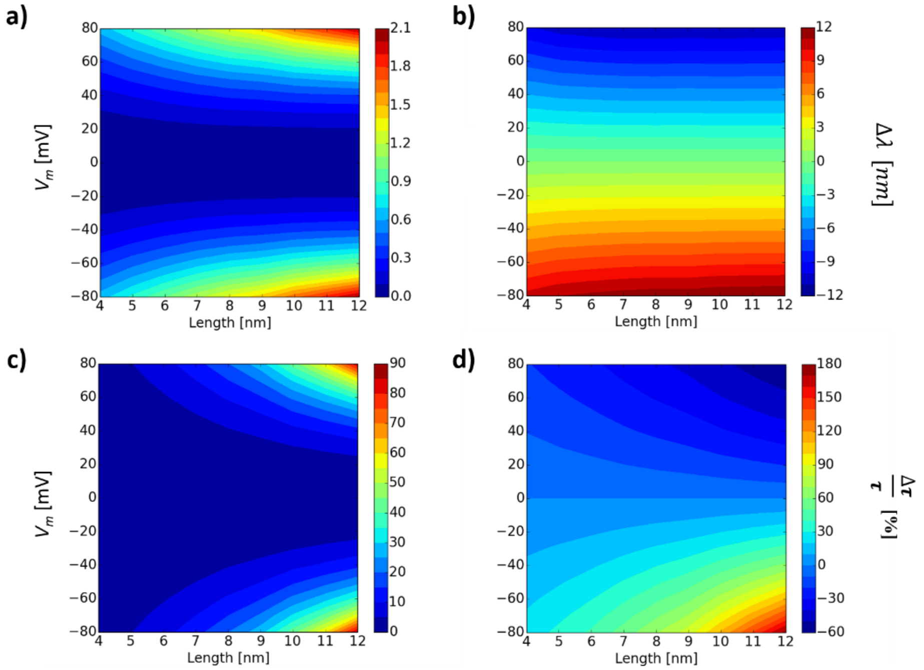

Fig. 4.3 Stark-shift (a, b) and relative radiative lifetime changes (c, d) for different length type-I CdSe NR (a, c) and type-II ZnSe-CdS heterostructure NRs (b, d), referenced to V_m=0.

With the approximation $F_{\text{int}} \approx \Delta V / l = V_m / l$ (Fig. 4.1), the F_{int}-driven potential energy operator can be written as: $V_F(x) = x \cdot F = xV_m / l$ and therefore the Hamiltonians for the two bands are: $H_{e,h} = \pm \hat{p}^2 / 2m^*_{e,h} \pm E_g/2 \pm V_{e,h} \pm V_F$. Solving the Schrödinger equation for *e* and *h* energies directly yields the QCSE's spectral shift dependence on the membrane voltage V_m (Fig. 4.3). Fig. 4.3a shows $\Delta\lambda$ for different length type-I CdSe NR. Fig. 4.3b shows $\Delta\lambda$ for different length type-II ZnSe-CdS heterostructure NRs. While longer NRs can give rise to a larger separation between the charges, and hence a larger dipole, F_{int} is decreased. $\Delta\lambda$ is therefore only moderately increased (in absolute value, for both red and blue shifts) as function of the NRs' length (Figs. 4.3a and b). $\Delta\lambda$ at $V_m = \pm 70$ mV is 1.5 nm red-shifted compared to V_m

= 0 mV for a 12 nm long CdSe type-I NR. It is only 0.5 nm red-shifted for a 4 nm long CdSe (similar to the shift Marshall *et al.* estimated for a 4 nm CdTe QD[91]. In contrast, 12 nm long Type-II ZnSe-CdS NR shows 10.3 nm red-shift at V_m = +70 or 9.5 nm blue-shift at V_m = -70 with respect to V_m= 0 mV. A 4 nm long ZnSe-CdS NR shows considerable red (9.0 nm) and blue (8.7 nm) shifts. Type-II NRs exhibit much larger shifts (even for the shortest NRs).

Figs. 4.3c and 4.3d show the relative change in the radiative lifetime $\Delta\tau_r / \tau_r$ [%] of CdSe type-I NRs (4.3c) and Type-II ZnSe-CdS NRs (4.3d). τ_r is calculated according to: $\tau_r = \frac{2\pi\varepsilon_0 m_0 c^3 \hbar^2}{\sqrt{\eta} e^2 E_{ex} K f}$ where m_0 is the free electron mass, c is the speed of light, $\hbar$ is the reduced plank constant, e_0 is the vacuum permittivity, η is the refractive index for the NRs (2.5 for both CdSe and ZnSe-CdS), K is the Kane matrix element, and E_{ex} is the energy of emitted photons[92]. $\Delta\tau_r / \tau_r$ is increased by only 2% for a 4 nm CdSe NR. This is likely due to strong *e* and *h* confinement in a small volume, with f hardly changing. However, $\Delta\tau_r / \tau_r$ increases by ~56 % for a 12 nm CdSe type-I NR. While $\Delta\lambda$ changes only weakly as function of voltage for Type-II ZnSe-CdS NR, $\Delta\tau_r / \tau_r$ exhibits a strong length dependence for these NRs. For 4 nm long type-II NRs, $\Delta\tau_r / \tau_r$ increases by 21 % for red-shifting field orientation, or reduced by 17 % for blue-shifting orientation. These changes are amplified to 140% (red-shifting) or reduced to 53 % (blue-shifting) for 12nm long type-II NRs. This $\Delta\tau_r / V_m$ sensitivity could be exploited by utilizing conventional fluorescence lifetime imaging microscopy (FLIM)[94] or wide-field FLIM using the singe photon counting H33D detector[95].

Using the overlap integral and the radiative lifetime calculations discussed above, one can estimate the sensor's fluorescence emission intensity ($I = QY \cdot \frac{\sigma}{\hbar\omega}$), which is an easily accessible observable of the QCSE. Here σ is the sensor's absorption cross section and QY is its quantum yield. To a first approximation, σ does not depend on V_m, so that $\mathrm{D}I \propto \mathrm{D}QY$. The overall QY of the sensor's fluorescence emission is assumed to be a linear combination of the QY's of the exciton (X) and the positive trion state (X$^+$), $QY = aQY^X + (1 - a)QY^{X+}$ with: $QY^X = k_r / (k_r + k_t)$ and $QY^{X+} = 2k_r / (2k_r + 2k_t + k_A)$ where a is the exciton's emission partition coefficient (relative weight) between the exciton (X) and the positive trion state (X$^+$), a weight that depends on the excitation intensity (a is close to one at low excitation power and close to zero at high excitation power). $k_r = \tau_r^{-1}$ is the radiative transition rate, and k_t is a charge trapping rate at the particle's surface (due to surface states).

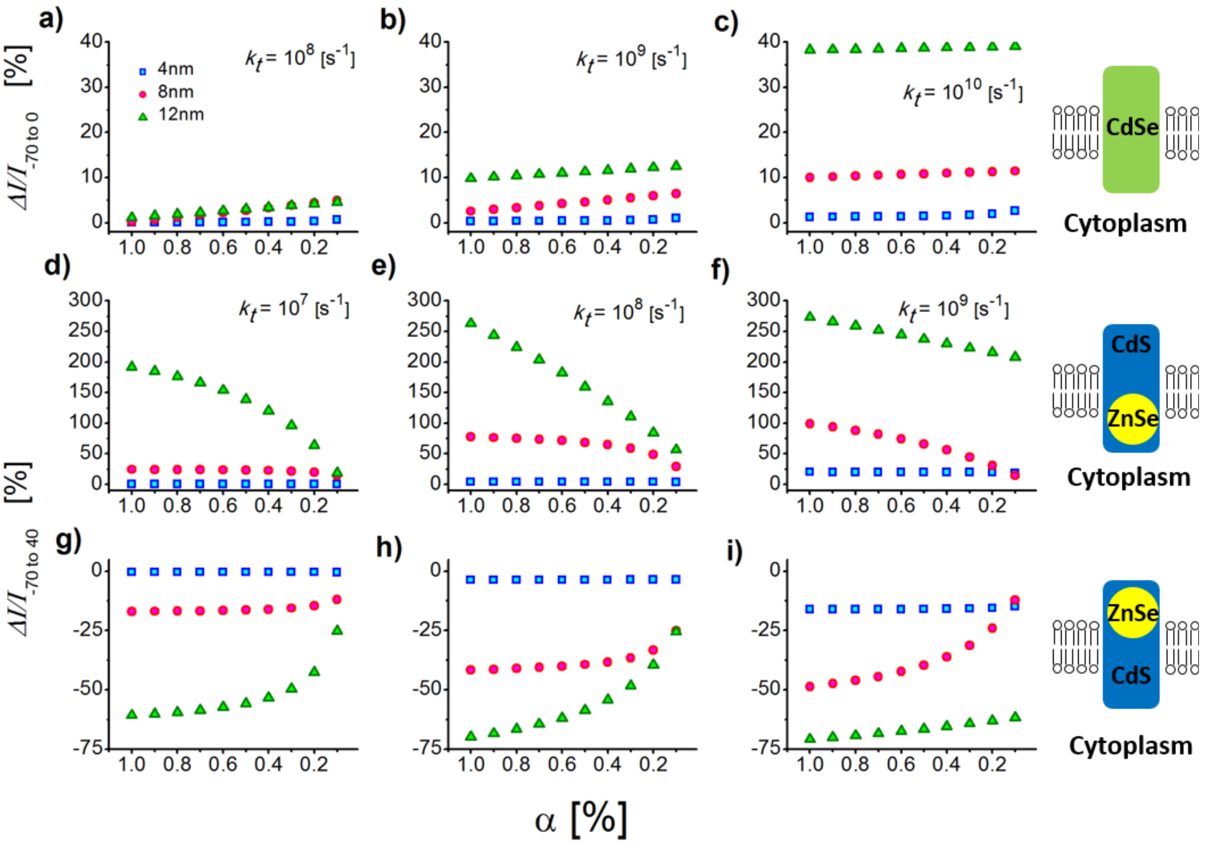

Fig. 4.4: Relative intensity change $\Delta I / I$ corresponding to a voltage sweep of an action potential calculated for 4nm (blue-square), 8nm (red-circle), and 12 nm (green-triangle) long NRs. (**a**~**c**) type-I CdSe NRs . (**d**~**i**) type-II ZnSe-CdS heterostructure NRs. (**d**~**f**) red-shifting geometry. (**g**~**i**) blue shifting geometry. k_t values used for the calculations are: 10^7s^{-1} (**d**, **g**), 10^8s^{-1} (**a**, **e**, **h**), 10^9s^{-1} (**b**, **f**, **i**), 10^{10} s^{-1} (**c**).

k_t is assumed not to depend on the action potential. Both the X and X$^+$ states are subjected to surface trapping (i.e. k_t affects both QY^X and QY^{X+}), but k_A affects only the X$^+$ state. The weights of k_r and k_t are doubled for the X$^+$ state, accounting for the presence of two holes in this state. Fig. 4.4 gives estimates for the maximum attainable $\Delta I / I$ under a full voltage sweep corresponding to an action potential, $\Delta I / I_{-70\to 0} = \dfrac{I(V_m = 0) - I(-70)}{I(-70)}$ for type-I CdSe NRs (Figs. 4.4a, b, c; $\mathrm{D}I$ is evaluated for half of the AP sweep, due to the quadratic dependence on the field), and $\Delta I / I_{-70\to 40} = \dfrac{I(40) - I(-70)}{I(-70)}$ for CdS type-II heterostructure NRs (Figs. 4.4d – i; $\mathrm{D}I$ is evaluated for the full AP sweep, due to the monotonic dependence on the field) for the red-shifting (Figs. 4.4d, e, f) and blue-shifting (Figs. 4.4g, h, i) geometries. All other parameter were derived from calculations described in Fig. 4.2. Three surface trapping rates $k_t = 10^8$ s^{-1} (Fig. 4.4a), $k_t = 10^9$ s^{-1} (Fig. 4.4b), and $k_t = 10^{10}$ s^{-1} (Fig. 4.4c) were used for CdSe type-I NRs since their fluorescence lifetime ($\tau = \tau_r^{-1} + \tau_A^{-1} + \tau_t^{-1}$) ranges between ~ 0.1ns - 100 ns. For type-II ZnSe-CdS heterostructure NRs, however, $k_t = 10^7$ s^{-1} (Figs. 3.7d and 3.7g), $k_t = 10^8$ s^{-1} (Figs. 4.4e and 4.4h), and $k_t = 10^9$ s^{-1} (Figs. 4.4f and 4.4i) were used due to their longer fluorescence lifetime (~ 10ns - 1000 ns).

For type-I CdSe, I found that $\Delta I / I_{-70\to 0}$ increases as longer length, at trion state, and low QY (large k_r). Although it turns out that $\Delta QY^{X+} > \Delta QY^{X}$ for this CdSe NR ($\Delta I / I_{-70\to 0}$ is larger at small α), it is only small increment. One strategy for considerable $\Delta I / I_{-70\to 0}$ is using longer and lower QY NR (Fig. 4.4c).

In contrast to small change in $\Delta I / I_{-70\to 0}$ for type-I CdSe NRs, type-II ZnSe-CdS heterostructure NRs exhibit large sensitivity in intensity. In addition, the orientation of this NR in the membrane affects the sign of the $\Delta I / I$ signal in response to membrane depolarization. When the hole-trapping part (ZnSe) is facing the cytoplasmic side (Figs. 4.4d, e, f), $\Delta I / I$ is positive (intensity is increased). When it faces the extracellular side (Figs. 4.4g, h, i), $\Delta I / I$ is negative (intensity is decreased). For both orientations, $\Delta I / I$ is larger for $\alpha \to 1$. It is therefore beneficial to run these sensors under weak excitation (favoring emission from the X state). It is also found that longer type-II NRs exhibit larger $\Delta I / I$ than shorter NRs. Both types of particles exhibit larger $\Delta I / I$ sensitivity for larger k_t values (lower QY). This is because, $\Delta I / I$ displays a large sensitivity to changes in $\underline{\tau_r}$ (for a given $\underline{\tau_{nr}}$) at low quantum yields (Fig. 4.4c, f, i),

The QCSE can be detected not only by recording a decrease or an increase in the sensor's (total) fluorescence intensity, but also through a direct measurement of the spectral shift of the sensor's emission spectrum. This latter approach provides a higher sensitivity measurement[68]. The spectral shift can be measured by recording the emission spectrum as function of voltage and extracting the peak position of the spectra by fitting[68]. Alternatively, the shift can be detected by splitting the emission into two halves (using a dichroic mirror) and detecting them with two (or split) detectors. Spectral shifts are thus translated into anti-correlated intensity changes between the two detected signals. The ratio of the two signals (denoted here as ΔI_{ratio}) directly reports the spectral shift, and is more immune to noise (and blinking) as compared to a simple intensity measurement[89].

The QCSE results in both a spectral shift $\Delta\lambda$ and a spectral broadening $\Delta FWHM_{\mathrm{V}}$. To estimate the dependence of ΔI_{ratio} on $\Delta\lambda$, I reanalyzed our previously published QCSE data taken for 275 individual ZnSe-CdS NRs[68]. This data set lacks a voltage calibration. However, due to a distribution of NRs orientations with respect to the field direction, the data set exhibits distributions of Stark shifts and spectral broadenings. Fig. 4.5a shows a scatter plot of normalized spectral broadenings $\gamma_{FWHM} = \Delta FWHM_{\mathrm{V}} / \Delta FWHM_{\mathrm{V=0}}$ ($\Delta FWHM_{\mathrm{V=0}}$ is the zero field spectral width value) as function of spectral shifts $\Delta\lambda$ for the whole data set. From this scatter plot I derive, by linear regression, the relation: $\gamma_{FWHM}\left(\Delta\lambda\right) = 1 + 0.022 \times \Delta\lambda$. When the spectrum is red-shifted, $\Delta FWHM_{\mathrm{V}}$ is increased. When the spectrum is blue-shifted, $\Delta FWHM_{\mathrm{V}}$ is decreased. Based on the average spectra at zero field, the unperturbed sensor's emission spectrum can be modeled by a Lorentzian curve:

$$L(\lambda) = \frac{30\ \mathrm{nm}}{2\pi\left[\left(\lambda - 600\ \mathrm{nm}\right)^2 + \left(30\ \mathrm{nm}/2\right)^2\right]}$$

with $\Delta FWHM_{\mathrm{V=0}} = 30\ \mathrm{nm}$, and $\lambda_{\mathrm{V=0}} = 600\ \mathrm{nm}$ (average peak emission wavelength at zero field). This average model spectrum is shown as a red curve in the inset of Fig. 4.5b. Under an applied field, this spectrum is altered according to:

$$L(\lambda, \Delta\lambda) = \frac{30\ \mathrm{nm} \times \gamma_{FWHM}\left(\Delta\lambda\right)}{2\pi\left[\left(\lambda - 600\ \mathrm{nm}\ \text{-}\ \Delta\lambda\right)^2 + \left(30\ \mathrm{nm} \times \gamma_{FWHM}\left(\Delta\lambda\right)/2\right)^2\right]}.$$

Then, ratiometric observable I_R / I_B from $L(\lambda, \Delta\lambda)$ is estimated as

$$I_R / I_B\left(\lambda, \Delta\lambda\right) = \frac{\int_{600\ \mathrm{nm}}^{\infty} L\left(\lambda, \Delta\lambda\right) d\lambda}{\int_{-\infty}^{600\ \mathrm{nm}} L\left(\lambda, \Delta\lambda\right) d\lambda}$$

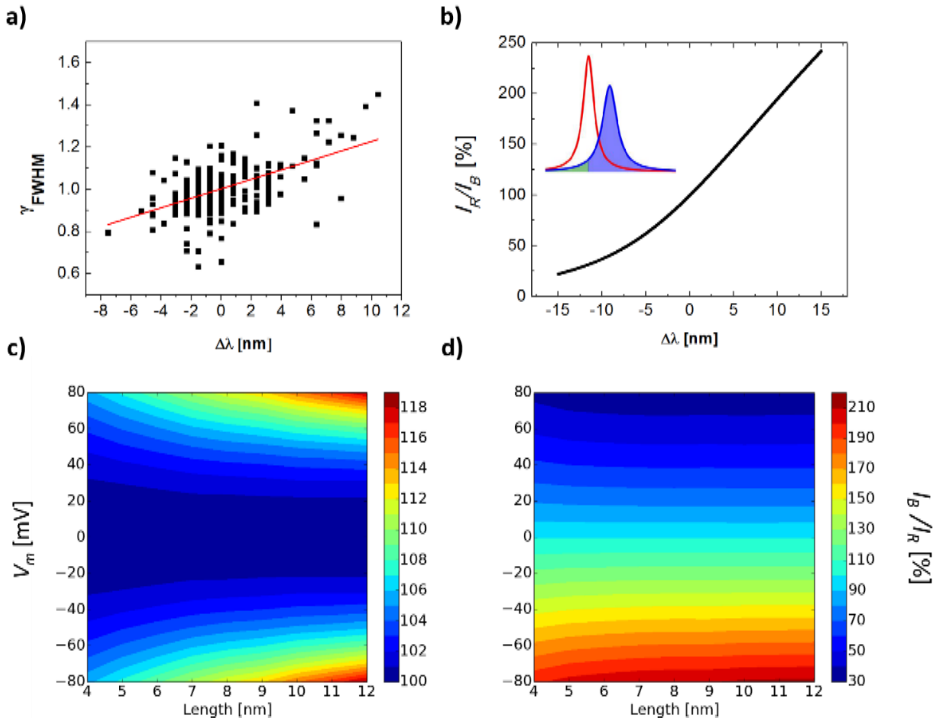

Fig. 4.5: (**a**) A scatter plot of normalized spectral widths γ_{FWHM} as function of Stark shifts $\Delta\lambda$ for 275 ZnSe-CdS NRs. (**b**) The ratiometric observable I_R/I_B as function of the Stark shift $\Delta\lambda$ Inset: Lorentzian fits to average spectrum (red) and red shifted spectrum (blue/green) (**c**, **d**) I_R/I_B of CdSe (**c**) and ZnSe-CdS(**d**) at different length and V_m referenced to V_m=0.

As shown in Fig. 4.5b, I_R/I_B changes from 22 % to +242% when the spectrum is shifted from -15 nm to +15 nm. For a 4 nm type-I CdSe NRs, I_R/I_B increases by approximately 4 % when V_m changes from -70 mV to 0 mV. For a 12 nm type-I CdSe NRs, I_R/I_B increases by 12 % for the same voltage sweep. I_R/I_B of a 4 nm type-II ZnSe-CdS heterostructure NR reduces by 67 % (for a blue-shifting orientation) or increases by 247 % (for a red-shifting orientation) when the membrane voltage is swept from -70 mV to +40 mV. I_R/I_B is only weekly dependent on the length of these type-II NRs.). For a 12nm ZnSe-CdS NR, I_R / I_B reduces by 70 % (for a blue-shifting orientation) and increases by 295 % (for a red-shifting orientation) for same voltage sweep (Fig. 4.5d).

4.6 Discussion

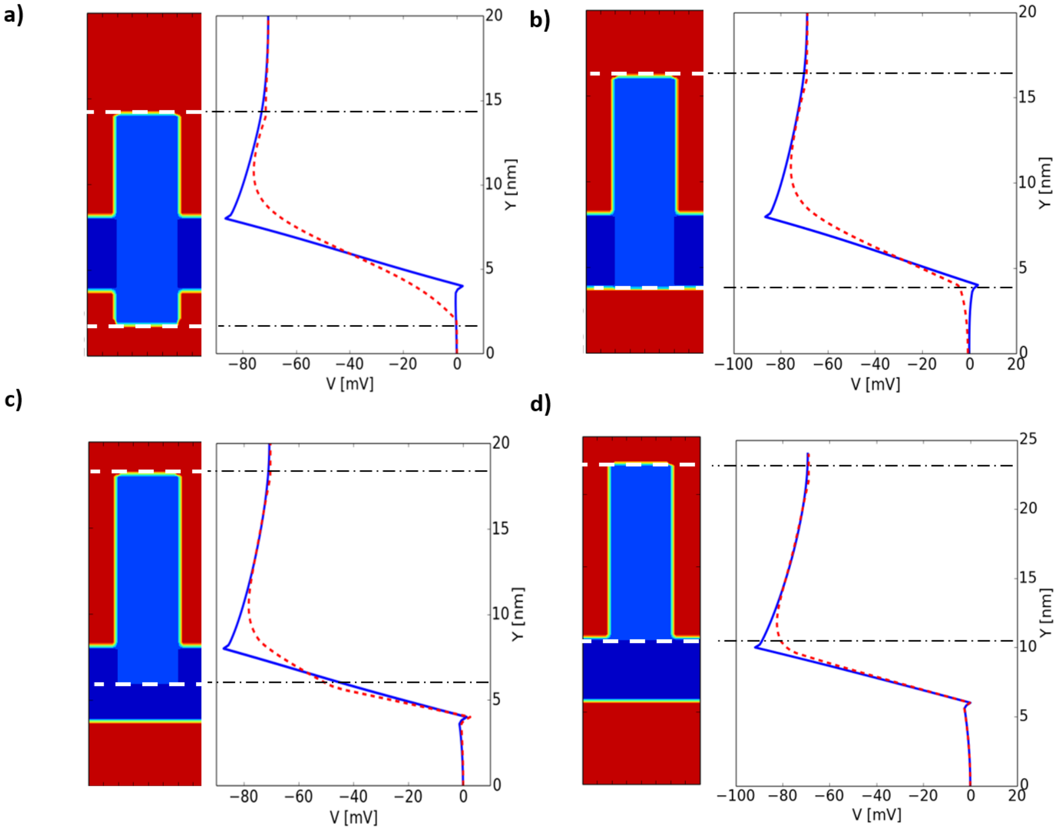

Fig. 4.6 Non-ideal case of NRs insertion in membrane. Color represents different material's dielectric constants ε_r : intra- and extra-cellular (red): 80, lipid (dark blue): 4, NR (light blue) 10. ε_r 's at the boundaries and interfaces are averaged. Distance from NR's bottom end to the bottom lipid's head group is 2nm (**a**), 0nm (**b**), -2nm (**c**), -4nm (**d**). Right graphs are 1D potential profile across the NR (dashed red line) and outside of the NR (solid blue line) when V_m=70mV. Dashed-doted black lines mark the top and bottom of the NR.

Effective action potential recording *via* the QCSE requires the NRs to be inserted in the correct orientation into the cell membrane (Figs. 4.1). I also calculated electrostatic potential for non-ideal cases, where NRs are partially embedded into the membrane (Fig. 4.6). These calculations suggest that F_{int} is concentrated in the membrane embedded part of the NR when it asymmetrically extrueds out of the membrane. In this case most of the membrane potential drops outside of the NR and the linear approximation $F_{\text{int}} = \Delta V / l = V_m / l$ is not valid anymore. For a given V_m, QCSE will be maximized when both ends of the NR symmetrically extrued the membrane on both sides.

While best performing voltage sensitive dyes exhibit $\Delta I / I \approx 20\%$, 4nm type-II QDs are predicted to exhibit $\Delta I / I \propto 30\%$ [91]. Our calculations suggest that 12 nm long type-I CdSe NRs and ~12 nm long type-II ZnSe-CdS heterostructure NRs could potentially exhibit $\Delta I / I \approx 40,\ 250\%$ increment, respectively or 75 % reduction for type-II NR. $\Delta I / I$ relies on f, so the longer is the more sensitive for both samples since longer (or larger) volume has enough room for wavefunction's relocation.

The ratiometric observable I_R / I_B (based on $\Delta\lambda$ spectral shift) provides higher noise-immunity and higher sensitivity measurement as compared to the intensity-based $\Delta I / I$ measurement, especially for short, weakly excited NRs (most of the emission is from X state). While $\Delta I / I$ of a 4nm type-I CdSe NR in the X state is hardly $\Delta I / I$ ~1%, the ratiometric measurement provides I_R / I_B ~4 %. The largest $\Delta I / I$ signal for this particle approaches 40 % but it sacrifices the brightness (Fig 5c). However, the ratiometric measurement provides I_R / I_B ~13% (Fig. 4.5c). Unlike the single channel intensity measurement, (Fig. 4.4) where length plays important role, ratiometric measurement is rather length insensitive especially for type-II NR. For this sample, I_R / I_B is either decreased by at least 67 % or increased by 240%. If employing this measurement, it is unnecessary to elongate the NR for obtaining larger sensitivity. I anticipate that shorter NRs are easier to be inserted in the membrane.

The calculations show that the fluorescence lifetime of the sensor is strongly modulated by the membrane voltage and therefore a fluorescence lifetime measurement by time correlated single photon counting (TCSPC)[96] and [97] could also serve as a noise-immune voltage sensing observable.

In general, longer NRs exhibit larger $\Delta\lambda$, $\Delta\tau_r / \tau_r$, $\Delta I / I$ and I_R / I_B and are therefore more sensitive to voltage changes than short NRs. However, stably inserting long NRs into the membrane, with both ends symmetrically extruding the membrane on both sides is a very challenging task. It requires anisotropic functionalization that imparts membrane protein-like properties to the NRs. Several recent works report on the intimate association of QDs with cell membranes[98] and vesicles[99]. In Chapter 5, membrane inserted NRs with the desired orientation is introduced. Nonetheless, short NRs (4nm) exhibit reasonable voltage sensitivity and therefore should be pursued as an alternative approach.

Lastly, random orientation of membrane-inserted asymmetric (type-II) sensors could result in the cancelation of the (ensemble level) voltage signal due to opposite sign spectral shifts (or intensity changes). Methods for directional insertions that ensure same orientation for all will need to be developed. Note that if such sensors are bright enough to operate on the single particle level (dilute limit), this problem is aliveated as there is no cancelation of the signal.

4.7 Summary

Sequential Schrödinger-Poisson calculations were used to assess the voltage sensing performance of type-I CdSe NRs and type-II ZnSe-CdS heterostructure NRs embeded in a membrane. The calculations show that type-I CdSe NRs could exhibit a sizeable $\Delta I/I$ (due to a voltage-dependent decrease in QY^{X} and QY^{X+}). The calculations also show that type-II ZnSe-CdS heterostructure NRs exhibit sizeable $\Delta I/I$, $\Delta\lambda$, and ΔI_{ratio} with even higher voltage sensitivities. Lastly, the calculations show that a fluorescence lifetime measurement ($\Delta\tau_r/\tau_r$) could also be a sensitive reporter of voltage (due to large voltage-dependent changes in k_r and k_A, for both types of NRs).

When compared with conventional VSDs and VSPs, vsNRs are brighter, they exhibit higher voltage sensitivity and faster temporal response, they hardly photobleach, and they afford noise-immune ratiometric analysis. Our calculatiuons suggest that these sensors could possibly be used on the single molecule level (if bright enough) and provide design rules for their further. Approaches for functionalization and stable membrane insertion of these sensors are currently being developed.

Chapter 5

Membrane potential imaging with semiconductor nanoparticle

5. 1 Introduction

Previous Chapters validate QDs or NRs voltage or electric field sensing capability both experimentally and theoretically (Chapter 2 and 3). In addition, Chapter 4 predicts the realistic performance of membrane inserted NRs in action potential condition and provides design rules. Those results anticipate NPs as promising optical voltage reporters. Meanwhile, NP's delivery method is thoroughly investigated and introduced in this chapter. In addition, delivered NPs successfully record cell membrane potential and is imaged by charge coupled device for the first time.

Although numerous papers discussed diverse NP surface functionalization methods including polymer[100] and peptide[101] coating or additional capping layer[12], they focused on targeting NPs to protein[102, 103], antibody[104] or penetrating into the cell[105]. No surface functionalization attempt has been made to deliver and insert NPs into cellular lipid bilayer up to authors' knowledge. On the other hand, vesicle-incorporated QDs were successfully delivered to the vesicle's lipid bilayer. To achieve this, QD's vesicle insertion and vesicle fusion to the cell should be achieved sequentially. There are few studies demonstrating QD's insertion in the vesicles. Al-Jamal et al. reported the QD's incorporation in vesicles and delivery to the cytoplasm of human epithelial ling cell[106]. Wi et al. both experimentally and theoretically investigate the maximum allowed size of QD which can be inserted in the vesicle[107]. Jeremish (Nadeau) et al. reported the TEM micrographic evidence of QD insertion in a vesicle[99]. Meanwhile, there are specific types of lipids whose vesicle can fuse to the cell membrane. Well known lipids are cationic lipids such as 1,2-stearoyl-3-trimethylammonium-propane, 3ß-[N-(N',N'-dimethylaminoethane)-carbamoyl]cholesterol hydrochloride, and 'cone'- shaped lipid, 1,2-dioleoyl-sn-glycero-3-phosphoethanolamine or its combination[108, 109]. Gopalakrishnan et al. combined these two steps, and successfully deliver QDs to the HEK293 cell membrane which shows no internalization[98]. However, our approach is different from those studies in following aspects.

First, it aims NP's direct delivery without vesicle fusion process to eliminate the redundancy. Second, it overcomes the size and shape limitation on NPs. Until now, only small sized QDs (< 3 nm) are delivered to the two leaflets of vesicles[107]. In contrast, our method was considered and designed for the NR delivery although it turns out that both our method works for both QDs and NRs. Since NRs possess larger voltage sensitivity. Since NRs possess larger QCSE than QDs (Chapter 2 and 4), so NRs will have higher voltage sensitivity.

First half of this Chapter will discuss QDs and NRs cell delivery methods. Rationally designed alpha helical peptide is used to modify NPs' surface. The designed peptides are successfully coated on QDs and NRs and delivered them to the membrane. Second half of this Chapter will cover NPs' diverse membrane potential measurements, validation of voltage sensitivity and analyze the performance. All optical voltage sensing measurement was performed on voltage oscillating engineered HEK cell,[110] which has slow time course, making it suitable for testing pcNP's voltage report.

5.2 NP's surface modification and membrane delivery

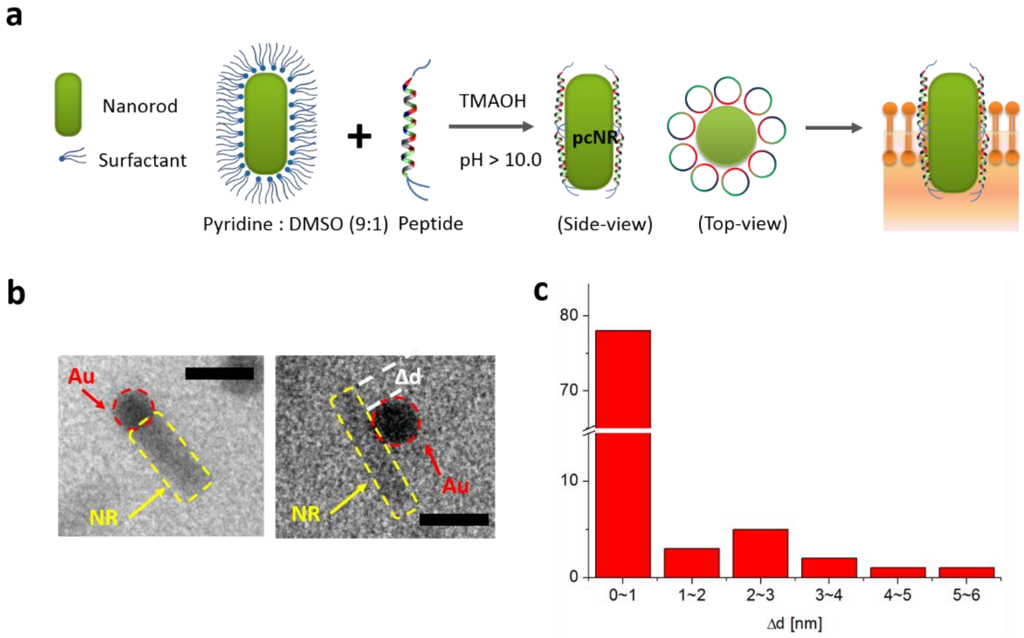

Fig. 5.1 Peptide-coated NR **(a)** Protocol **(b)** TEM micrograph of biotinlated-GNP and pcNR complex, linked *via* NeutrAvidin. Scale bar is 10 nm. **(c)** Histogram of relative GNP position (Δd), measured from the pcNR's end

Fig. 5.1 describes the protocol of the peptide coating on a NR, and peptides' relative orientation with respect to the NR's long axis. Since as-synthesized QDs and NRs are not compatible with cytosolic fluid due to the hydrophobic ligand on their surface, they require an additional surface functionalization step, such as performing ligand exchange[111] or adding additional coating layers[112] before the aqueous phase[113]. For this purpose, novel functionalization technique is developed for NRs' membrane insertion. Inspired by transmembrane protein[114], α-helical peptides, Myristoyl-CLTCALTCMECTLKCWYKRGCRGCG-COOH, and Biotin-CLTCALTCMECTLKCWYKRGCRGCG-COOH, were designed. The only different between two peptides is at their terminal. Biotin-end peptides are used for validating peptides orientation and Myristoyl-end peptides are used for all other experiments. Both peptides consist of three components: liphophilic central part containing multiple cysteines along one face (bind to cations of NPs), hydrophobic residues at the opposite face (heading to the alkyl chain of lipids), and hydrophilic N- and C-termini (exposed to the extra- and intracellular fluid). Through the process of surfactant exchange, ~8~12 peptides will be self-assembled and coated to the QD's or NR's cylinderical wall along its long axis (Fig. 5.1a). The detail procedure of the peptide coating on NRs is shown in Material and Methods (Chapter 5.6).

Hybridization with gold nanoparticle (GNP) confirms peptides' orientation relative to the NR's long axis (Fig. 5.1b and c). The biotin-end peptide is coated on NRs. By adding NeutrAvidin and biotinlated-GNP, I achieved GNP-pcNR complex (Chapter 5.6). Since GNPs are linked to the biotinlated peptide *via* NeutrAvidin, I estimate the relative peptide orientation by observing GNP position with respect to the NR. Under transmission electron microscopy (TEM) examination, larger than 85% of GNP-pcNR complexes displayed GNPs at the or near the NRs' tip (Fig. 1c), confirming the presumed peptide orientation in Fig. 5.1a. This functionalization allowed us to demonstrate stable membrane insertion of peptide-coated NRs (pcNRs) into lipid vesicles or cell membranes. For all other experiments, Myristoyl-end peptide is used for NRs coating.

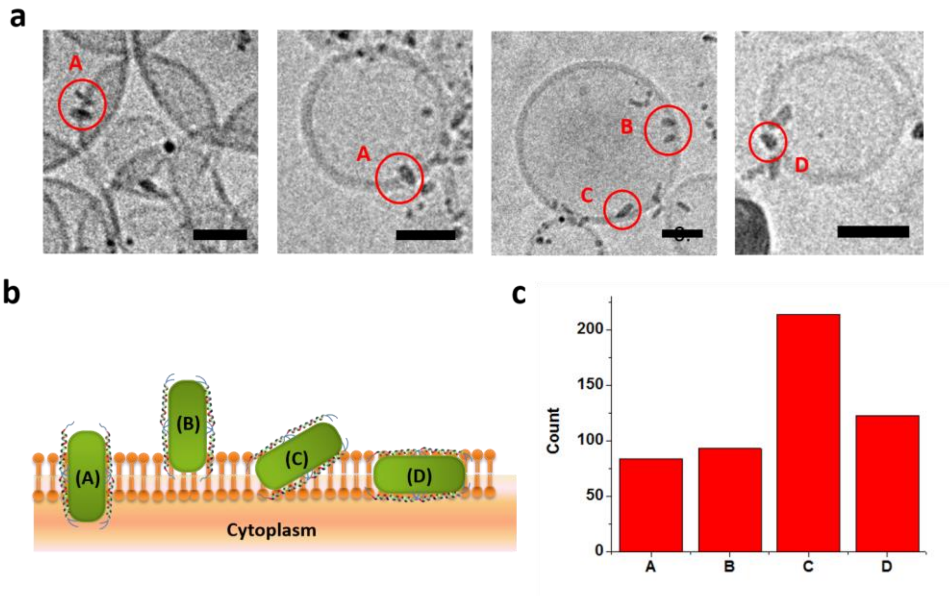

Fig. 5.2 **(a)** Schematic of the pcNR's possible insertion or attachment to the lipid bilayer. (A) Perfectly inserted (B) Partially inserted (C) Insertion with angle (D) Embedded in the membrane **(b)** TEM micrographs of pcNRs inserted vesicles. (scale bar is 30 nm) **(c)** Histogram of A~D configurations, illustrated in **(b)**

Next, pcNR's orientation with respect to the lipid membrane was examined by cryo-electron microscopy (cryoEM) micrographs. pcNRs are delivered to the small unilamellar vesicles (SUV) which are first sonicated then extruded with 100 nm pore filter (Chapter 5.6). pcNRs' spontaneous insertion in vesicles are confirmed by fluorescence microscopy measurement (Fig. 5.3a). Since the cryoEM image is top-view (integrated over z), exact z-levels of pcNRs and how they insert are unclear except for those, adjacent to the equator. Therefore, pcNRs adjacent to the equator are considered in our analysis and categorized into four different types of configurations (Fig. 5.2b). A-type is pcNR's perfect and symmetrical insertion (NR's both ends are exposed to outside of the membrane). B-type is either pcNR's partial but perpendicular insertion (one side of NRs is exposed) at the equator or A-type insertion in different z-level. C-type is pcNR's partial insertion with an angle. D-type is embedded pcNRs in the lipid bilayer. More than 500 cases are categorized and histogrammed (Fig. 5.2c). 16.4 % of NRs are A-type insertion. A-type is expected to have the largest voltage sensitivity *via* QCSE since it detects the largest voltage drop across pcNRs. B- and C-type attachment count for 18.0 and 41.7 %, respectively. In these cases, electric field applied to the NR is squeezed towards one end (Chapter 4.6) or less voltage drop is applied to pcNRs if partially inserted. Therefore, they are expected to have less voltage sensitivity. Embedded pcNRs (D-type) are also influenced by electric field. Given the same amount of voltage drop in pcNRs, electric field will be different from A and D. Considering the fact that electric field is shielded by lipid molecules. D-type is anticipated to have smaller QCSE[91]. However, this result demonstrates that at least 16.4 % of pcNRs have presumed orientation (Fig. 5.1a or A-type), proving the peptide's functionality. The actual amount of perfectly inserted pcNRs will increase if B-type is taken into account.

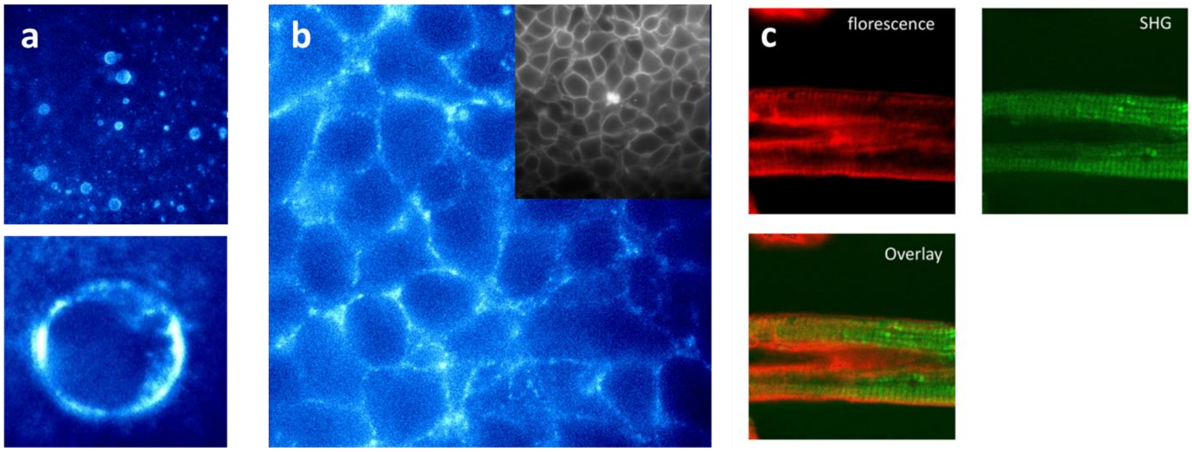

Fig. 5.3 Fluorescence images of pcNRs loaded **(a)** vesicles (bottom: magnified) **(b)** HEK293 cells (inset: staining with ANEPPS). (**c**) Ventricular cardiomyocyte from rabbit. **(a,b)** measured by 20X 0.4 NA objective lens. (**c**) measured by 100X 1.4NA objective lens.

Fig. 5.3 demonstrates the pcNR' labeling applied for diverse system. Besides the pcNR' SUV insertion (Fig. 5.2b), it can also label giant unilamellar vesicles (GUVs, Fig. 5.3a). Fig. 5.3b compares staining images of HEK293 cells with pcNR and ANEPPS (inset). Both show well-defined boundaries of HEK293 cells, which prove the strong cell membrane association of pcNRs. Besides pcNRs, pcQDs also label cell similarly (Fig. 5.4). However, more punctuated fluorescence patterns are visible at the cell boundaries for pcNRs than ANEPPS, due to uneven labeling and strong single pcNR emission. Even single pcNR's blinking behavior is clearly visible. Semiconductor NPs have been developed in such different ways that they can sense pH[28], temperature[32], stress[33], ions[30], and electric field[68]. In addition single NP is individually addressable. Therefore, nanoscale environmental sensor will be achievable with one NP at a single molecule level. Unlike semiconductor NPs, organic dyes or molecules have much smaller (<5 %) absorption cross section[115], making it impossible to detect individual emission. I also succeeded in staining rabbit's ventricular cardiomyocyte with pcNRs (Fig. 5.3c). Since unlabeled pcNRs or nonspecific bound NPs contributes to the background, they decrease the signal to noise ratio (S/N). Since labeled pcNPs are resistant to the multiple washing, the S/N increases with each addition wash (removing floating pcNRs).

5. 3 Membrane potential measurement

Recently developed light-activated voltage oscillating cell lines[110] are used for testing pcQD's and pcNR's voltage sensing capability. These HEK cells are expressed with voltage-gated sodium channel Na_V 1.3 and inward rectifying potassium channel K_{IR} 2.1. The cell's membrane potential oscillates periodically upon light illumination if its confluency reaches 90~100 %. Depending on the culture condition, oscillation frequency varies from 1 Hz to 4 Hz. Its resting potential is -66 ± 5 mV and rises up to +34 ± 12 mV when spike comes[110]. It serves as a convenient test-bench for testing pcNP's voltage sensing capability since it does not require the bulky electrophysiology equipment, and has slow time courses. A half width of spikes of this cell is larger than 100 ms whereas that of action potential in neurons is less than 1 ms.

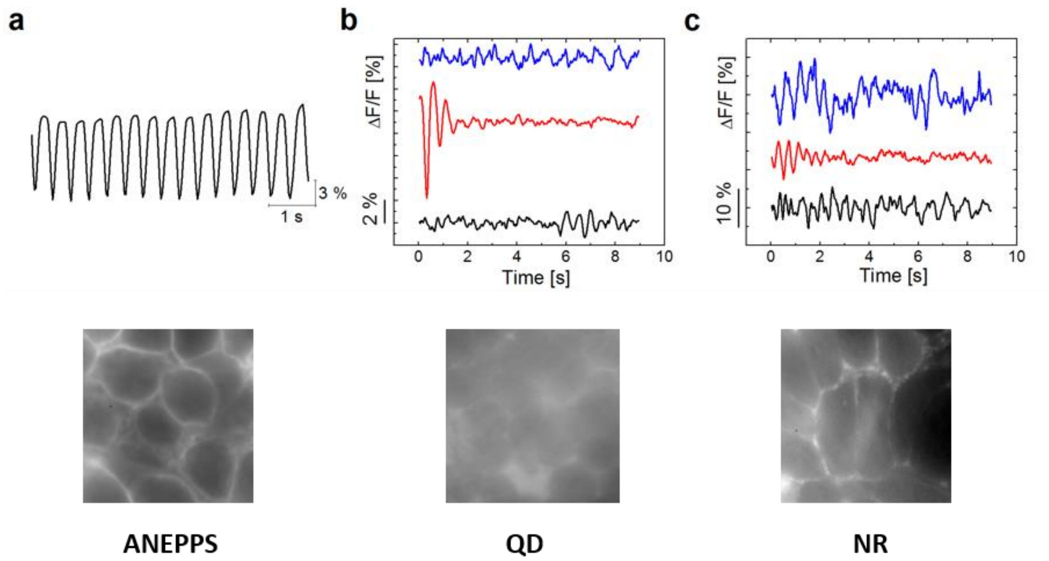

Fig. 5.4 Intensity traces of spikes, measured by (**a**) di-8-ANEPPS and (**b**) pcQD (**c**) pcNR

I first test the cell's voltage oscillating property with commercial VSD, di-8-ANEPPS (ANEPPS) as a control (Fig. 5.4a). It exhibits well-defined periodic voltage oscillation (f= 2 Hz), showing at around 10% sensitivity (ΔF/F). By performing multiple experiments, reproducible voltage oscillating activity was confirmed. Thus, the magnitude of ANEPPS's fluorescence change (10 % / 100 mV) and frequency (1.5~ 4 Hz) of spikes serves as a positive control for pcQD and pcNR measurements. Next, I applied pcQDs and pcNRs to more than 40 cell-cultured dishes and measured their fluorescence. Three representative fluorescence intensity trajectories of pcQD and pcNR are reported in Fig. 5.4b (pcQD) and 5.4c (pcNR). Compared to the ANEPPS, pcNPs' intensity traces are irregular such that there are random occurrences of voltage reporting period and non-reporting period (reds in Fig. 5.4b and c). Its amplitude (red and black in Fig. 5.4b, blue and red in Fig. 5.4c) and frequency also varies (black in Fig. 5.4c). In many cases, voltage reporting period (and ΔF/F) disappears and settles in voltage non-reporting period within 20 seconds. For this reason, I extract and statistically analyze the maximum value of sensitivity ($\Delta F/F_{max}$) of each measurement. For pcQDs, the mean value of $\Delta F/F_{max}$s is 3.0 % and the standard deviation (σ) of $\Delta F/F_{max}$ is 2.8 %, implying large variation of sensitivity. For pcNRs, mean value of $\Delta F/F_{max}$ is 9.5 % and σ is 4.1 %. Compared to the ANEPPS image at the bottom of Fig. 5.4, pcNPs have less S/N, due to non-specific binding and unbound pcNPs floating in the medium.

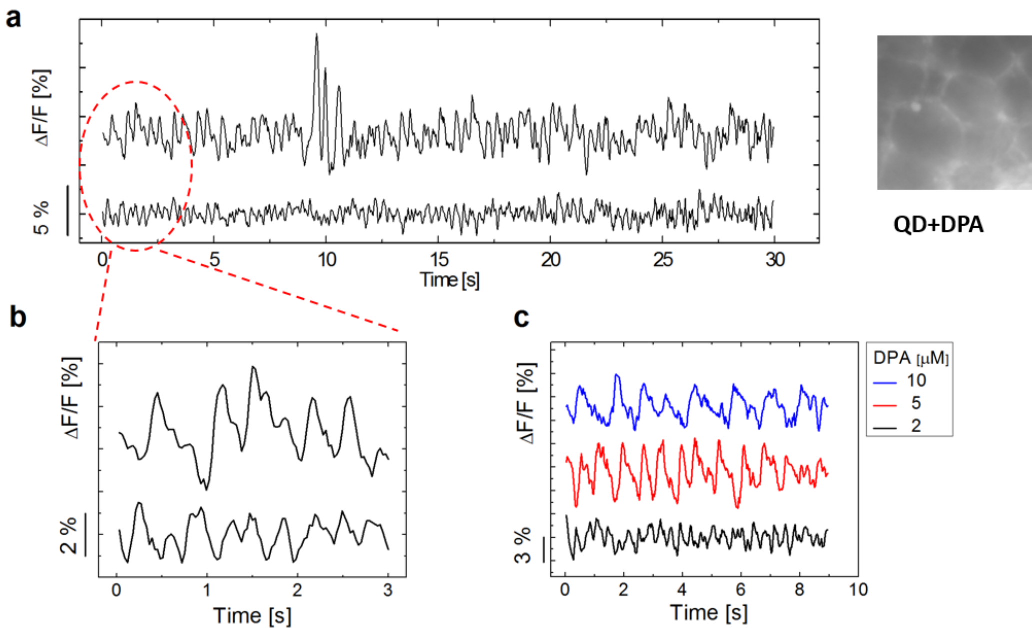

Fig. 5.5 Spiking measurement with pcQD and DPA (**a**) Two representative recordings with 2μM DPA with pcQD (**b**) Magnification of 0~3s of (**a**). (**c**) pcQD with different DPA concentration. 2μM (black), 5μM (red), 10μM (blue)

Unstable voltage reporting is stabilized by introducing a dipicrylamine (DPA) molecule which serves as a foster resonance energy transfer (FRET) acceptor, quenching the donor fluorescence (Here, pcQD is donor). Since DPA is negatively charged, its partitioning in the membrane is determined by the membrane potential[7]. If pcQDs are in B- or C-type insertion as shown in Fig. 5.2b, it's expected to have membrane potential-modulated FRET interaction between DPA and pcQD. Fig. 5.5a shows two intensity trajectories of this FRET measurement (pcQD and 2μM of DPA on HEK cell). Compared to the pcQD only measurement, where spiking reporting is unstable (Fig. 5.4b and c), FRET measurement displays much more stable spiking reporting (Fig. 5.5). For some dishes, there are still voltage reporting intermittency and sensitivity change during FRET measurement, which are regarded as unevenly distributed DPAs. However, it allows the extended voltage-reporting time stably. None of the pcQD and pcNR dish measurements report voltage oscillation more than 30 seconds stably. In one experiment in Fig. 5.5a, there is a burst of spiking in which ΔF/ F reaches 10 %, surpassing the rest of the spikes (around 3.0 % in ΔF/ F). This implies that there is a transient movement of pcQD which opens or changes to another voltage sensing channel or just increases the FRET sensitivity by its proximity to the DPA molecule. The largest ΔF/F of FRET measurement is 6.9 %, but the majority shows less than 2 % ΔF/F. In contrast to the pcNP only measurement, washing does not deteriorate the voltage reporting property for FRET measurement. Instead, it increases ΔF/F by reducing background fluorescence. In conclusion, washing is always beneficial before FRET experiment.

Previously reported, slowed and increased width of spikes are also confirmed in this study. Bradley et al. found this phenomenon with DiO/DPA FRET measurement and explained it with increased capacitance by DPA molecule[7]. Here, 2 (black), 5(red) and 10μM (blue) of DPA at the final concentration with 2 μl of pcQDs are loaded to three different dishes. Fig. 5.5c shows their intensity traces, displaying slower, more asymmetric and broadened spikes as DPA concentration increases. The frequencies are 2.2, 1.6, 1.0 Hz, and the average half widths are 0.23, 0.30, 0.49s for 2, 5 and 10 μM of DPA, respectively. It is also observed that falling phase is slower than rising phase as DPA increases. These solid FRET features suggest pcQD's relative position to the cell membrane (B or C-type), and prove the possible replacement in hybrid voltage sensors such as DiO/DPA or eGFP/DPA. Considering the difficulty of DiO labeling in the cell membrane[7], pcQD has advantages in fast and easy cell labeling.

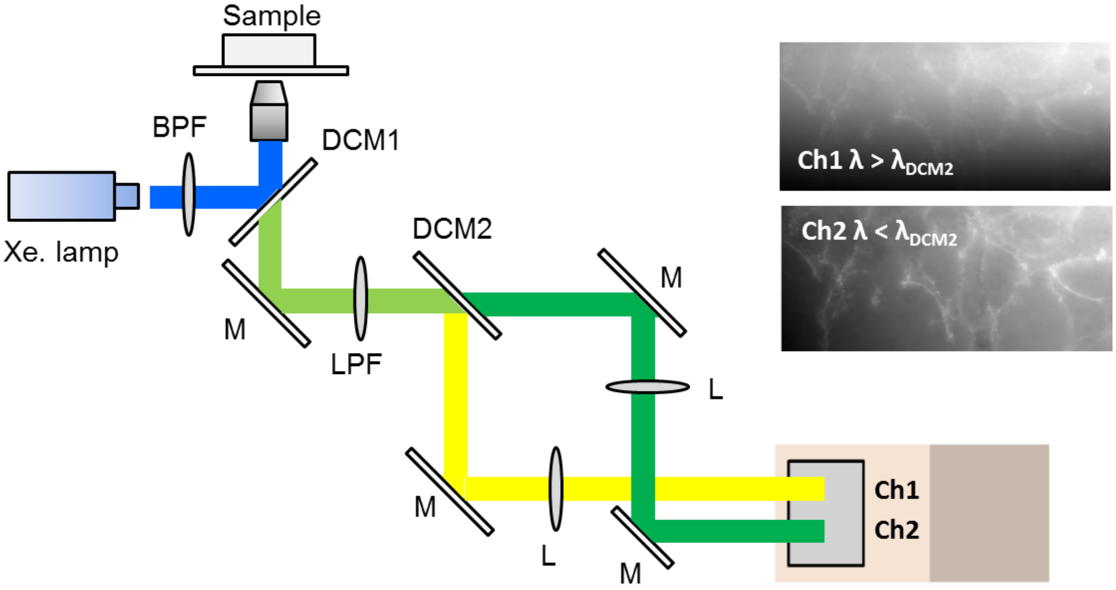

Fig. 5.6 Dual-view optical setup (L=lens, DCM=dicroic mirror, M=mirror, BPF=band pass filter, LPF=long pass filter)

Next, dual-view spectrum separating measurements were performed for two purposes. First, pcQD's voltage sensing is additionally validated with simultaneous measurements with ANEPPS. Second, it helps to understand the voltage sensing mechanism by observing the spectrum shift to determine whether it is QCSE or not. Fig. 5.6 is a schematic of dual-view optical setup. The set-up is built on Olympus IX71 inverted microscope equipped with a Xenon lamp (Olympus, U-LH75XEAPO, 75W) and excitation filter (BPF 470/40, Chorma Technology Corp, Bellows Falls, VT). The emission of the NP is collected by ×60 objective lens (Olympus, PlanApo 60×, n=1.45, oil immersion), passed through a dichroic mirror (DCM1, 505DCXRU, Chorma Technology Corp, Bellows Falls, VT) and directed to the dual-view path. DCM2 separates the emission spectrum, and separated spectra are imaged at the Andor iXon electron multiply (EM) charge coupled device (CCD) camera (EMCCD, Andor iXon, South Windsor, CT).

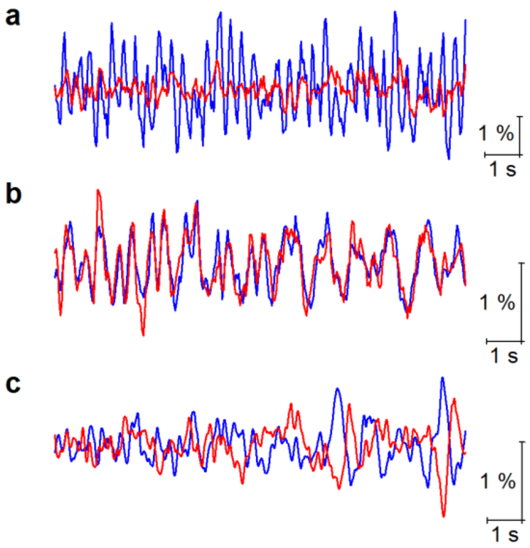

Fig. 5.7 Dual-view experiment

For validation, I measured pcQD (λ=511nm) and ANEPPS (λ=630nm) simultaneously with 570nm long pass DCM for DCM2. Their images are found in ch1 (blue, ANEPPS) and ch2 (red, pcQD) (Fig. 5.7a). By comparing spikes' peak positions of two traces, it is clear that pcQD signal is correlated with ANEPPS, proving its voltage sensing validity. Next, I separate the bluer (λ < 514nm) and the redder (λ > 514nm) spectrum of pcQDs' emission by 514 nm long pass DCM for DCM2. If the voltage sensing mechanism is QCSE (spectrum shift), intensities of bluer and redder channels will be anticorrelated. If it is correlated, it indicates no QCSE. It also indicates pcNP's close proximity to the membrane close enough to sense the potential or ion change in its environment. In most cases, correlated signals are detected as shown in Fig. 5.7b. However, a few cases show occasionally anti-correlated signal between redder and bluer channel (Fig. 5.7c, noticeable in late 5 seconds). This is the strong evidence of QCSE, and membrane insertion. Shifted spectrum in Fig. 5c turns out to be 1nm, which is calculated by applying the calibration curve in Fig. 4.5.

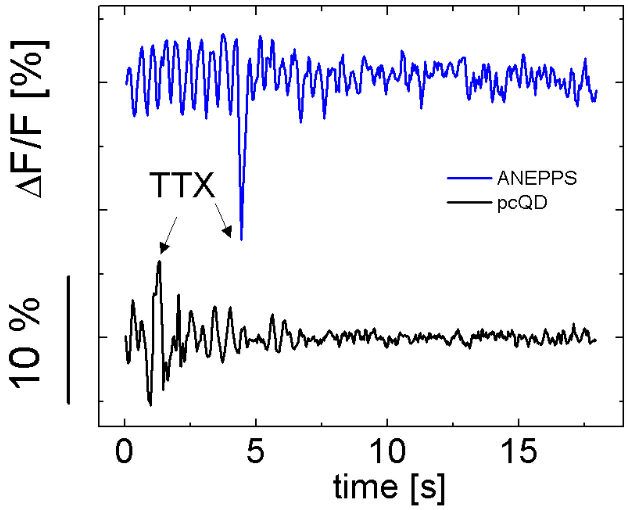

Fig. 5.8 TTX induced Na_V 1.3 block

Tetrodotoxin (TTX) is frequently used for studying sodium channel in neuroscience or in physiology. It blocks sodium channels, prohibiting action potential in neurons[116]. In this study, TTX is used to confirm whether pcNP's voltage sensitivity originates from the dynamical potential change due to the ions movement during the voltage oscillation or just artifact. As a control experiment, ANEPPS is used (blue in Fig. 5.8). Before loading TTX, it reports stable voltage oscillation. After loading, ΔF/F diminishes and merges in noise level in 5 seconds. Similarly, ΔF/F of pcQD signal is nullified in 5~6 seconds after loading TTX.

Simultaneous and multisite voltage imaging is shown in Fig. 5.9. Averaged intensity of cells' boundary, noted as white in Fig. 5.9b is first analyzed to check whether it captures real voltage dependent emission change or just artifact. White areas indicating cells' boundary in Fig. 5.9b are obtained by applying threshold in intensity over entire field of view in Fig. 5.9a. The averaged intensity is presented in Fig. 5.9c which shows periodic oscillation. Fig. 5.9d shows the cross correlation between two points (red, and green in Fig. 5.9a), demonstrating also periodic oscillation with 3.5 Hz. These average data (Fig. 5.9c) and cross correlation (Fig. 5.9d) proved the membrane potential dependent intensity change since if captured signal is noise and different points are uncorrelated, it would not generate the periodicity as in Fig. 5.9c and d. Next, data analysis on individual and separated points are performed in Fig. (5.9e~h). In our field of view (Fig. 5.9a), three cells are selected for comparing between adjacent cells (red and blue families), and remote cell (green family from red and blue families). In each cell, three different sites are also selected and compared (Fig. 5.9e, f and g). QD has emission intermittency (blinking) whose trajectory serves as envelop function in intensity trajectory and voltage dependent oscillation feature is added on top of that, serving similarly as carrier frequency. Therefore, QDs in the same cell present a bit different ΔF/F, due to the different envelop function. In addition, it is also possible that each QD suffers different electric environment in nanoscale range near each QD.

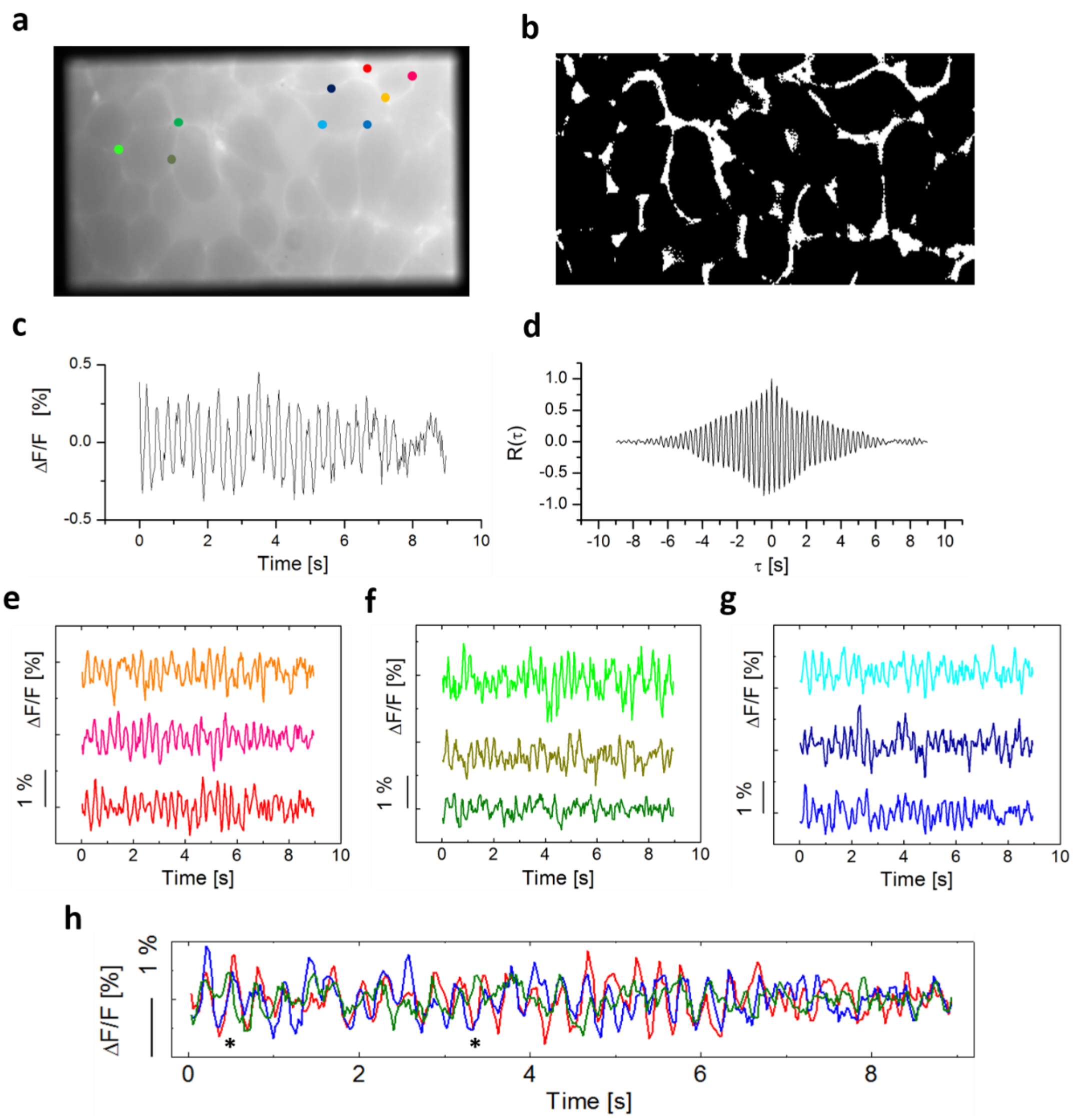

Fig. 5.9 Simultaneous multisite voltage imaging with pcQD (**a**) Imaged field of view. (**b**) Boundary selection of (**a**), noted as white. (**c**) Averaged intensity trace of cell boundary in (**b**, white), (**d**) Cross correlation of red and green position in (**a**). (**e~g**) Intensity traces at different points. Colored dots in (**a**) correspond to same colored curves in (**e~g**). (**h**) Comparison between three points at red (**e**) and green (**f**) and blue (**g**)

Fig. 5.9h compares three different cells (the bottom curves in Fig. 5.9e, f, g). By comparing so, it is determined that the green cell's oscillation is ahead of red and blue cells at certain times, marked with asterisks (* in Fig. 5.9h). This result demonstrates pcQD's voltage imaging, enabling high throughput simultaneous multisite recording.

5. 4 Discussion

This study first introduces the inorganic voltage sensor, made of semiconductor nanocrystals. Organic dyes have flourished in the past few decades. Recently hybrid voltage sensor (DiO/DPA, eFGP/DPA)[7, 90], photoinduced electron transfer (PeT)[117], and voltage sensing protein such as microbial rhodopsin (ArCh)[8] have been introduced are overcoming some of the VSD's limit. The recently developed organic voltage sensors have larger ΔF/F (> 20 %) than conventional VSD (~10 %). However, they have slower response (hybrid voltage sensor), lower quantum yield (Arch), short retention time (internalization) or are toxic. Compared to these organic voltage sensor, inorganic NPs are quite different in shape, size, and physical and chemical property. Due to the recent achievement for colloidal nanocrystal synthesis[10], diverse magnetic[118], plasmonic[119], semiconductor NPs[11] are introduced and used for many applications including biology[13] as well. However, their bulkiness (> 4 nm), and incompatibility with cytosolic fluid and membrane delivery make them difficult to use in the field of neuroscience.

I solve this problem by using alpha helical peptides that attach to the NP surface in parallel to the NR cylinder. Although this peptide is the first of its kind, it successfully and surprisingly directs pcNPs to the cell membrane. Considerable amount of pcNRs are inserted in vesicle membrane in the desired orientation (Fig. 5.2). If it is an A-type insertion, 40 % and 280

% ΔF/F increase are expected for 12 nm CdSe and ZnSe-CdS NR under action potential, respectively (Chapter 4). Further optimization of the peptide sequence will enable more A-type insertion. By applying the same concept (peptide coating), magnetic or plasmonic NPs delivery will be feasible. Therefore, one direction of future study should focus on precise tuning of peptide sequence, length, shape of NPs and delivery optimization for different NPs.

If delivery is equipped, semiconductor NPs possess lots of advantages over VSDs as voltage sensors. First of all, voltage sensitivity *via* QCSE or electrochromic effect (corresponding QCSE for organic molecule) is much larger in NPs than in organic molecules. Furthermore, it is further enhanced by adopting type-II energy structure such as ZnSe-CdS or CdSe-CdTe. The large spectral shift enables the ratiometric intensity measurement (Fig. 5.7c) which is noise immune[89]. Secondly, semiconductor NPs are very strong emitter, affording single-molecule detection due to a large one-photon excitation cross-section and high quantum yield[115]. Thirdly, voltage detecting with QCSE provides the fastest response among all other mechanism. For example, Ca^{2+} indicator cannot capture single action potential among action potential trains due to the saturation of this ions in the cytoplasm. Lastly, its tunable spectrum with large Stokes shift expands the choice of light sources, provides the multiplexing and near infrared range which is more suitable for *in-vivo* experiment.

Current voltage reporting of pcNPs are yet mature in terms of sensitivity and reporting time (Fig. 5.3). Possible explanation for voltage reporting intermittency (Fig. 5.4 and ΔF/F burst in Fig. 5.5) is transient movement of the pcNPs in- and out- the membrane. Another explanation is the increasing capacitance due to pcNP iteself. For some intensity traces (Fig. 5.4b blue, Fig. 5.5c black, Fig. 5.7b), spikes' width is increased gradually. The increased capacitance will eventually influence cell's natural oscillation. NPs' relative permittivity is at around 10, compared to 2~4 of lipid molecule. In addition, NPs and peptides may be charged which contributes to the increase of capacitance. Therefore, studies regarding capacitance and potential change induced by membrane inserted pcNPs should be investigated. FRET measurement with DPA molecules provides more information regarding the relative position of pcNR, with respect to the membrane. This green light emitting QD/DPA combination is the third type of hybrid voltage sensor after eGFP/DPA and DiO/DPA. It does not require the protein expression of eGFP or the incubation time for DiO (1~2 days). Spectrum shift is observed by dual-view experiment, indicating QCSE (Fig. 5.7c). 1 nm of spectral shift translates to 8 % I_R/I_B (Fig. 4.5), indicating its highly sensitive measurement of membrane potential. This 1 nm shift of 4 nm sized CdSe QD is precisely estimated by Chapter 4 and ref. [91]. In Chapter 4, 12 nm CdSe and 4~12 nm ZnSe-CdS have 1.5 and ~10 nm $\Delta\lambda$ which translates to 13 and 240 % I_R/I_B, respectively. The NPs used in this study are CdSe and CdSe-CdS, which are not very sensitive voltage sensor due to the strong Coulomb interaction between an electron and a hole which oppose the external electric field (Chapter 2). Therefore, optimized size of ZnSe-CdS should be synthesized in order to increase the sensitivity. ZnSe-CdS sample (#7) used in Chapter 2 is 30 nm long and 10 nm thick.

Although much efforts are still needed to make this inorganic voltage sensor more reliable before practical use in the relevant field, Fig. 5.9 shows its potential to measure high throughput simultaneous multisite recording of membrane potential. In addition to this, novel detecting methods will be available with inorganic voltage sensor. It includes ratiometric intensity measurement (Fig. 5.7), which is noise immune to background fluctuation and blinking, and lifetime change measurement ($\Delta\tau$). Lifetime change is another sensitive indicator for QCSE (Chapter 4). Imaging $\Delta\tau$ can be captured by fluorescence lifetime imaging microscopy (FLIM)[94] or wide-field FLIM using the singe photon counting H33D detector[95].

5.5 Summary

First generation of inorganic voltage sensor is introduced for membrane potential imaging. The sensitivity varies from lower than 0.5 to larger than 20 %. The pcNRs have statistically larger sensitivity than pcQDs. Unstable voltage reporting is stabilized by FRET measurement with adopting DPA molecule. Meanwhile, spectrum shift is also found which supports QCSE operation. Therefore, pcNPs are either attached to the cell surface, sensing ions, voltage and distance from DPA, or inserted in the membrane generating QCSE. Sudden burst of $\Delta F/F$ implies transient movement of pcNPs. To operate QCSE, better NP delivery method should be made. Semiconductor NPs have fast response to an external electric field and are more stable and sensitive than organic fluorophores. As a second generation inorganic voltage sensor, we can expect nanodiamond and metal-semiconductor hybrid (Au-CdSe NR or symmetric Au-CdSe-Au NRs) operating with photoinduced electron transfer. If inorganic voltage sensors are mature, they will revolutionize neuroscience and tools for opto-physiology.

5.6 Supporting Information

Nanoparticle preparation

Chemicals and materials: Cadmium oxide (CdO, 99.99%), tri-n-octylphosphine (TOP, 90%), trioctylphosphine oxide (TOPO, 99% and technical grade 90%), selenium (Se, 99.999%), Sulfur (S, 99.5%) along with all organic solvents were purchased from Sigma-Aldrich and used without any further purification. Hexylphosphonic acid (HPA) and octadecylphosphonic (ODPA) were purchased from PCI Synthesis. QD: CdSe/ZnS core/shell QDs were purchased from Evident-511. NR: CdSe-CdS NRs were used. A 50 ml round bottom flask was loaded with 60 mg (0.5 mmol) CdO, 280 mg ODPA and 3 g TOPO. After degassing under vacuum for 1 hour at 120°C the temperature was raised to 340°C under argon until dissolution of CdO at which point 1.8 ml TOP was injected and temperature was raised to 370°C. A solution containing 58 mg Se in 0.5 ml TOP was swiftly injected and heating mantle was removed until. Final core size had a diameter of about 2.7 nm. A 50 ml round bottom flask was charged with 211 mg (1.6 mmol) CdO, 1 g ODPA, 50 mg HPA and 3.46 g TOPO. The reaction flask was degassed for 3 hours at 130° and then temperature was raised to 340°C under argon until dissolution of CdO at which point 1.8 ml TOP was injected. CdSe seed solution was separated and purified for reaction by mixing with toluene and precipitating with excess methanol 3 times. Seeds (cores) were then re-dissolving in 0.6 ml TOP. The S:TOP precursor solution was prepared by mixing 51mg S (1.6mmol) in 0.6 ml TOP. Temperature was raised to 350°C for injection. The amount of dots used for preparation was 8×10^{-7} moles.

NR functionalization with peptides

The two peptides are Myristoyl-CLTCALTCMECTLKCWYKRGCRGCG-COOH, and Biotin-CLTCALTCMECTLKCWYKRGCRGCG-COOH. Their peptide coating protocols are the same. NP functionalization with alpha helical peptide is similar to the protocol introduced in ref. X except few modifications. As-synthesized NRs were coated with hydrophobic surfactants such as TOPO or TDPA. To replace surfactants with designed peptides, I first purified a NP's surface with multiple (5~6×) ethanol precipitation, and redissolved in pyridine 450 µl. The NP's concentration was 0.1 µM. 4.0 mg of peptides were dissolved in 50 µl of DMSO, and mixed with NRs in DMSO solution. 12ul of tetramethylammonium hydroxide (TMAOH) were added to the solution to increase the pH to 10.0 where peptides bind to the NP surface efficiently. The mixture was centrifuged, and redispersed in 150 µl of DMSO. They are ready to be used to the cells. For vesicle staining or cryoEM experiment, NRs in DMSO solution were finally eluted through a G-25 Sephadex desalting column (Amersham, Piscataway, NJ) and equilibrated with PBS buffer. The pcNRs were stored at 4 ºC unless used in experiments.

GNP-pcNR complex

Biotinylated gold nanocrystals were a gift from Ocean NanoTech. Biotin-end peptides were coated on the CdSe/CdS NRs with the same procedure, stated above. Take 1 µl of above peptide-coated rods solution, mix with 15 µl of neutravidin solution (2mg/ml). Let it sit for 20 min at room temperature. Add 1 µl of 20X diluted biotin-Au to this mixture and let the reaction go for 2 h. Take 2 mcl of the solution on to copper grids and let dry in air.

Synthesis of vesicles and staining with pcNP

1,2-dimyristoyl-sn-glycero-3-phosphocholine (DMPC), 1,2-dioleoyl-3-trimethylammonium propane chloride salt (DOTAP), 3ß-[N-(N',N'-dimethylaminoethane)-carbamoyl]cholesterol hydrochloride (DC-Cholesterol), were purchased from Avanti Polar Lipids, Inc. Chloroform solutions of DOTAP (25 mM, 6 µl), DMPC (10 mM, 6 µl)m and DC-Cholesterol (10mM, 6 µl) were mixed and dried in a vacuum for 4 h in rotor evaporator. The film was then hydrated with 1 ml of 0.1M sucrose containing PBS buffer with pH 6.24 overnight at 37ºC incubator, during which vesicles are spontaneously formed. Vesicles were stored at 4 ºC unless used in experiments (they are stable and useable for about one week). For fluorescence microscopy measurement, 2 µl of vsQDs (eluted through a G-25 Sephadex desalting column) are added to the 10 µl of vesicle solution. They spontaneously and rapidly (~1 min) self-insert into the vesicles' membranes.

Cell culture preparation

HEK293 cells (AATC, VA) were maintained in 1:1 Dulbecco's Modified Eagle Medium and Nutrient Mixture F-12 (Invitrogen, NY) supplemented with 10% fetal bovine serum (FBS; Sigma-Aldrich, MO), 0.6mg/ml of G418 (Life technologies), and 5µg/ml of puromycin (Life technologies). Cells are grown on the 35mm glass bottom dish for the optical experiment purpose until it reaches 90 % confluency.

Di-8-ANEPPS staining

4 μl of Pluoic (10 %) in DMSO was added to the ANEPPS

pcNP staining

1~2 μl of the pcQD or pcNR was directly loaded to the cell cultured 35mmm glass bottom dish by pipet. Gentle shaking is followed, and plated under fluorescence microscopy for measurement. For FRET measurement, 2~10 μM of DPA at final concentration was added to the dish. To increase the signal to noise ratio, one might wash the dish with Dulbecco's Phosphate Buffered Saline (DPBS) after 5 min by replacing cell culture medium with DPBS.

Optical recording

The set-up is based on an Olympus IX71 inverted microscope equipped with a Xenon lamp (Olympus, U-LH75XEAPO, 75W) and excitation filter (BP 470/40, Chorma Technology Corp, Bellows Falls, VT). The emission of the NPs is collected by ×60 objective lens (Olympus, PlanApo 60×, n=1.45, oil immersion), passed through a dichroic mirror (DM, 505DCXRU, Chorma Technology Corp, Bellows Falls, VT). Single-view: The emission is detected by Andor iXon electron multiply (EM) charge coupled device (CCD) camera (EMCCD, Andor iXon, South Windsor, CT). Dual-view: Commercially available dual-view system is purchased from XXX, and a dichroic mirror (DM, Di02-R514-25x36, Semrock, Rochester, NY) is installed inside the dual-view component to split the QD's spectrum (511) to redder ($\lambda > 514$ nm) and bluer part ($\lambda < 514$ nm). Those images are collected the by Andot EMCCD.

Chapter 6

Conclusion

Developing inorganic voltage sensor and imaging cell membrane potential are ultimate goal of this study. Through the intensive experimental (Chapter 2, 3) and theoretical investigation (Chapter 2, 3 and 4), semiconductor NPs validate themselves as a sufficient voltage reporter which possesses superior sensitivity and faster than conventional optical voltage probes. Equipped with novel surface modification technique, two different NPs were successfully delivered to the cell membrane, displaying voltage dependent fluorescence emission (Chapter 5). This optical information is captured by EMCCD camera, translated to the voltage imaging, enabled high throughput analysis.

There are several findings in this study both experimental and theoretically, which are readdressed here. RT operating single molecule QCSE are demonstrated for the first time which opens the possibility of semiconductor NP as a voltage sensor. Before this study, there was no study reporting QCSE at RT at single molecule level. This is due to the thermal broadening, chaotic spectral noise and insensitive samples. I overcame these problem by *F*-modulation QCSE setup, statistical analysis, and using type-II energy structured nanomaterials. Unrevealed physical property of QCSE were found which are wavelength blue-shift, approximately linear $\Delta\lambda$-ΔF or ΔE-ΔF relation. It is especially noted that linear $\Delta\lambda$-ΔF is important for action potential detecting. Under action potential, type-II material generates monotonically increased or decreased (depends on the orientation) values of observables ($\Delta\lambda$, $\Delta\tau_r$, ΔI, I_R/I_B). In contrast, observables in type-I material change their polarity under action potential due to quadratic $\Delta\lambda$-ΔF relation. In addition, Auger recombination variation was explained in the context of QCSE for the type-II NP with experimental proof. It is found that Auger recombination rate is very sensitive indicator of applied electric field, influencing on intensity. These results are regenerated by self-consistent quantum mechanical calculation. In addition, voltage sensing performance of membrane-embedded NRs are predicted (Chapter 4) which estimates $\Delta\lambda$, $\Delta\tau_r$, ΔI, I_R/I_B.

Equally important achievements of this study are success of NR's cell membrane delivery and voltage imaging. This study first succeed to deliver quasi-type-II NR (and type-I QD) in the cell membrane with rationally designed alpha-helical peptide. This voltage sensing nanoparticle proves itself to self-insert into the cell membrane and optically record, non-invasively, membrane potential, at multi-sites, in a large field-of-view. This study also introduces different detecting methods including simple intensity, ratiometric intensity, and FRET measurement and compares their performances.

At the same time, this study also brings lots of homework. This includes optimization of NRs towards smaller asymmetric type-II NR (10 nm in length), optimization of peptide sequence towards more A-type insertion in Fig. 5.2 and development of better delivery method. Study regarding membrane-inserted NPs' influence on cell's capacitance and potential change should be marked as well. Similar to the delivery method used in this study, I would expect other inorganic NP voltage sensor.

With single molecule sensitivity, vsNPs could presumably afford the nanoscale recording of pre- and post-synaptic membrane potentials during release of- and signaling by-neurotransmitters, monitor individual ion channel activity, or a release of ions from single Ca^{+2} stores. With the appropriate optical imaging equipment, vsNPs could be used to optically record fast action potentials transients, in a high-throughput fashion, simultaneously at many sites, over a large field-of-view, and at superresolution. Moreover, deep tissue imaging could be afforded by two-photon excitation (2PE) using NIR-vsNPs and far-field non-linear temporal focusing microscopy. Such capabilities could eliminate the need for a crowded array of contact electrodes and bulky read-out electronics. vsNPs could therefore enable remote, noise-immune, sensitive action potential ratiometric recordings.

References

1.Sebel, P. S.; Lang, E.; Rampil, I. J.; White, P. F.; Cork, R.; Jopling, M.; Smith, N. T.; Glass, P. S.; Manberg, P., A multicenter study of bispectral electroencephalogram analysis for monitoring anesthetic effect. Anesthesia & Analgesia 1997, 84 (4), 891-899.

2.Belliveau, J. W., Functional mapping of the human visual cortex by magnetic resonance imaging. Science 1990, 254, 716-719.

3.Hamill, O. P.; Marty, A.; Neher, E.; Sakmann, B.; Sigworth, F. J., Improved patch-clamp techniques for high-resolution current recording from cells and cell-free membrane patches. Pflugers Arch. 1981, 391 (2), 85-100.

4.Spira, M. E.; Hai, A., Multi-electrode array technologies for neuroscience and cardiology. Nat Nano 2013, 8 (2), 83-94.

5.Pologruto, T. A.; Yasuda, R.; Svoboda, K., Monitoring neural activity and [Ca2+] with genetically encoded Ca2+ indicators. The Journal of neuroscience : the official journal of the Society for Neuroscience 2004, 24 (43), 9572-9.

6.Salama, G.; Choi, B. R.; Azour, G.; Lavasani, M.; Tumbev, V.; Salzberg, B. M.; Patrick, M. J.; Ernst, L. A.; Waggoner, A. S., Properties of New, Long-Wavelength, Voltage-sensitive Dyes in the Heart. J Membrane Biol 2005, 208 (2), 125-140.

7.Bradley, J.; Luo, R.; Otis, T. S.; DiGregorio, D. A., Submillisecond optical reporting of membrane potential in situ using a neuronal tracer dye. The Journal of neuroscience : the official journal of the Society for Neuroscience 2009, 29 (29), 9197-209.

8.Kralj, J. M.; Douglass, A. D.; Hochbaum, D. R.; Maclaurin, D.; Cohen, A. E., Optical recording of action potentials in mammalian neurons using a microbial rhodopsin. Nat Meth 2012, 9 (1), 90-95.

9.Jin, L.; Han, Z.; Platisa, J.; Wooltorton, Julian R. A.; Cohen, Lawrence B.; Pieribone, Vincent A., Single Action Potentials and Subthreshold Electrical Events Imaged in Neurons with a Fluorescent Protein Voltage Probe. Neuron 2012, 75 (5), 779-785.

10. Brus, L., Quantum crystallites and nonlinear optics. Appl. Phys. A 1991, 53 (6), 465-474.

11.Alivisatos, A. P., Semiconductor Clusters, Nanocrystals, and Quantum Dots. Science 1996, 271 (5251), 933-937.

12.Medintz, I. L.; Uyeda, H. T.; Goldman, E. R.; Mattoussi, H., Quantum dot bioconjugates for imaging, labelling and sensing. Nat Mater 2005, 4 (6), 435-446.

13.Michalet, X.; Pinaud, F. F.; Bentolila, L. A.; Tsay, J. M.; Doose, S.; Li, J. J.; Sundaresan, G.; Wu, A. M.; Gambhir, S. S.; Weiss, S., Quantum Dots for Live Cells, in Vivo Imaging, and Diagnostics. Science 2005, 307 (5709), 538-544.

14.Xu, X.; Sun, B.; Berman, P. R.; Steel, D. G.; Bracker, A. S.; Gammon, D.; Sham, L. J., Coherent population trapping of an electron spin in a single negatively charged quantum dot. Nat Phys 2008, 4 (9), 692-695.

15.Mora-Seró, I. n.; Bisquert, J., Breakthroughs in the Development of Semiconductor-Sensitized Solar Cells. The Journal of Physical Chemistry Letters 2010, 1 (20), 3046-3052.

16.Kim, T.-H.; Cho, K.-S.; Lee, E. K.; Lee, S. J.; Chae, J.; Kim, J. W.; Kim, D. H.; Kwon, J.-Y.; Amaratunga, G.; Lee, S. Y.; Choi, B. L.; Kuk, Y.; Kim, J. M.; Kim, K., Full-colour quantum dot displays fabricated by transfer printing. Nat Photon 2011, 5 (3), 176-182.

17.Peng, X.; Manna, L.; Yang, W.; Wickham, J.; Scher, E.; Kadavanich, A.; Alivisatos, A. P., Shape control of CdSe nanocrystals. Nature 2000, 404 (6773), 59-61.

18.Peng, Z. A.; Peng, X., Nearly Monodisperse and Shape-Controlled CdSe Nanocrystals via Alternative Routes: Nucleation and Growth. Journal of the American Chemical Society 2002, 124 (13), 3343-3353.

19.Murray, C. B.; Norris, D. J.; Bawendi, M. G., Synthesis and characterization of nearly monodisperse CdE (E = sulfur, selenium, tellurium) semiconductor nanocrystallites. Journal of the American Chemical Society 1993, 115 (19), 8706-8715.

20.Tang, J.; Sargent, E. H., Infrared Colloidal Quantum Dots for Photovoltaics: Fundamentals and Recent Progress. Advanced Materials 2011, 23 (1), 12-29.

21.Manna, L.; Scher, E. C.; Alivisatos, A. P., Synthesis of Soluble and Processable Rod-, Arrow-, Teardrop-, and Tetrapod-Shaped CdSe Nanocrystals. Journal of the American Chemical Society 2000, 122 (51), 12700-12706.

22.Kim, S.; Fisher, B.; Eisler, H.-J.; Bawendi, M., Type-II Quantum Dots: CdTe/CdSe(Core/Shell) and CdSe/ZnTe(Core/Shell) Heterostructures. Journal of the American Chemical Society 2003, 125 (38), 11466-11467.

23.Carbone, L.; Nobile, C.; De Giorgi, M.; Sala, F. D.; Morello, G.; Pompa, P.; Hytch, M.; Snoeck, E.; Fiore, A.; Franchini, I. R.; Nadasan, M.; Silvestre, A. F.; Chiodo, L.; Kudera, S.; Cingolani, R.; Krahne, R.; Manna, L., Synthesis and Micrometer-Scale Assembly of Colloidal

CdSe/CdS Nanorods Prepared by a Seeded Growth Approach. Nano Letters 2007, 7 (10), 2942-2950.

24.Dorfs, D.; Salant, A.; Popov, I.; Banin, U., ZnSe Quantum Dots Within CdS Nanorods: A Seeded-Growth Type-II System. Small 2008, 4 (9), 1319-1323.

25.Oron, D.; Kazes, M.; Banin, U., Multiexcitons in type-II colloidal semiconductor quantum dots. Physical Review B 2007, 75 (3), 035330.

26.Klimov, V. I.; Ivanov, S. A.; Nanda, J.; Achermann, M.; Bezel, I.; McGuire, J. A.; Piryatinski, A., Single-exciton optical gain in semiconductor nanocrystals. Nature 2007, 447 (7143), 441-446.

27.Avidan, A.; Oron, D., Large Blue Shift of the Biexciton State in Tellurium Doped CdSe Colloidal Quantum Dots. Nano Letters 2008, 8 (8), 2384-2387.

28.Medintz, I. L.; Stewart, M. H.; Trammell, S. A.; Susumu, K.; Delehanty, J. B.; Mei, B. C.; Melinger, J. S.; Blanco-Canosa, J. B.; Dawson, P. E.; Mattoussi, H., Quantum-dot/dopamine bioconjugates function as redox coupled assemblies for in vitro and intracellular pH sensing. Nature Materials 2010, 9 (8), 676-684.

29.Callan, J.; Mulrooney, R.; Kamila, S.; McCaughan, B., Anion Sensing with Luminescent Quantum Dots – A Modular Approach Based on the Photoinduced Electron Transfer (PET) Mechanism. Journal of Fluorescence 2008, 18 (2), 527-532.

30.Ruedas-Rama, M. J.; Hall, E. A. H., Azamacrocycle Activated Quantum Dot for Zinc Ion Detection. Analytical Chemistry 2008, 80 (21), 8260-8268.

31.Aouani, H.; Itzhakov, S.; Gachet, D.; Devaux, E. s.; Ebbesen, T. W.; Rigneault, H.; Oron, D.; Wenger, J. r. m., Colloidal Quantum Dots as Probes of Excitation Field Enhancement in Photonic Antennas. ACS Nano 2010, 4 (8), 4571-4578.

32.Li, S.; Zhang, K.; Yang, J.-M.; Lin, L.; Yang, H., Single Quantum Dots as Local Temperature Markers. Nano Letters 2007, 7 (10), 3102-3105.

33.Choi, C. L.; Koski, K. J.; Olson, A. C. K.; Alivisatos, A. P., Luminescent nanocrystal stress gauge. Proceedings of the National Academy of Sciences 2010.

34.Müller, J.; Lupton, J. M.; Rogach, A. L.; Feldmann, J.; Talapin, D. V.; Weller, H., Monitoring surface charge migration in the spectral dynamics of single CdSe⁄CdS nanodot/nanorod heterostructures. Physical Review B 2005, 72 (20), 205339.

35.Novelli, F.; Fausti, D.; Giusti, F.; Parmigiani, F.; Hoffmann, M., Mixed regime of light-matter interaction revealed by phase sensitive measurements of the dynamical Franz-Keldysh effect. Sci. Rep. 2013, 3.

36.Miller, D. A. B.; Chemla, D. S.; Damen, T. C.; Gossard, A. C.; Wiegmann, W.; Wood, T. H.; Burrus, C. A., Band-Edge Electroabsorption in Quantum Well Structures: The Quantum-Confined Stark Effect. Physical Review Letters 1984, 53 (22), 2173-2176.

37.Empedocles, S. A.; Bawendi, M. G., Quantum-Confined Stark Effect in Single CdSe Nanocrystallite Quantum Dots. Science 1997, 278 (5346), 2114-2117.

38.Miller, D.; Chemla, D.; Damen, T.; Wood, T.; Burrus, C.; Gossard, A.; Wiegmann, W., The quantum well self-electrooptic effect device: Optoelectronic bistability and oscillation, and self-linearized modulation. Quantum Electronics, IEEE Journal of 1985, 21 (9), 1462-1476.

39.Kuo, Y.-H.; Lee, Y. K.; Ge, Y.; Ren, S.; Roth, J. E.; Kamins, T. I.; Miller, D. A. B.; Harris, J. S., Strong quantum-confined Stark effect in germanium quantum-well structures on silicon. Nature 2005, 437 (7063), 1334-1336.

40.Galland, C.; Ghosh, Y.; Steinbruck, A.; Sykora, M.; Hollingsworth, J. A.; Klimov, V. I.; Htoon, H., Two types of luminescence blinking revealed by spectroelectrochemistry of single quantum dots. Nature 2011, 479 (7372), 203-207.

41.Wang, Y.; Fruhwirth, G.; Cai, E.; Ng, T.; Selvin, P. R., 3D Super-Resolution Imaging with Blinking Quantum Dots. Nano Letters 2013, 13 (11), 5233-5241.

42.Royo, M.; Climente, J. I.; Movilla, J. L.; Planelles, J., Dielectric confinement of excitons in type-I and type-II semiconductor nanorods. Journal of Physics: Condensed Matter 2011, 23 (1), 015301.

43.Yan, L., Voltage-dependent electroluminescence from colloidal CdSe/ZnS quantum dots. Appl. Phys. Lett. 2007, 91 (24), 243114.

44.Yakimov, A. I.; Dvurechenskii, A. V.; Nikiforov, A. I.; Ulyanov, V. V.; Milekhin, A. G.; Govorov, A. O.; Schulze, S.; Zahn, D. R. T., Stark effect in type-II Ge/Si quantum dots. Physical Review B 2003, 67 (12), 125318.

45.Rothenberg, E.; Kazes, M.; Shaviv, E.; Banin, U., Electric Field Induced Switching of the Fluorescence of Single Semiconductor Quantum Rods. Nano Letters 2005, 5 (8), 1581-1586.

46.Hewa-Kasakarage, N. N.; Kirsanova, M.; Nemchinov, A.; Schmall, N.; El-Khoury, P. Z.; Tarnovsky, A. N.; Zamkov, M., Radiative Recombination of Spatially Extended Excitons in (ZnSe/CdS)/CdS Heterostructured Nanorods. Journal of the American Chemical Society 2009, 131 (3), 1328-1334.

47.Deutsch, Z.; Schwartz, O.; Tenne, R.; Popovitz-Biro, R.; Oron, D., Two-Color Antibunching from Band-Gap Engineered Colloidal Semiconductor Nanocrystals. Nano Letters 2012, 12 (6), 2948-2952.

48.Dias, E. A.; Grimes, A. F.; English, D. S.; Kambhampati, P., Single Dot Spectroscopy of Two-Color Quantum Dot/Quantum Shell Nanostructures. The Journal of Physical Chemistry C 2008, 112 (37), 14229-14232.

49.Miller, D. A. B., Optical bistability in self-electro-optic effect devices with asymmetric quantum wells. Applied Physics Letters 1989, 54 (3), 202-204.

50.Haywood, S. K.; Lim, A. C. H.; Gupta, R.; Emery, S.; Hogg, J. H. C.; Hewer, V.; Stavrinou, P. N.; Hopkinson, M.; Hill, G., Demonstration of a blueshift in type II asymmetric InP/InAsP/InGaAs multiple quantum wells. Journal of Applied Physics 2003, 94 (5), 3222-3228.

51.Nirmal, M.; Dabbousi, B. O.; Bawendi, M. G.; Macklin, J. J.; Trautman, J. K.; Harris, T. D.; Brus, L. E., Fluorescence intermittency in single cadmium selenide nanocrystals. Nature 1996, 383 (6603), 802-804.

52.Pelton, M., Characterizing quantum-dot blinking using noise power spectra. Appl. Phys. Lett. 2004, 85 (5), 819.

53.Frantsuzov, P.; Kuno, M.; Janko, B.; Marcus, R. A., Universal emission intermittency in quantum dots, nanorods and nanowires. Nat Phys 2008, 4 (5), 519-522.

54.Kuno, M., Nonexponential ?blinking? kinetics of single CdSe quantum dots: A universal power law behavior. J. Chem. Phys. 2000, 112 (7), 3117.

55.Talapin, D. V.; Koeppe, R.; Götzinger, S.; Kornowski, A.; Lupton, J. M.; Rogach, A. L.; Benson, O.; Feldmann, J.; Weller, H., Highly Emissive Colloidal CdSe/CdS Heterostructures of Mixed Dimensionality. Nano Letters 2003, 3 (12), 1677-1681.

56.Müller, J.; Lupton, J. M.; Lagoudakis, P. G.; Schindler, F.; Koeppe, R.; Rogach, A. L.; Feldmann, J.; Talapin, D. V.; Weller, H., Wave Function Engineering in Elongated Semiconductor Nanocrystals with Heterogeneous Carrier Confinement. Nano Letters 2005, 5 (10), 2044-2049.

57.Kraus, R. M.; Lagoudakis, P. G.; Rogach, A. L.; Talapin, D. V.; Weller, H.; Lupton, J. M.; Feldmann, J., Room-Temperature Exciton Storage in Elongated Semiconductor Nanocrystals. Physical Review Letters 2007, 98 (1), 017401.

58.Sitt, A.; Sala, F. D.; Menagen, G.; Banin, U., Multiexciton Engineering in Seeded Core/Shell Nanorods: Transfer from Type-I to Quasi-type-II Regimes. Nano Letters 2009, 9 (10), 3470-3476.

59.Haas, H.; Magnea, N.; Dang, L. S., Quantum-confined Stark effect on spatially indirect excitons in CdTe/Cd_x Zn_{1-x} Te quantum wells. Physical Review B 1997, 55 (3), 1563-1567.

60.Wang, C. H.; Chen, T. T.; Tan, K. W.; Chen, Y. F.; Cheng, C. T.; Chou, P. T., Photoluminescence properties of CdTe/CdSe core-shell type-II quantum dots. Journal of Applied Physics 2006, 99 (12), 123521-4.

61.Baskoutas, S.; Terzis, A. F., Size-dependent band gap of colloidal quantum dots. Journal of Applied Physics 2006, 99 (1), 013708-4.

62.Nemchinov, A.; Kirsanova, M.; Hewa-Kasakarage, N. N.; Zamkov, M., Synthesis and Characterization of Type II ZnSe/CdS Core/Shell Nanocrystals. The Journal of Physical Chemistry C 2008, 112 (25), 9301-9307.

63.Mews, A.; Eychmueller, A.; Giersig, M.; Schooss, D.; Weller, H., Preparation, characterization, and photophysics of the quantum dot quantum well system cadmium sulfide/mercury sulfide/cadmium sulfide. The Journal of Physical Chemistry 1994, 98 (3), 934-941.

64.Wang, S.; Wang, L.-W., Exciton Dissociation in CdSe/CdTe Heterostructure Nanorods. The Journal of Physical Chemistry Letters 2010, 2 (1), 1-6.

65.Susa, N., Quantum-confined Stark effects in semiconductor quantum disks. Quantum Electronics, IEEE Journal of 1996, 32 (10), 1760-1766.

66.Aspnes, D. E., Electric-Field Effects on Optical Absorption near Thresholds in Solids. Physical Review 1966, 147 (2), 554-566.

67.Keldysh, L. V., Behaviour of Non-Metallic Crystals in Strong Electric Fields. Soviet Physics: J. Exptl. Theoret. Phys. 1957, 33, 994-1003.

68.Park, K.; Deutsch, Z.; Li, J. J.; Oron, D.; Weiss, S., Single Molecule Quantum-Confined Stark Effect Measurements of Semiconductor Nanoparticles at Room Temperature. ACS Nano 2012, 6 (11), 10013-10023.

69.Wang, W.; Banerjee, S.; Jia, S.; Steigerwald, M. L.; Herman, I. P., Ligand Control of Growth, Morphology, and Capping Structure of Colloidal CdSe Nanorods. Chemistry of Materials 2007, 19 (10), 2573-2580.

70.Talapin, D. V.; Nelson, J. H.; Shevchenko, E. V.; Aloni, S.; Sadtler, B.; Alivisatos, A. P., Seeded Growth of Highly Luminescent CdSe/CdS Nanoheterostructures with Rod and Tetrapod Morphologies. Nano Letters 2007, 7 (10), 2951-2959.

71.Jack Li, J.; Tsay, J. M.; Michalet, X.; Weiss, S., Wavefunction engineering: From quantum wells to near-infrared type-II colloidal quantum dots synthesized by layer-by-layer colloidal epitaxy. Chemical Physics 2005, 318 (1–2), 82-90.

72.Avidan, A.; Deutsch, Z.; Oron, D., Interactions of bound excitons in doped core/shell quantum dot heterostructures. Physical Review B 2010, 82 (16), 165332.

73.Li, J. J.; Wang, Y. A.; Guo, W.; Keay, J. C.; Mishima, T. D.; Johnson, M. B.; Peng, X., Large-Scale Synthesis of Nearly Monodisperse CdSe/CdS Core/Shell Nanocrystals Using Air-Stable Reagents via Successive Ion Layer Adsorption and Reaction. Journal of the American Chemical Society 2003, 125 (41), 12567-12575.

74.Hu, J.; Li, L.-s.; Yang, W.; Manna, L.; Wang, L.-w.; Alivisatos, A. P., Linearly Polarized Emission from Colloidal Semiconductor Quantum Rods. Science 2001, 292 (5524), 2060-2063.

75.Hu, Z.; Fischbein, M. D.; Querner, C.; Drndić, M., Electric-Field-Driven Accumulation and Alignment of CdSe and CdTe Nanorods in Nanoscale Devices. Nano Letters 2006, 6 (11), 2585-2591.

76.Boda, D.; Gillespie, D.; Nonner, W.; Henderson, D.; Eisenberg, B., Computing induced charges in inhomogeneous dielectric media: Application in a Monte Carlo simulation of complex ionic systems. Physical Review E 2004, 69 (4), 046702.

77.Movilla, J. L.; Climente, J. I.; Planelles, J., Dielectric polarization in axially-symmetric nanostructures: A computational approach. Computer Physics Communications 2010, 181 (1), 92-98.

78.Caruge, J. M.; Halpert, J. E.; Wood, V.; Bulovic, V.; Bawendi, M. G., Colloidal quantum-dot light-emitting diodes with metal-oxide charge transport layers. Nat Photon 2008, 2 (4), 247-250.

79.Efros, A. L.; Rosen, M., Random Telegraph Signal in the Photoluminescence Intensity of a Single Quantum Dot. Physical Review Letters 1997, 78 (6), 1110-1113.

80.Cragg, G. E.; Efros, A. L., Suppression of Auger Processes in Confined Structures. Nano Letters 2009, 10 (1), 313-317.

81.Wang, X.; Ren, X.; Kahen, K.; Hahn, M. A.; Rajeswaran, M.; Maccagnano-Zacher, S.; Silcox, J.; Cragg, G. E.; Efros, A. L.; Krauss, T. D., Non-blinking semiconductor nanocrystals. Nature 2009, 459 (7247), 686-689.

82.Chen, Y.; Vela, J.; Htoon, H.; Casson, J. L.; Werder, D. J.; Bussian, D. A.; Klimov, V. I.; Hollingsworth, J. A., “Giant” Multishell CdSe Nanocrystal Quantum Dots with Suppressed Blinking. Journal of the American Chemical Society 2008, 130 (15), 5026-5027.

83.Climente, J. I.; Movilla, J. L.; Planelles, J., Auger Recombination Suppression in Nanocrystals with Asymmetric Electron–Hole Confinement. Small 2012, 8 (5), 754-759.

84.Bae, W. K.; Padilha, L. A.; Park, Y.-S.; McDaniel, H.; Robel, I.; Pietryga, J. M.; Klimov, V. I., Controlled Alloying of the Core–Shell Interface in CdSe/CdS Quantum Dots for Suppression of Auger Recombination. ACS Nano 2013, 7 (4), 3411-3419.

85.Alivisatos, A. P.; Chun, M.; Church, George M.; Greenspan, Ralph J.; Roukes, Michael L.; Yuste, R., The Brain Activity Map Project and the Challenge of Functional Connectomics. Neuron 2012, 74 (6), 970-974.

86.Alivisatos, A. P.; Chun, M.; Church, G. M.; Deisseroth, K.; Donoghue, J. P.; Greenspan, R. J.; McEuen, P. L.; Roukes, M. L.; Sejnowski, T. J.; Weiss, P. S.; Yuste, R., The Brain Activity Map. Science 2013, 339 (6125), 1284-1285.

87.Peterka, D. S.; Takahashi, H.; Yuste, R., Imaging Voltage in Neurons. Neuron 2011, 69 (1), 9-21.

88.Grinvald, A.; Hildesheim, R., VSDI: a new era in functional imaging of cortical dynamics. Nat Rev Neurosci 2004, 5 (11), 874-885.

89.Klymchenko, A. S.; Stoeckel, H.; Takeda, K.; Mély, Y., Fluorescent Probe Based on Intramolecular Proton Transfer for Fast Ratiometric Measurement of Cellular Transmembrane Potential. The Journal of Physical Chemistry B 2006, 110 (27), 13624-13632.

90.DiFranco, M.; Capote, J.; Quinonez, M.; Vergara, J. L., Voltage-dependent dynamic FRET signals from the transverse tubules in mammalian skeletal muscle fibers. J Gen Physiol 2007, 130 (6), 581-600.

91.Marshall, J. D.; Schnitzer, M. J., Optical Strategies for Sensing Neuronal Voltage Using Quantum Dots and Other Semiconductor Nanocrystals. ACS Nano 2013, 7 (5), 4601-4609.

92.Hemdana, I.; Mahdouani, M.; Bourguiga, R., Investigation of the radiative lifetime in core–shell CdSe/ZnS and CdSe/ZnSe quantum dots. Physica B: Condensed Matter 2012, 407 (17), 3313-3319.

93.Park, S.-J.; Link, S.; Miller, W. L.; Gesquiere, A.; Barbara, P. F., Effect of electric field on the photoluminescence intensity of single CdSe nanocrystals. Chemical Physics 2007, 341 (1–3), 169-174.

94.Gadella Jr, T. W. J.; Jovin, T. M.; Clegg, R. M., Fluorescence lifetime imaging microscopy (FLIM): Spatial resolution of microstructures on the nanosecond time scale. Biophysical Chemistry 1993, 48 (2), 221-239.

95.Colyer, R. A.; Siegmund, O. H. W.; Tremsin, A. S.; Vallerga, J. V.; Weiss, S.; Michalet, X., Phasor imaging with a widefield photon-counting detector. BIOMEDO 2012, 17 (1), 0160081-01600812.

96.Michalet, X.; Siegmund, O. H. W.; Vallerga, J. V.; Jelinsky, P.; Millaud, J. E.; Weiss, S., Photon-counting H33D detector for biological fluorescence imaging. Nuclear Instruments and Methods in Physics Research Section A: Accelerators, Spectrometers, Detectors and Associated Equipment 2006, 567 (1), 133-136.

97.Michalet, X.; Colyer, R. A.; Antelman, J.; Siegmund, O. H.; Tremsin, A.; Vallerga, J. V.; Weiss, S., Single-quantum dot imaging with a photon counting camera. Current pharmaceutical biotechnology 2009, 10 (5), 543-558.

98.Gopalakrishnan, G.; Danelon, C.; Izewska, P.; Prummer, M.; Bolinger, P.-Y.; Geissbühler, I.; Demurtas, D.; Dubochet, J.; Vogel, H., Multifunctional Lipid/Quantum Dot Hybrid Nanocontainers for Controlled Targeting of Live Cells. Angewandte Chemie International Edition 2006, 45 (33), 5478-5483.

99.Kloepfer, J. A.; Cohen, N.; Nadeau, J. L., FRET between CdSe Quantum Dots in Lipid Vesicles and Water- and Lipid-soluble Dyes. The Journal of Physical Chemistry B 2004, 108 (44), 17042-17049.

100.Schipper, M. L.; Iyer, G.; Koh, A. L.; Cheng, Z.; Ebenstein, Y.; Aharoni, A.; Keren, S.; Bentolila, L. A.; Li, J. Q.; Rao, J. H.; Chen, X. Y.; Banin, U.; Wu, A. M.; Sinclair, R.; Weiss, S.; Gambhir, S. S., Particle Size, Surface Coating, and PEGylation Influence the Biodistribution of Quantum Dots in Living Mice. Small 2009, 5 (1), 126-134.

101.Iyer, G.; Pinaud, F.; Xu, J. M.; Ebenstein, Y.; Li, J.; Chang, J.; Dahan, M.; Weiss, S., Aromatic Aldehyde and Hydrazine Activated Peptide Coated Quantum Dots for Easy Bioconjugation and Live Cell Imaging. Bioconjugate Chem 2011, 22 (6), 1006-1011.

102.Chan, W. C. W.; Nie, S., Quantum Dot Bioconjugates for Ultrasensitive Nonisotopic Detection. Science 1998, 281 (5385), 2016-2018.

103.Mason, J.; Tomlinson, I.; Rosenthal, S.; Blakely, R., Labeling Cell-Surface Proteins Via Antibody Quantum Dot Streptavidin Conjugates. In NanoBiotechnology Protocols, Rosenthal, S.; Wright, D., Eds. Humana Press: 2005; Vol. 303, pp 35-50.

104.Jin, T.; Tiwari, D. K.; Tanaka, S.-i.; Inouye, Y.; Yoshizawa, K.; Watanabe, T. M., Antibody-ProteinA conjugated quantum dots for multiplexed imaging of surface receptors in living cells. Molecular bioSystems 2010, 6 (11), 2325-2331.

105.Xu, J.; Teslaa, T.; Wu, T.-H.; Chiou, P.-Y.; Teitell, M. A.; Weiss, S., Nanoblade Delivery and Incorporation of Quantum Dot Conjugates into Tubulin Networks in Live Cells. Nano Letters 2012, 12 (11), 5669-5672.

106.Al-Jamal, W. T.; Al-Jamal, K. T.; Tian, B.; Lacerda, L.; Bomans, P. H.; Frederik, P. M.; Kostarelos, K., Lipid−Quantum Dot Bilayer Vesicles Enhance Tumor Cell Uptake and Retention in Vitro and in Vivo. ACS Nano 2008, 2 (3), 408-418.

107.Wi, H. S.; Kim, S. J.; Lee, K.; Kim, S. M.; Yang, H. S.; Pak, H. K., Incorporation of quantum dots into the lipid bilayer of giant unilamellar vesicles and its stability. Colloids and Surfaces B: Biointerfaces 2012, 97 (0), 37-42.

108.Bailey, A. L.; Cullis, P. R., Membrane Fusion with Cationic Liposomes: Effects of Target Membrane Lipid Composition†. Biochemistry 1997, 36 (7), 1628-1634.

109.Lonez, C.; Lensink, M.; Kleiren, E.; Vanderwinden, J.-M.; Ruysschaert, J.-M.; Vandenbranden, M., Fusogenic activity of cationic lipids and lipid shape distribution. Cell. Mol. Life Sci. 2010, 67 (3), 483-494.

110.Park, J.; Werley, C. A.; Venkatachalam, V.; Kralj, J. M.; Dib-Hajj, S. D.; Waxman, S. G.; Cohen, A. E., Screening Fluorescent Voltage Indicators with Spontaneously Spiking HEK Cells. PloS One 2013, 8 (12), e85221.

111.Dubois, F.; Mahler, B.; Dubertret, B.; Doris, E.; Mioskowski, C., A Versatile Strategy for Quantum Dot Ligand Exchange. Journal of the American Chemical Society 2006, 129 (3), 482-483.

112.Sperling, R. A.; Parak, W. J., Surface modification, functionalization and bioconjugation of colloidal inorganic nanoparticles. Philosophical Transactions of the Royal Society A: Mathematical, Physical and Engineering Sciences 2010, 368 (1915), 1333-1383.

113.Iyer, G.; Pinaud, F.; Tsay, J.; Weiss, S., Solubilization of Quantum Dots with a Recombinant Peptide from Escherichia coli. Small 2007, 3 (5), 793-798.

114.Rost, B.; Fariselli, P.; Casadio, R., Topology prediction for helical transmembrane proteins at 86% accuracy–Topology prediction at 86% accuracy. Protein Science 1996, 5 (8), 1704-1718.

115.Leatherdale, C. A.; Woo, W. K.; Mikulec, F. V.; Bawendi, M. G., On the Absorption Cross Section of CdSe Nanocrystal Quantum Dots. The Journal of Physical Chemistry B 2002, 106 (31), 7619-7622.

116.Wayne, N. L.; Kuwahara, K.; Aida, K.; Nagahama, Y.; Okubo, K., Whole-Cell Electrophysiology of Gonadotropin-Releasing Hormone Neurons that Express Green Fluorescent Protein in the Terminal Nerve of Transgenic Medaka (Oryzias latipes). Biology of Reproduction 2005, 73 (6), 1228-1234.

117.Miller, E. W.; Lin, J. Y.; Frady, E. P.; Steinbach, P. A.; Kristan, W. B.; Tsien, R. Y., Optically monitoring voltage in neurons by photo-induced electron transfer through molecular wires. Proceedings of the National Academy of Sciences of the United States of America 2012, 109 (6), 2114-2119.

118.Mornet, S.; Vasseur, S.; Grasset, F.; Duguet, E., Magnetic nanoparticle design for medical diagnosis and therapy. Journal of Materials Chemistry 2004, 14 (14), 2161-2175.

119.Storhoff, J. J.; Elghanian, R.; Mucic, R. C.; Mirkin, C. A.; Letsinger, R. L., One-Pot Colorimetric Differentiation of Polynucleotides with Single Base Imperfections Using Gold Nanoparticle Probes. Journal of the American Chemical Society 1998, 120 (9), 1959-1964.